Amplification of Long-Range Surface Plasmon-Polaritons

by
Israel De Leon Arizpe

A thesis presented to the
Faculty of Graduate and Postdoctoral Studies
in partial fulfillment of the requirements for the degree of

Doctor of Philosophy
in Electrical Engineering

Ottawa-Carleton Institute for Electrical and Computer Engineering
School of Information Technology and Engineering
Faculty of Engineering
University of Ottawa

Abstract

Surface plasmon-polaritons are optical surface waves formed through the interaction of photons with free electrons at the surface of metals. They offer interesting applications in a broad range of scientific fields such as physics, chemistry, biology, and material science. However, many of such applications face limitations imposed by the high propagation losses of these waves at visible and near-infrared wavelengths, which result mainly from power dissipation in the metal.

In principle, the propagation losses of surface plasmon-polaritons can be compensated through optical amplification. The objective of this thesis is to provide deeper insights on the physics of surface plasmon-polariton amplification and spontaneous emission in surface plasmon-polariton amplifiers through theoretical and experimental vehicles applied (but not necessarily restricted) to a particular plasmonic mode termed *long-range* surface plasmon-polariton.

On the theoretical side, the objective is approached by developing a realistic theoretical model to describe the small-signal amplification of surface plasmon-polaritons in planar structures incorporating dipolar gain media such as organic dye molecules, rare-earth ions, and quantum dots. This model takes into account the inhomogeneous gain distribution formed near the metal surface due to a non-uniform excitation of dipoles and due to a position-dependent excited-state dipole lifetime that results from near-field interactions between the excited dipoles and the metal. Also, a theoretical model to describe the amplified spontaneous emission of surface plasmon-polaritons supported by planar metallic structures is developed. This model takes into account the different energy decay channels into which an exited dipole located in the vicinity of the metal can relax. The validity of this model is confirmed through experimentation.

On the experimental side, the objective is approached by providing a direct experimental demonstration of complete loss compensation in a plasmonic waveguide. The experiments are conducted using the *long-range* surface plasmon-polariton supported by a symmetric thin gold waveguide incorporating optically pumped organic dye molecules in solution as the gain medium. Also, an experimental study of spontaneous emission in a *long-range* surface plasmon-polariton amplifier is presented. It is shown that this amplifier benefits from a low spontaneous emission into the amplified mode, which leads to an optical amplifier with low noise characteristics. The experimental setup and techniques are explained in detail.

To God Almighty, Who created light.

Acknowledgements

First and foremost I thank God for having made all possible by giving me health and strength to accomplishing this work.

I thank my beautiful wife, Claudia, for her loving support and understanding throughout my doctoral studies. Claudia, you are the reason behind all my efforts; I love you. Also, I thank my family for their unconditional support.

I would like to express my appreciation to my thesis advisor, Dr. Pierre Berini, for letting me work in such an exciting research topic, for his guidance, and for the countless hours of research-oriented discussion. I am also grateful to Dr. Berini for providing the financial support, which partially made this work possible.

I am thankful to Dr. J.C. (Tito) Scaiano, Michel Grenier, and other members of the photochemistry laboratory at the University of Ottawa for their assistance in measuring some of the photophysical parameters of the laser dye used for the experimentation, and for valuable discussions in related topics.

I would like to thank Ewa Lisicka-Shrzek for the initial training on optical measurements in surface plasmon-polariton waveguides and for numerous discussions regarding experimental matters. Also, I would like to thank the people working in the research laboratory for their friendship and many hours of interesting conversations and non-research related activities.

Publications

Book chapters accepted and in preparation

- De Leon, I. & Berini, P. Amplification and lasing with surface plasmon-polaritions in *Plasmonics and Plasmonic Metamaterials: Analysis and Applications*. World Scientific (to be published). **Invited**.

- De Leon, I. & Berini, P. Amplification of long-range surface plasomons in *Terahertz and Optical Plasmonics and Metamaterial*. Pan Stanford Publishing (in preparation). **Invited**.

Papers published and accepted in refereed journals

- De Leon, I. & Berini, P. Measuring gain and noise in long-range surface plasmon-polariton waveguides. *Rev. Sci. Inst.* (to be published).

- De Leon, I. & Berini, P. Spontaneous emission in long-range surface plasmon-polariton amplifiers. *Phys. Rev. B.* (to be published).

- De Leon, I. & Berini, P. Amplification of long-range surface plasmons by a dipolar gain medium. *Nature Photon.*. **4,** 382-387 (2010).

- De Leon, I. & Berini, P. Modeling surface plasmon-polariton gain in planar metallic structures. *Opt. Express.* **17** 20191-20202 (2009).

- De Leon, I. & Berini, P. Theory of surface plasmon-polariton amplification in planar structures incorporating dipolar gain media. *Phys. Rev. B.* **78,** 161401(R) (2008).

Papers published and accepted in refereed conferences

- De Leon, I. & Berini, P. Gain and noise in long-range surface plasmon-polariton amplifiers, CLEO: QELS Fundamental Science 3: Metamaterials and Complex Media, Baltimore MD, USA (2011).

- De Leon, I. & Berini, P. Amplification of surface plasmons. SPIE Photonics West: Ultrafast Phenomena in Semiconductors and Nanostructure Materials XV, San Francisco, USA. (2011) **Invited**.

- Berini, P. & De Leon, I. Spontaneous and Stimulated Emission into Surface Plasmons. OSA Frontiers in Optics 2010 / APS Laser Science XXVI, Rochester NY, USA. (2010) **Invited**.

- De Leon, I. & Berini, P. Theory and modeling of surface plasmon gain in planar metallic structures. Progress on Electromagnetics Research Symposium - PIERS 2010, Cambridge MA, USA (2010).

- De Leon, I. & Berini, P. Towards amplification of surface plasmon-polaritons using dipolar gain media. 4 th. International Conference on Surface Plasmon Photonics - SPP4, Amsterdam, The Netherlands (2009).

- Berini, P. & De Leon, I. Sensitivities and amplification of surface plasmons. Proc. SPIE, **7395,** 73950Y (2009).

- De Leon, I. & Berini, P. Surface plasmon-polariton mode amplification in long range waveguides. Proc. SPIE, **6896,** 68960K (2008).

Invited paper in a workshop

- Berini, P., De Leon, I. & Akbari, A. Active Surface Plasmon Photonics. Workshop on Nano-optics, Plasmonics, and Advanced Materials, NIST, Gaithersburg MD, USA. (2010).

Acronyms

AOM Acousto-Optic Modulator

APD Avalanche Photodiode

ASE Amplified Spontaneous Emission

ASE-LRSPP ASE of Long-Range Surface Plasmon-Polaritons

CW Continuous Wave

DFB Distributed-Feedback

EH Electron-Hole

FWHM Full-Width-Half-Maximum

GPIB General Purpose Interface Bus

LRSPP Long-Range Surface Plasmon-Polariton

laser Light Amplification by Stimulated Emission of Radiation

PM Polarization-Maintaining

QW Quantum Well

QC Quantum Cascade

QD Quantum Dot

R6G Rhodamine-6G

spaser Surface Plasmon Amplification by Stimulated Emission of Radiation

SPP Surface Plasmon-Polariton

SRSPP Short-Range Surface Plasmon-Polariton

TM Transverse Magnetic

TE Transverse Electric

Table of Contents

CHAPTER 1

Introduction

This chapter presents a basic introduction to the electromagnetic properties of surface plasmon-polaritons. The discussion focuses on two typical cases to describe the key properties of these electromagnetic waves. Also, the motivation for studying the topic of surface plasmon-polariton amplification is addressed and the related body of literature reviewed. Finally, the scope and organisation of this thesis are presented.

1.1 Surface plasmon-polaritons

Valence electrons in metals can be regarded as a high density gas of charges that move through a static ionic lattice [1]. This electron gas (as well as other plasmas) can sustain charge density oscillations called plasma oscillations or plasmons [2]; the latter being the quantised quasiparticle of the former. Light in the visible and near-infrared spectrum can couple to plasma oscillations at the surface of some metals creating hybrid (plasmon-polariton) surface waves that propagate along the metal interface with a dielectric. Due to its hybrid nature, the quantised quasiparticle of these surface waves is termed *surface plasmon-polariton* (SPP).

SPPs exist on surfaces of metals with a negative real part of permittivity (e.g., Au, Ag, Cu, and Al at visible and near-infrared wavelengths [3]) and their fields are exclusively transverse-magnetic (TM) polarised – the magnetic field lies in the plane of the metal surface. SPPs have larger momenta than photons at the same frequency, forbidding direct coupling and giving the characteristic surface-wave nature to SPPs. As a result, mechanisms such as grating- or evanescent-wave-coupling are needed to excite SPP with light. Also, SPPs dissipate their energy in the metal, mainly through electron scattering, which results in large propagation losses in the visible and near-infrared wavelength spectrum.

A variety of metallic structures can support SPPs. The structure's shape, dimensions, and material properties define key characteristic of these surface waves. Indeed, a main distinction is made between SPPs supported by planar metallic surfaces and metallic nano-particles with sizes smaller than the free-space wavelength. The former type of structure support SPPs that propagate along the metal surface and hence they are often referred to as *propagating* SPPs. On the other hand, for the latter type of structure, SPPs are confined to the nanoparticle itself and hence they are referred to as *localised* SPPs. This thesis considers only planar metallic structures; hence, the

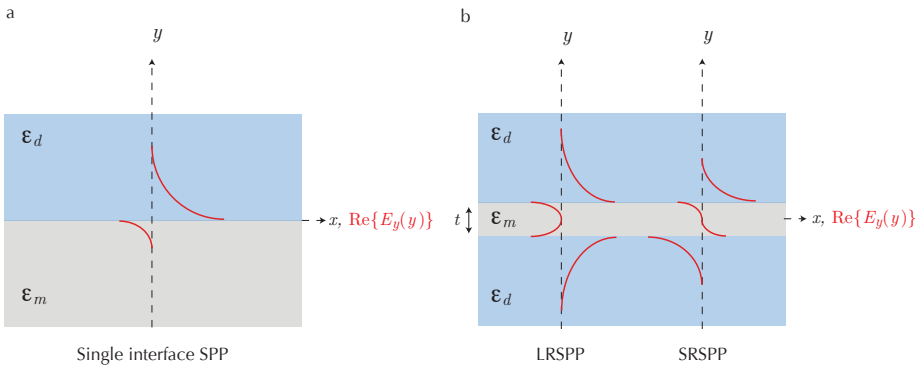

Figure 1.1 | Important planar plasmonic structures: (a) single metal-dielectric interface and (b) metal slab bounded by dielectrics. The main transverse electric field distribution, $E_y(y)$, of the SPP modes supported by each structure is sketched in red. The $+z$-coordinate points out of the page.

term *propagating* will be omitted henceforth when referring to these SPPs.

Two planar structures widely used in plasmonics applications are shown in Fig. 1.1. They consist of a metallic region with complex permittivity, ε_m, bounded by a dielectric with permittivity, ε_d, which could also be complex but with positive real part. Fig. 1.1 a depicts two semi-infinite media forming a metal-dielectric interface; this structure supports the so-called *single-interface* SPP [2]. On the other hand, Fig. 1.1 b depicts a metal slab of thickness t bounded by optically infinite dielectrics on both sides. When t is large, the structure's electromagnetic properties are no different than those of the single interface structure. However, when t is small enough, the SPPs at each metal-dielectric interface couple forming two supermodes with symmetric and asymmetric transverse field distributions termed *long-range* SPPs (LRSPPs) and *short-range* SPPs (SRSPPs), respectively [4]-[9]. In general, the top and bottom dielectrics in Fig. 1.1 b can have different permittivities but for the purposes of this discussion we shall focus on the symmetric case.

For the two structures of interest, the fields of SPPs propagating along the positive z-axis, pointing out of the page, have the form (time-harmonic dependance $e^{i\omega t}$ implicit)

$$\begin{aligned} \mathbf{E} &= [0, E_y(y), E_z(y)] \exp(-ikz) \\ \mathbf{H} &= [H_x(y), 0, 0] \exp(-ikz), \end{aligned} \tag{1.1}$$

where $k = \beta - i\alpha$ is the SPP wavevector, with β and α being the phase and field-attenuation coefficients, respectively. Note that the fields are TM-polarised. The main transverse electric field distribution, $E_y(y)$, of each SPP is sketched over the structure cross-section. As it is characteristic of a surface wave, the fields peak at the metal surface while they decay exponentially into both the metal and the bounding dielectric.

Next we shall examine the key properties of SPPs based on the two simple structures presented above.

1.1.1 Dispersion relations

An appealing method to understanding the dispersion properties of SPPs is studying how an electric dipole located in the vicinity of the metal surface dissipates power into the modes supported by the electromagnetic environment [10]. For this we consider the structures in Fig. 1.1 with silver and glass as the metal and dielectric regions, respectively, and with $t = 20$ nm as the slab thickness. The complex permittivity of silver is approximated by the Drude model [1]

$$\varepsilon_m = 1 - \frac{\omega_p^2}{\omega^2 - i\omega\zeta}, \tag{1.2}$$

where $\omega_p = 1.2 \times 10^{16}$ rad/s and $\zeta = 9.11 \times 10^{13}$ rad/s are, respectively, the plasma angular frequency and damping constant for silver [1]. The permittivity of glass is taken as $\varepsilon_d = 2.1$. Fig. 1.2 a and b show calculations of the power dissipated by a y-oriented dipole placed 50 nm away from the metal surface of the structures shown in Fig. 1.1 a and b, respectively. The vertical axes indicate the angular frequency of light in free-space, ω, normalised to ω_p. The horizontal axes correspond to the wavevector component in the metal plane (in-plane wavevector) normalised to the plasma wavevector, $k_p = \omega_p/c$, with c being the speed of light in free-space. The grayscale is proportional to the dipole power dissipation in logarithmic scale with white and black representing the maximum and minimum values, respectively.

The dipole dissipates power by coupling its radiative field components (with in-plane wavevector component above the light-line) to the planewave modes in the dielectric medium and by coupling its evanescent field components (with in-plane wavevector component below the light-line) to the SPP modes of the structure. The power dissipation traces that fall below the light-line in Figs. 1.2 a and b denote the dispersion characteristics of SPPs supported by the respective structure, with their corresponding in-plane wavevector given by β. For the thin metal slab, the high-ω and low-ω dispersion curves are associated with the LRSPP and SRSPP, respectively. The two curves result from the split of the single-interface SPP dispersion curve due to coupling of individual single-interface SPPs at each metal-dielectric interface.

For small values of ω all SPP modes lay slightly below the light-line indicating that their behaviour is almost photon-like but as ω increases SPPs acquire interesting properties. The dispersion curves of SPPs exhibit an energy asymptote (indicated by the dashed lines in Figs. 1.2 a and b) at $\omega = \omega_p/\sqrt{1+\varepsilon_d} = 0.56\ \omega_p$. For single-interface SPPs and SRSPPs, β increase monotonically with ω approaching to infinity as ω reaches the energy asymptote; conversely, LRSPPs can also exist above the energy

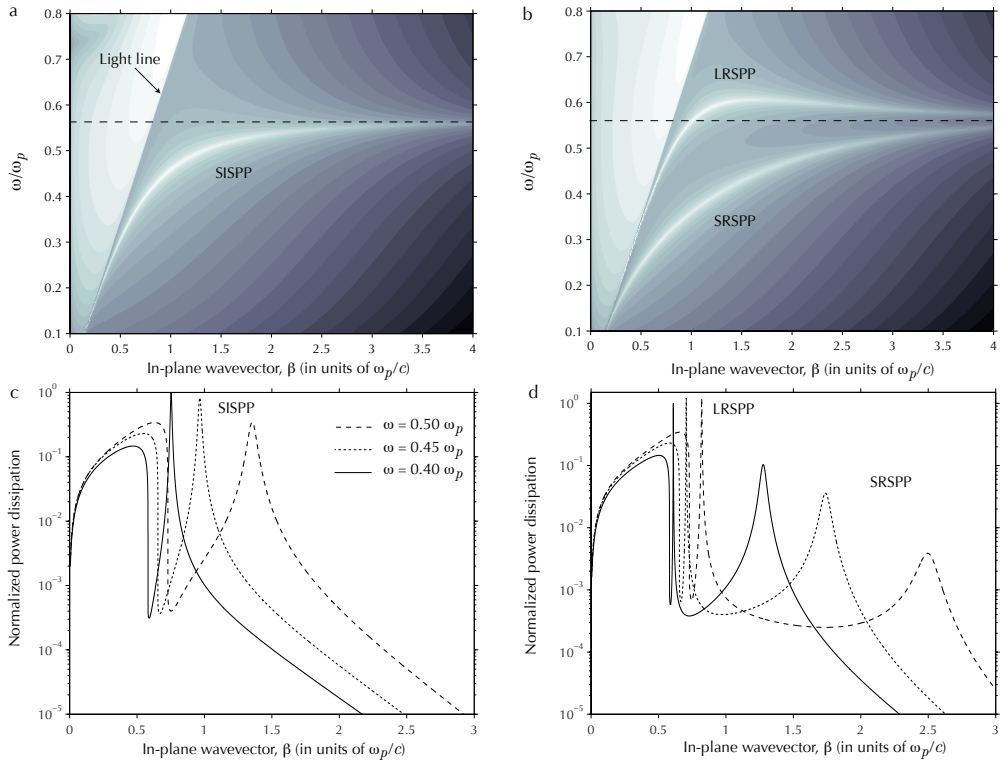

Figure 1.2 | Power dissipation of a y-oriented dipole located 50 nm above the metal surface as a function of the in-plane wavevector for (a) single metal-dielectric interface and for (b) a 20 nm-thick metal slab bounded by dielectrics. The logarithmic grayscale is proportional to the dissipated power with white and black being the maximum and minimum values, respectively. The power dissipation traces that fall bellow the light-line denote the SPP dispersion relations, with their corresponding in-plane wavevector given by β. The dipole's power dissipation spectrum at three angular frequencies are shown in (c) for single metal-dielectric interface and in (d) for the metal slab.

asymptote and β do not increase monotonically with ω. The SPP group velocity, obtained as the rate of change in the slope of the dispersion curve (i.e., $v_g = \partial\omega/\partial\beta$), can be unusually slow, reaching a value of zero at the energy asymptote. Moreover, for LRSPPs there is a region of the dispersion curve where β increases with decreasing ω, implying a *negative* group velocity. The LRSPP attains zero group velocity at the energy asymptote and also at the point where the slope of the dispersion curve changes sign.

The dispersion relation of single-interface SPPs can also be obtained analytically in a straightforward manner [2] and is given by

$$k = \frac{\omega}{c}\left(\frac{\varepsilon_m \varepsilon_d}{\varepsilon_m + \varepsilon_d}\right). \tag{1.3}$$

On the other hand, the dispersion relations of SPPs supported by the metal slab have no explicit analytical form, but can be obtained from the roots of the following

equations [2]

$$0 = \varepsilon_m q_d + \varepsilon_d q_m \tanh(\frac{q_m d}{i2}) \tag{1.4a}$$

$$0 = \varepsilon_m q_d + \varepsilon_d q_m \coth(\frac{q_m d}{i2}), \tag{1.4b}$$

where equation (1.4a) is associated with LRSPPs and (1.4b) with SRSPPs. Here, q_m and q_d are the transverse wavevectors in the metal and in the dielectric, respectively. They are obtained by requiring the conservation of momenta at the metal-dielectric interface as

$$q_{m,d} = i\left[k^2 - \varepsilon_{m,d}\left(\frac{\omega}{c}\right)^2\right]^{1/2}. \tag{1.5}$$

1.1.2 Mode size

The SPP field in the dielectric regions is characterised by the transverse wavevector, q_d, as described by equation (1.5). The imaginary part of q_d defines the penetration depth into the dielectric, which is the distance from the metal surface to the point where the field decays by a factor of e^{-1} in the dielectric region. Since the field's penetration depth into the metal is very small (in the order of few nanometers [11]), the SPP mode size is characterised mainly by the field's penetration depth into the dielectric media. For the two structures presented here, the mode size can be simply obtained as

$$w = \frac{m}{\text{Im } q_d} \approx m\left[\beta^2 - \varepsilon_d\left(\frac{\omega}{c}\right)^2\right]^{-1/2} \tag{1.6}$$

where $m = 1$ for the single-interface SPP and $m = 2$ for the LRSPP and SRSPP. The approximation is made using the fact that $\beta \gg \alpha$. Note that for the metal slab, this expression is valid only when the bonding dielectrics are identical.

The fact that SPPs can have extremely large values of β (see Figs. 1.2a and b) implies through equation (1.6) that their mode size can be extremely small. This property makes SPPs attractive to applications in nano-optics [11, 12].

1.1.3 Propagation loss

The unusual dispersion relations of SPPs are accompanied by propagation losses characterised by the field attenuation coefficient, $\alpha = \text{Im } k$, in equation (1.1). Often the propagation loss is expressed in terms of the distance that the SPP propagates before dissipating most of its power. This distance is called *propagation length*. It is usually defined as the length from the launching point at which the SPP intensity decays by a factor of e^{-1} and is given by [2]

$$l = \frac{1}{2\alpha}. \tag{1.7}$$

The propagation loss of SPPs is manifested as a broadening of the SPP resonance in the momentum space [2, 13]. Figs. 1.2 c and d show the resonance spectrum of the SPPs in question; they are obtained from the dipole's power dissipation spectra as cuts of constant ω. In analogy to the resonance spectrum of a lossy cavity mode, the SPP resonance spectrum is sharp when the SPP loss is low and broad when the loss is high. As the angular frequency approaches to the energy asymptote at large values of β, the SPP resonance spectrum vanishes as it becomes increasingly wide due to the large propagation loss (see Fig. 1.2), thus limiting the effective range of wavevectors β. The SPP propagation loss increases with increasing β because the SPP field becomes more confined to the metal [as it is apparent from equation (1.6)], increasing the power dissipation through ohmic losses. Also, large values of β imply angular frequencies closer to the energy asymptote, where the metal absorbs more efficiently.

Clearly there is always a trade-off between the SPP propagation loss and its field confinement around the metal. Following the previous arguments one can notice that, for the types of SPPs discussed here, LRSPPs have the lower propagation loss and larger mode size, SRSPPs have the higher propagation loss and smaller mode size, and single-interface SPPs lie between these two cases.

1.1.4 Field enhancement

SPP modes can exhibit strong field enhancement with respect to the field of the excitation source [2]. Considering again the case of a dipole radiating in the vicinity of the metal surface, the enhancement follows from a simple focusing effect that takes place as the two-dimensional field emitted by the dipole is transformed into the one-dimensional SPP field. Weber and Ford [14] derived an upper limit for the SPP field enhancement on the basis energy conservation arguments. Their analysis considered the single interface structure in particular. Ignoring the field in the metal and assuming $\mathrm{Re}\,(-\varepsilon_\mathrm{m}) \gg \varepsilon_d$, which is often the case, such an upper limit can be approximated as [14]

$$\left|\frac{\mathbf{E}_{sp}^{+}}{\mathbf{E}_0}\right|^2 \approx \frac{1}{w\alpha}, \tag{1.8}$$

where $\mathbf{E}_{sp}^{+}$ is the SPP electric field just above the metal surface and $\mathbf{E}_0$ is the excitation electric field, which is assumed to be coupled perfectly to the SPP mode. This intuitive expression indicates that the maximum enhancement in the SPP field is given approximately by the inverse product of the field attenuation coefficient and the mode size.

1.2 SPP amplification

The unique properties of SPPs make them valuable in a broad range of scientific fields. For example, the strong field enhancement at the metal surface has applications in spectroscopy [15, 16] and non-linear optics [17]; the strong SPP field confinement promise interesting applications in nanophotonics [18, 19] and imaging [20]; and the high sensitivity to the bounding dielectric environment has been exploited in the development of biosensors [21, 22]. However, a fundamental problem that imposes limitations to many of these applications is the large propagation loss of SPPs at visible and near-infrared wavelengths. To alleviate this problem, researchers have proposed loss compensation through optical amplification. This can be achieved in principle by adding optical gain to the dielectric(s) bounding the metal. As a result, there has been a great interest in understanding the physics of SPP amplification as well as exploring the feasibility of complete SPP loss compensation by this mechanism.

The obvious consequence of reducing SPP propagation losses is, as indicated by equation (1.7), an increase in SPP propagation length. This feature is advantageous for SPP-based biosensors, as it could lead to higher sensitivities [21]. Also, from equation (1.8) one observes that a small attenuation coefficient, α, could result in a huge field enhancement. Finally, the compromise between mode size and propagation loss could be reduced or even eliminated through optical amplification, allowing researchers to exploit the full potential of nano-scale SPP mode dimensions. Thus, the amplification of SPPs is a research area that promises useful practical applications and opportunity to achieve a better understanding of light-matter interactions.

In general, complete SPP loss compensation requires a large amount of gain; the amount varies depending on the type of structure, material properties, and operation wavelength. For example, consider the single-interface SPP supported by the structure in Fig. 1.1 a. It can be shown that the critical gain needed for lossless SPP propagation ($\alpha = 0$) is [23]

$$\gamma = \frac{\omega}{c}\frac{\varepsilon_d''}{\sqrt{\varepsilon_d'}} = \frac{\omega}{c}\frac{\varepsilon_m''\varepsilon_d'^{3/2}}{|\varepsilon_m|^2}, \tag{1.9}$$

where the prime ($'$) and double prime ($''$) indicate real and imaginary parts, respectively, and ε_d'' is a positive quantity indicating that the dielectric provides optical gain. Equation (1.9) assumes that the optical gain is homogeneous and isotropic. As expected, the required optical gain increases linearly with the metal absorption characterised by ε_m''. Yet, more importantly, it increases with the permittivity of the dielectric as $\varepsilon_d'^{3/2}$ (thus, using low index dielectrics to host the gain material is advantageous). Assuming silver as the metal and a laser-dye-doped-glass as the active dielectric, one obtains $\gamma \approx 3833$ cm^{-1} at a wavelength $\lambda = 580$ nm using the permittivity values from Section 1.1.1. As a reference point, the obtained value of γ

is two orders of magnitude larger than typical values achieved in dye-doped-polymer optical amplifiers. Slightly lower gains are required at near-infrared wavelengths (e.g., $\gamma \approx 1200$ cm^{-1} at $\lambda = 1550$ nm [23]) because of the lower metal absorption.

The gain requirements are reduced by approximately an order of magnitude for LRSPPs due to their lower propagation loss [23]. This feature makes LRSPPs attractive for amplification and lasing applications. On the other hand, SRSPPs exhibit extremely large propagation losses and complete loss compensation for this mode does not seem possible because of this reason.

In addition to the large gain needed for lossless SPP propagation, several practical considerations must be taken into account; for instance, gain quenching near the metal, imperfect overlap between the SPP field and the gain medium, gain depletion due to amplified spontaneous emission, and limited pump energy due to potential damage of the metal surface. Some of these issues are addressed in this thesis.

1.3 Literature review

A large number of theoretical and experimental studies have been reported as researchers investigate and put to test new ideas within the context of SPP amplification. This section reviews some of these studies.

1.3.1 Theoretical studies

The first theoretical study on SPP amplification was reported by Plotz and co-workers [25] in 1979 within the context of enhanced total internal reflection. The authors considered a thin silver film ($\sim$ 50 nm-thick) attached to a glass prism on one side (Kretschmann-Raether configuration) and in contact with a gain medium on the other, and explored the reflectivity of the glass-metal interface for different gain values. The gain medium, a fluorescent dye, was assumed to be homogeneous. Their result show that the usual reflectance drop that characterises the SPP resonance decreases monotonically as the gain in the dye region increases, reaching eventually a reflectance that is larger than one; i.e., enhanced total reflection. When this condition is met, a singularity can be generated in the reflectivity expression by choosing an appropriate thickness for the metal slab; physically, this singularity is associated with the coherent out-coupling of SPPs with infinite propagation length.

Almost a decade later, Sudarkin and Demkovic [26] complemented the work by Plotz and co-workers, and proposed for the first time the possibility of an SPP based laser. The authors studied a similar structure and showed that for a specific set of complex dielectric constants describing the metal and gain medium, there is an optimum metal-film thickness for which the ratio of the SPP field intensity at the

metal surface to the intensity of the excitation source is maximum. They noted that for silver films thicker than those considered in Ref.[25] the reflectance does not increase monotonically with the gain. Instead, it decreases with increasing gain (a phenomenon later observed experimentally by Seidel *et al.* [27]) until the gain reaches a specific value where the metal thickness is close to the optimum. As the gain increases beyond this point, the reflectance begins to increase. Despite the non-monotonic reflectance behaviour, the analysis shows that the SPP field increases and the SPP resonance linewidth narrows monotonically with gain increments, as expected for SPP loss reduction. The authors also showed that Fresnel formulae can lead to erroneous results of reflectivity when the diameter of the excitation beam is comparable to the SPP range, an important consideration for systems with high gain.

In 2003 Bergman and Stockman [28] proposed the concept of surface plasmon amplification by stimulated emission of radiation (*spaser*) to create a nanoscopic coherent SPP source. Indeed, a *spaser* could serve as a convenient light source for plasmonic applications, eliminating the need of an external coupling mechanism between photons and SPPs. In their study, the authors considered a metallic nano-particle surrounded by a gain medium in the form of quantum dots (QDs). The nano-particle itself serves as a resonator, which together with the inverted surrounding gain medium form a structure capable of amplifying coherently the localised surface plasmon modes supported by the system, much like the photonic modes of a cavity are amplified in a conventional *laser*.

Around the same time, Ramakrishna and Pendry [29], considered amplification of SPPs to improve the resolution of a near-field lens based on the *perfect lens* proposed by J. Pendry [30]. The *perfect lens* is a slab of left-handed material (a material with negative permeability and permittivity) capable of imaging both propagating and evanescent fields, and thus, with resolution not limited by diffraction. At optical wavelengths, a near-field lens can be constructed from a carefully designed metal slab, where evanescent fields are transported through the lens via a series of SPP resonances; however, the image resolution is degraded by SPP losses. In their study, the authors proposed a near-field lens consisting of a stack of thin alternating layers of silver and semiconductor medium with optical gain. They showed theoretically that such a lens can transport evanescent fields with little attenuation achieving images with sub-wavelength resolution of $\sim \lambda/25$.

Nezhad and colleagues [23] studied SPP amplification in planar metallic structures bounded by an homogeneous gain medium. The authors derived analytical expressions for the material gain needed for lossless propagation, zero wave-front tilt, and bound propagation limit of single-interface SPPs. Considering silver and an InGaAsP-based gain medium they showed that lossless propagation of single-interface SPPs is possible

at $\lambda = 1550$ nm when the material gain is about 1260 cm^{-1}. The authors also studied numerically amplification of LRSPPs supported by a 40 μm-thick silver slab and a 400 μm-wide stripe of the same thickness embedded in an InGaAsP-based gain medium. For these geometries, it was found that the material gain required for lossless propagation is an order of magnitude smaller than for single-interface SPPs. They also investigated the effect of non-uniform gain close to the metal stripe by modelling the gain medium as a layer of thickness h located at a distance d from one of the metal surfaces. Their results showed that for $50 < h < 175$ nm and $0 < d < 200$ nm, the gain needed for lossless propagation increases monotonically as the layer moves away from the stripe. The reported gain values varied from 800 to 4500 cm^{-1} depending on the size and position of the gain layer, which reflects the importance of a good gain-mode overlap.

Avrutsky [31] reported a theoretical study on the behaviour of gain-assisted SPPs and their interaction with nanoscale gratings at frequencies near to the SPP energy asymptote. The study considers SPPs supported at the interface between silver and a dielectric medium with gain in the spectral region of $330 < \lambda < 370$ nm. The author shows that compensating SPP losses at frequencies near to the SPP energy asymptote enables the unusual properties expected due to the singularity in the dispersion relations [i.e., $\varepsilon_m + \varepsilon_d \to 0$ in equation (1.3)] that in the passive case are masked by large optical losses. These properties, which include extremely low group velocity, large effective index, and high field localisation, allow the SPP to interact with features that are an order of magnitude smaller in size than the wavelength. Indeed, these unique properties show potential for characterisation of sub-nanometer surface features and ultra-sensitive optical sensors.

Okamoto and colleagues [32] suggested lasing in the LRSPP supported by a thin corrugated silver film covered by a gain medium in the form of 4-dicyanomethylene-2-methyl-6-p-dimethyl-aminostyryl-4H-pyran (DCM) doped tris-(8-hydroxyquinoline)-aluminium (Alq_3). They pointed out that the medium can provide sufficient gain ($\sim$ 600 cm^{-1}) at $\lambda = 620$ nm to overcome the LRSPP propagation loss in films thinner than 60 nm. In subsequent studies, Okamoto and colleagues investigated theoretically the behaviour of plasmonic bandgaps appearing in the SPP dispersion relations of corrugated thin silver films and determined design conditions for improved performance of a LRSPP plasmonic bandgap laser [33, 34].

Winter and colleagues [35] studied in detail the plasmonic bandgap laser structure suggested by Okamoto in Ref. [32] and questioned the possibility of LRSPP lasing. They discussed the need of considering the power dissipation of excited molecules into SRSPPs also supported by the structure. Photoluminescence measurements on (effectively) symmetric corrugated structures with silver-film thicknesses varying from

20 to 90 nm showed that a significant amount of power is indeed coupled into both SRSPPs and LRSPPs. The authors conducted numerical calculations to estimate the fraction of the power dissipated by excited molecules into LRSPPs and SRSPPs supported by a planar symmetrically cladded silver film as a function of the film thickness and for specific separations, d, between the molecule and the metal surface. The results showed that for a film thickness of 20 nm and $d = 20$ nm excited molecules dissipate about 80% of their power into SRSPPs and only about 7% into LRSPPs. The authors estimated the gain available for LRSPPs and SRSPPs as a fraction of the total gain corresponding to the fraction of power dissipated by an excited molecule at a particular location into the respective mode. Their results suggested that lasing in the LRSPP would be possible only with silver films thinner than about 15 nm.

Maier [36] studied analytically the propagation of SPPs at telecommunication wavelengths in metal-insulator-metal structures with optical gain. The analysed structures are formed by two gold semi-infinite regions separated by semiconductor gain material with thicknesses varying from 5 to 500 nm. It is shown that a sufficiently large gain can completely compensate for the odd-parity coupled SPP mode supported by the metal-semiconductor interfaces. The gain coefficient for complete loss compensation is estimated as 1625 cm^{-1} and 4830 cm^{-1} for structures with semiconductor thicknesses of 500 and 50 nm, respectively.

Alam and colleagues [37] proposed a structure to overcome the SPP losses at telecommunication wavelengths via optical amplification using quantum wells as the gain medium. It consisted of a 1 μm-wide and 10 nm-thick silver stripe on an AlGaInAs multiple quantum well (QW) structure. The metal stripe was covered by a dielectric superstrate of finite thickness and the entire structure was on a semi-infinite InP substrate. The authors conducted a numerical analysis of the structure's optical properties varying systematically parameters such as superstrate and QW barrier refractive indices, and metal and superstrate dimensions. They showed that a 400 nm-thick superstrate with refractive index matched to that of the barrier regions allows a well-guided LRSPP mode despite the structure's large refractive index asymmetry. This design also provided a good balance between SPP mode attenuation ($\sim$ 12 dB/mm) and mode-gain overlap ($\sim$ 6.5%). They found that a material gain of 402 cm^{-1} was required for lossless SPP propagation in this configuration assuming that modal loss was due solely to the metal absorption. The authors pointed out the difficulty of growing a crystalline superstrate on top of a metallic film which can lead to additional losses of up to 35 dB/mm for a poly-crystalline superstrate.

1.3.2 Experimental studies

Amplification of SPPs was first demonstrated at far-infrared wavelengths a decade ago by Capasso and co-workers [38, 39]. In Ref. [39] the authors reported a distributed-feedback (DFB) SPP laser emitting at $\lambda \approx 17$ μm. In part, this plasmonic laser owes its success to the low absorption of metals at far-infrared wavelengths. The device consisted of an alternate sequence of gold (300 nm-thick) and titanium/gold (10/300 nm-thick) stripes deposited on a quantum-cascade (QC) active material. The DFB mechanism was provided by the refractive index difference of the alternating metallic pattern. With this approach, the thickness of epitaxial growth was reduced by a factor of 2.25 and the confinement factor was increased by a factor of 1.8 compared to the respective values of a conventional DFB QC laser with the same active medium. At low temperatures, the laser showed a reduction in the lasing threshold by a factor of two compared to conventional QC lasers operating at similar wavelengths; this allowed a record high power of 38 mW at a temperature of 5K. Furthermore, the laser offered high modal purity with side suppression ratio of approximately 30 dB and operated at a maximum temperature of 240K with a thermal wavelength tenability of ~ 1 nm/K.

The first demonstration of SPP stimulated emission at visible wavelengths was reported by Seidel and colleagues [27] in 2005. They employed structures consisting of a ~ 40 and ~ 65 nm-thick silver films attached to a glass-prism on one side and in contact with a gain medium in the form of optically excited dye molecules in solution on the other side. The authors studied the change in reflectance at the glass-silver interface induced by the gain medium as a function of the incidence angle. Experiments were conducted using two flowing dye solutions, Rhodamine 101 and Cresyl-violet in ethanol, both with a molecular density of $N = 7 \times 10^{17}$ cm^{-3}. TM polarised light from a helium-neon laser at $\lambda = 633$ nm was used to probe the SPPs while the dye molecules were excited via SPP coupling at $\lambda = 580$ nm using light from a dye-laser incident from the glass-silver interface. The pump beam carried a power of 10 mW and was focused to a spot of 60 μm in diameter; it overlapped completely with the probe beam which was focused to an area approximately twice as large. The probe and pump beams were modulated at 23 Hz and 27 MHz, respectively, and a phase-sensitive detection scheme using two lock-in amplifiers was employed to measure the reflectance change due to the SPP stimulated emission. For the 40 nm-thick films, the effect of stimulated SPPs was observed as an increased emission of light into the reflected probe beam; on the other hand, for the 65 nm-thick films it is manifested by the narrowing and deepening of the reflectance dip occurring at the SPP resonance angle. The experimental results agreed qualitatively with a theoretical model that considers the gain medium as a 4-level system and a number of factors characteristic of the experiment, such as the exponential decay of population inversion away from

the metal surface and the transverse profile of the probe and pump beams.

Noginov and colleagues [40] studied experimentally SPP amplification in a structure similar to that used by Seidel in Ref. [27]. In this case, a 40 nm-thick silver film was coated on one side by a 10 μm layer of Rhodamine-6G (R6G) doped polymethylmethacrylate (PMMA) and attached to a glass prism on the other side. The density of dye molecules was $N = 2.2 \times 10^{22}$ cm^{-3}. The gain medium was optically pumped directly from the PMMA side using normally incident $\lambda = 532$ nm pulsed light with pulse energy of 18 mJ, a pulse duration $t_p = 10$ ns and repetition rate of $f_p = 10$ Hz. The SPP was coupled (probed) through the prism using TM polarised light from a helium-neon laser at $\lambda = 594$ nm. The reflected probe light was spectrally filtered using a monochromator tuned to the probe wavelength and then measured as a function of the probe's incidence angle using a photomultiplier tube. Stimulated emission of SPPs was observed as an increase in the reflected probe light, consistent with the observations previously reported by Seidel and colleagues [27]. Based on the reflectance measurements, the authors estimated an SPP loss reduction of 35%.

In a subsequent study [41], Noginov and colleagues measured the fluorescence decoupled from the prism side as the gain medium was pumped. For this experiment, the structures employed were similar to those reported in Ref. [40] but with a thinner (3 μm-thick) gain medium. In addition to the characteristic angular profile of decoupled SPPs, the authors observed attributes of stimulated emission. They reported spectral narrowing at high pump intensities and a non-linear intensity behaviour of the decoupled light with respect to the pump intensity, which exhibited a distinct threshold point. On the basis of a theoretical model, the authors claimed that the observations correspond to those expected for amplified SPP propagation when the losses are overcome entirely.

Lasing in metallic nano-cavities was first demonstrated by Hill and colleagues [42] at telecommunication wavelengths. Such a nano-laser consisted of an electrically pumped InP-InGaAs-InP double heterostructure gain medium shaped in the form of a circular pillar. The pillar was grown on a p-InGaAsP layer on a Si-InP substrate, and a thick gold layer covered the entire structure. The pillar's height and width were approximately 250 nm, 300 nm, respectively. The continuous wave (CW) lasing properties were analysed at cryogenic temperatures by measuring light leaking through the base of the structure. The laser covered single mode emission over a broad wavelength range (1418 nm $< \lambda <$ 1452 nm) by varying the pillar's diameter over 30 nm. At temperatures of 10K and 77K, respectively, the laser exhibited lasing thresholds of 3.5 μA and 6 μA and quality factors of 200 and 140. Finally, the spectral linewidth measured at 10K was approximately 1 nm for pump currents ranging from 25 to 150 μA and as narrow as 0.3 nm for higher currents.

In a subsequent study [43], Hill and colleagues reported lasing at telecommunication wavelengths in metallic nano-cavities similar to those used in Ref. [42]; however, in this case the semiconductor structure was shaped in the form of a rectangular pillar and covered with a thick layer of silver. The structures were 300 nm in height with widths varying from 90 nm to 350 nm and lengths of the order of microns; hence, supporting Fabry-Perot modes. The authors characterised the laser's CW operation at a temperature of 78K, reporting a lasing threshold of 40 μA and a quality factor of $\sim$ 370 for a 130 nm wide and 3 μm long device. In addition, they demonstrated pulsed laser operation at room temperature reporting a lasing threshold peak current of $\sim$ 5 mA and a quality factor of $\sim$ 340 for a 310 nm wide and 6 μm long device.

Ambati and colleagues [44] observed stimulated emission of LRSPPs at telecommunication wavelengths using a propagating pump-probe arrangement. The structure consisted of a 8 μm-wide by 20 nm-thick gold stripe embedded in erbium-doped glass gain medium. The insertion loss of a 8 mm-long waveguide was measured as 39 dB, which includes the ground-state absorption of erbium ions, the LRSPP propagation loss, and other loss mechanisms such as coupling and scattering losses. Presumably, structures of this length were used for stimulated emission experiments. The pump ($\lambda = 1480$ nm) and probe ($\lambda = 1532$ nm) signals were coupled simultaneously into the LRSPP supported by the metal stripe using a polarisation-maintaining fibre in order to study the LRSPP stimulated emission in pulsed and CW operation. For the pulsed analysis, a 500 μs pump pulse was followed by a 150 μs probe pulse with a time delay between them of 30 μs and the probe signal enhancement was measured as a function of the pump power. The authors reported a maximum enhancement of 0.74 dB with a pump power of 92 mW and of 1.73 dB with a pump power of 266 mW in pulsed and CW operation, respectively. As evidenced by measurements, the spontaneous emission into the LRSPP mode is practically none, thus ruling out this phenomenon as part of probe's enhancement.

Grandidier and colleagues [45] demonstrated an increase in propagation length of SPPs supported by a polymer loaded metallic waveguide at a telecommunication wavelength. The waveguides consisted of 600 nm-thick by 400 nm-wide PMMA stripes doped with lead sulfide (PbS) QDs fabricated on a 40 nm-thick gold film. The waveguides were 64 μm in length and the QD concentration is $\sim 9 \times 10^{16}$ cm^{-3}. The QD emission spectrum exhibited a broad peak near $\lambda = 1550$ nm, the probe light wavelength used in the experiments. The gain medium was pumped using CW light at $\lambda = 532$ nm homogeneously distributed over the waveguide. The SPP propagation length as a function of the pump power was measured via leakage radiation microscopy [46]. They reported a maximum increase in SPP propagation length of 27% achieved with a pump power of 1000 W/cm^2, with corresponding a gain in the

polymer of ~ 600 cm^{-1}. The authors claimed that the considerable increase in propagation length was not the result of thermal variations induced by the pump light at such high intensities. For this, they provided evidence of a narrowing in the momentum components of the amplified SPP, an expected behaviour observed previously also by Noginov [41] and Seidel [27].

Oulton and colleagues [47] demonstrated lasing in hybrid-plasmon modes supported by a thick silver film coupled to a cadmium sulphide (CdS) nano-wire that served as the gain medium. The CdS nano-wire was separated from the silver film by a thin magnesium fluoride insulating layer, where the hybrid plasmon mode concentrated most of its energy [48]. The gain medium was optically pumped with pulsed light at $\lambda_p = 405$ nm ($t_p = 100$ fs; $f_p = 80$ MHz). The emitted light coupled out of the structure was studied for a number of structures with different insulating layer thickness and CdS nano-wire dimensions. The amplified spontaneous emission (ASE) threshold was estimated as the pump intensity for which the Fabry-Perot modes of the cavity were discernible on the measured light spectrum. For structures with a 5 nm insulating layer and CdS nano-wire diameter ranging from 100 nm to 400 nm, the authors reported ASE thresholds that occurred between 10 to 60 MW/cm^2. For pump intensities above these thresholds a non-linear output-power versus pump-intensity relation developed indicating laser action. A six-fold enhancement in the spontaneous emission rate when compared to a photonic laser consisting of a CdS nano-wire on quartz was observed for a CdS nano-wire with a diameter of ~ 120 nm. This enhancement was attributed to the high mode confinement. The authors pointed out that the transition from spontaneous emission to lasing in the output-power versus pump-intensity relation of the hybrid-plasmon laser did not show the typical 'kink' characteristic of photonic lasers.

Noginov and colleagues[50] reported SPP lasing in metallic nano-particles according to the spaser concept introduced earlier by Bergman and Stockman [28]. The spaser design consisted of a 44 nm-diameter nano-particle formed by a 14 nm-diameter gold core embedded in a 15 nm thick dye-doped silica shell. The dye employed (Oregon Green 488) emitted in a band centred about $\lambda \approx 510$ nm and overlapped well with the broad SPP resonance spectrum supported by the gold nano-particle, which peaked at $\lambda \approx 520$ nm. The number of dye molecules per nano-particle was estimated as 2.7×10^3. An aqueous nano-particle suspension with nano-particle density of 3×10^{11} cm^{-3} was placed in a cuvette with 3 mm path-length. The suspension was pumped using pulsed light ($t_p = 5$ nm) at $\lambda = 488$ nm focused to a 2.4 mm diameter spot. The authors observed laser-like emission at $\lambda = 531$ nm with an intensity that exhibited a non-linear behaviour with respect to the pump energy, showing a lasing threshold at ~ 5 mJ. The authors noticed that reducing the nano-particle density

did not change considerably the emission characteristics. Hence, they concluded that the laser-like behaviour was produced by individual nano-particles (as predicted in Ref. [28]) and not by a collective feedback mechanism in the nano-particle suspension.

Bolger and colleagues [51] studied experimentally SPP ASE and the gain limitations that it imposes on SPP amplification. Experiments were conducted on gold films of various thicknesses (25, 50, and 100 nm-thick) deposited on a silica substrate and cladded with a 1 μm-thick gain medium in the form of PMMA doped with PbS QDs. The QDs concentration was 5 wt.%. The SPP mode supported at the polymer-gold interface was used for the analysis. Pairs of gratings separated by several distances were fabricated on the gold film in order to couple light in and out of the plasmonic structure. The SPP was probed via QD-photoluminescence generated using a helium-neon laser at $\lambda = 633$ nm directed at one of the gratings and the gain medium was pumped with a second helium-neon laser focused to a 100 μm-diameter spot located between the two gratings. The SPP emission spectra coupled out of the structures peaked at $\lambda \approx 1160$ nm and exhibited a significant linewidth narrowing as a function of the pump intensity. The emission linewidth reached its minimum value with a pump intensity of ~ 10 W/cm^2 and remained so for higher pump intensities. The authors estimated the pump intensity for the SPP ASE on-set as ~ 5 W/cm^2. They reported a maximum increase in propagation length of 30% achieved with a pump intensity of ~ 1 W/cm^2. For higher pump intensities the propagation length decreased, eventually reaching values comparable to those measured in the absence of the pump. This was attributed to a reduction of available gain caused by the competition of SPP ASE and amplified input SPP.

1.4 Thesis scope and outline

This thesis aims to provide deeper insights on the physics of surface plasmon-polariton amplification and spontaneous emission in surface plasmon-polariton amplifiers through theoretical and experimental vehicles applied (but not necessarily restricted) to LR-SPPs. The scope of this thesis comprises three important points:

- *The development of a realistic theoretical model to describe SPP amplification in planar plasmonic structures:* Photons and SPPs are amplified through the same process (i.e., stimulated emission), however, the conditions under which this process occurs are different in a SPP amplifier. The presence of the metal modifies the electromagnetic environment in its vicinity and affects the gain medium near the surface, where the SPP field is localised. A realistic model for SPP amplification must therefore consider the presence of the metal to describe accurately the amplification process. This thesis presents a theoretical model for

SPP amplification in planar structures incorporating dipolar gain media. The model accounts for (i) the inhomogeneous gain distribution near the metal surface caused by a non-uniform excitation of dipoles and by near-field phenomena occurring in the vicinity of the metal surface, and (ii) the overlap between the gain and SPP-mode distributions. The model is not restricted to the analysis of LRSPPs but it can be applied directly to other plasmon modes supported by the planar structure.

- *Experimental demonstration of complete SPP loss compensation:* Previous studies have presented evidence of complete loss compensation in SPPs through indirect vehicles such as a theoretical interpretation of SPP stimulated emission [41] or through the observation of laser-like behaviour of light coupled out of active plasmonic structures [42, 43, 47, 50]. This thesis presents a direct measurement of gain in the LRSPP supported by a symmetric gold-stripe plasmonic waveguide incorporating a gain medium in the form of optically pumped dye molecules in solution.

- *Study of spontaneous emission in SPP amplifiers:* In the context of SPP amplification, only few studies [51, 47] have addressed to some extent the implications of spontaneous emission near metallic surfaces. Furthermore, no experimental studies have addressed this phenomenon specifically in LRSPP amplifiers so far. This thesis presents an experimental study of spontaneous emission into the LRSPP supported by the structure described above. A theoretical model is proposed, which is not limited to the analysis of the LRSPP but can be applied directly to other plasmon modes in planar metallic structures. The validity of the theoretical model applied to LRSPPs is confirmed through experimentation.

This thesis consists of a collection of scientific articles, each of them presented as a chapter. The remainder of this document is organised as follows. Chapter 2 describes a theoretical model to study SPP amplification in one-dimensional planar metallic structures incorporating a dipolar gain medium taking into account the non-uniformity of the gain medium close to the metal surface due to position-dependant dipole lifetime and pump irradiance distribution. Chapter 3 employs this model to study SPP amplification in two important plasmonic structures, the semi-infinite metal and the metal slab (see Fig. 1.1). Chapter 4 reports experimental results of gain in propagating plasmons using the LRSPP supported by a symmetric metal stripe waveguide that incorporates optically pumped dye molecules in solution as the gain medium. Chapter 5 reports experimental measurements of spontaneous emission noise into the LRSPP mode supported by a plasmonic amplifier similar to that studied in Chapter 4. Chapter 6 describes the experimental setup and techniques used to obtain measure-

ments of gain and noise in LRSPP active waveguides. Finally, Chapter 7 presents the conclusions and suggestions for future work. Information regarding the measurement instrumentation settings and automation software employed in the experiments are included in appendices A and B, respectively.

CHAPTER 2

Theory of SPP amplification in planar structures

2.1 Summary

A theoretical model is proposed to study SPP amplification in one-dimensional planar metallic structures incorporating a dipolar gain medium, such as dye molecules, rare-earth ions, or quantum dots. The model takes into account the non-uniformity of the gain medium close to the metal surface due to position-dependant dipole lifetime and pump irradiance. The position-dependent lifetime is incorporated into the model through the CPS (Chance-Prock-Silbey) classical theory for molecular fluorescence and energy transfer near interfaces [54] as reformulated by Ford and Weber [55]. The non-uniform pump irradiance distribution throughout the plasmonic structure is calculated using a transfer-matrix formalism [56]. The rate equations for the standard 4-level model are then applied locally, with the lifetime and irradiance taking on their position-dependant values, leading to a non-uniform small-signal planewave gain distribution. The distribution is then discretised and incorporated into a multi-layer waveguide mode solver [57] from which mode power gains are computed for the modes of the system.

2.2 Contribution

The results provided in this chapter were published as a *Rapid Communication* in the journal *Physical Review B*. I formulated the theoretical model, implemented the numerical methods, generated and interpreted the results, and wrote the manuscript. Dr. Berini contributed to the theoretical formulation, the interpretation of the results, and revised the manuscript.

2.3 Article

The published article follows verbatim.

PHYSICAL REVIEW B **78**, 161401(R) (2008)

Theory of surface plasmon-polariton amplification in planar structures incorporating dipolar gain media

Israel De Leon* and Pierre Berini†

School of Information Technology and Engineering (SITE), University of Ottawa, 161 Louis Pasteur, Ottawa, Ontario, Canada K1N 6N5

(Received 13 June 2008; published 3 October 2008)

We investigate theoretically surface plasmon-polariton (SPP) amplification in planar metallic structures taking into account the nonuniformity of the gain medium close to the metal surface due to position-dependent dipole lifetime and pump irradiance. We propose a model that accounts for these nonuniformities and apply it to a physically realizable structure consisting of a thin silver film cladded on one side by a lossless dielectric and on the other by an optically pumped Rhodamine 6G dye solution. We study amplification of the supported long-range SPP mode and show that net amplification is possible at visible wavelengths using reasonable pump power and molecular concentration. It is shown that the gain nonuniformity close to the metal surface must be considered to describe adequately the SPP amplification phenomenon.

DOI: 10.1103/PhysRevB.78.161401 PACS number(s): 73.20.Mf, 78.20.Bh, 78.45.+h

Surface plasmon polaritons (SPPs) are electromagnetic waves coupled to free electron oscillations that propagate along the interface between a dielectric and a metal with a negative real part of permittivity.[1] Their unique properties offer promise for numerous applications.[2] Yet, a fundamental limitation is their short propagation length resulting from power dissipation in the metal. Recently, considerable efforts have been devoted to compensate for the SPP losses in planar structures by using gain media to achieve mode amplification.[3–10] It has been suggested that incorporating gain in such structures could also lead to the realization of SPP lasers at visible wavelengths.[11,12] Indeed, SPP lasers have already been demonstrated at midinfrared wavelengths.[13] Improved resolution of near-field lenses through amplification of SPPs[14] and the interaction of gain media with surface plasmons in metallic nanoparticles[15,16] have been also investigated.

In this growing research area, understanding the characteristics of the gain medium close to the metal surface is of major importance. For this, two factors must be carefully considered. The first factor is the excited state lifetime of dipolar gain media such as organic dye molecules and rare-earth ions, or equivalently, the recombination lifetime of semiconductor gain media such as quantum wells and quantum dots. It is well known that these lifetimes are quenched by a metallic surface due to additional decay channels through which the dipole (or electron-hole pair) relaxes.[17–19] This phenomenon certainly affects the gain available close to the metal. The second factor is the method used to pump the gain medium. In particular, for optically pumped gain media, the irradiance[20] distribution of the pump signal is generally not uniform near the metal. As a result of these factors, a uniform-gain picture is not adequate in the vicinity of a metallic surface.

In treating the amplification of SPP modes, the nonuniformity of the gain close to the metal has generally been neglected (in some cases justified) by assigning a uniform complex permittivity to the gain medium and solving Maxwell's equations in the active structure. A simplified approach was used by Okamoto *et al.*,[11] where the SPP gain is estimated by assuming a uniform gain medium and using bulk-plane-wave amplification arguments. Winter *et al.*[12] further analyzed the structure proposed by Okamoto *et al.*,[11] pointing out the need to account for additional decay channels.

In this Rapid Communication, we investigate how SPP amplification in planar structures is affected by a nonuniform gain distribution close to the metal surface. We propose a theoretical model to describe this phenomenon in structures incorporating dipolar gain media. Our approach consists in obtaining the gain distribution near the metal surface employing position-dependent expressions for the dipole lifetime and pump irradiance. The former accounts for all of the decay channels through which the dipole relaxes and the latter accounts for the pump-signal interaction with the structure. The SPP mode amplification is then computed by solving Maxwell's equations in the active structure using the inhomogeneous complex permittivity describing the gain distribution. This concept can be extended to semiconductor gain media as well by representing adequately the gain distribution in the vicinity of the metal surface.

For the analysis we consider the structure shown in Fig. 1. It consists of a 20-nm-thick silver film extending infinitely over the (x,z) plane. The bottom cladding consists of 25 μm of CYTOP, a lossless dielectric, which in turn sits on a semi-infinite silicon substrate; the top surface is covered by Rhodamine 6G (R6G) dye molecules in a mixture of ethanol and methanol. A semi-infinite CYTOP superstrate lies on top of the dye solution, holding it to within a 5-μm-thick layer. Dye molecules are assumed to be excited from the top by a monochromatic pump signal of wavelength λ_p=532 nm [frequency-doubled Nd:YAG (yttrium aluminum garnet)],

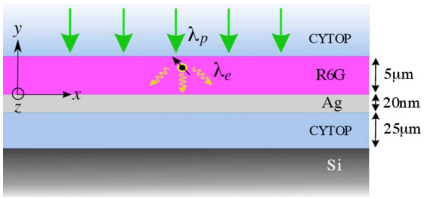

FIG. 1. (Color online) The SPP waveguide structure considered in this work.

TABLE I. Relative permittivities (ϵ_r) at λ_p=532 nm and λ_e =560 nm. *57% methanol 43% ethanol is assumed.

Material	$\epsilon_r(\lambda_p)$	$\epsilon_r(\lambda_e)$
Silver[25]	$-10.18-i0.8311$	$-11.68-i0.8283$
Silicon[25]	$17.22-i0.3646$	$16.42-i0.2936$
CYTOP[26]	1.8053	1.8039
Dye solvent* [23]	1.8068	1.8039

which is near the peak absorption of R6G. SPP mode amplification is analyzed at the peak emission wavelength of the dye, λ_e=560 nm. We approximate the parameters of R6G as those in pure methanol[21] since the dye performs similarly in both solvents.[22] We study the case where the real permittivity of the dye solution is matched to that of CYTOP at λ_e. This can be achieved using a solvent mixture of approximately 57% methanol and 43% ethanol.[23] Such a symmetric structure supports nonleaky short-range SPP (SRSPP) and long-range SPP (LRSPP) modes.[24] Table I lists the material relative permittivities at the two wavelengths of interest. The proposed structure and pumping arrangement are physically realizable and could serve directly as a validation vehicle for the theory proposed herein with the LRSPP coupled in and out of the structure via end-fire coupling.

The basic electronic dynamics of organic dye molecules can be approximated by the rate equations of a four-level system.[27] The steady-state solution gives the following small signal amplification coefficient at λ_e:

$$\alpha_e = N\frac{I_p\tau\sigma_p\sigma_e - \sigma_a\hbar\omega_p}{\hbar\omega_p + I_p\tau\sigma_p}, \tag{1}$$

where N is the total molecular density, I_p is the pump irradiance, τ is the excited-state lifetime, σ_e and σ_a are, respectively, the emission and absorption cross sections at λ_e, σ_p is the absorption cross section at λ_p, ω_p is the pump angular frequency, and $\hbar$ is the reduced Plank constant. This expression is valid for continuous-wave and pulsed pump signals provided that the pulse width is considerably longer than τ. To understand the gain distribution close to the metal we shall identify adequate expressions for τ and I_p.

Following the treatment by Ford and Weber[17] we model the molecule as classical dipole and examine its excited state lifetime in the presence of a thin metal film. Far from the metal, the lifetime is unaffected and is given by the usual definition, $\tau_0=[\gamma_{nr}+\gamma_r]^{-1}=\phi/\gamma_r$, where γ_r denotes the radiative decay rate, γ_{nr} accounts for all the nonradiative (NR) decay channels intrinsic to the dipole, and ϕ is the dipole's quantum efficiency (ϕ=0.9 for the present case[21]). However, close to the metal film, γ_r is replaced by the sum of four decay channels that arise from coupling of the dipole to (1) LRSPP and (2) SRSPP modes, where the dipole emits a SPP instead a photon; (3) coupling to electron-hole (EH) pairs in the metal film, where the energy is directly transferred from the dipole to the metal in a dipole-dipole interaction; and (4) coupling to the radiation modes of the structure. The decay rates into these four channels are affected by the dipole's position and dipole-moment orientation, while γ_{nr} is assumed to be independent of the environment. For the structure under analysis, we write the position-dependent decay rate normalized to the decay rate far from the silver film as

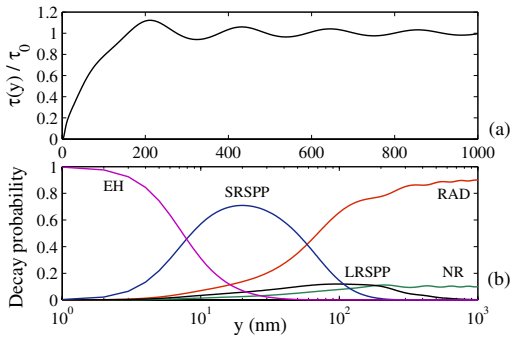

FIG. 2. (Color online) (a) Normalized lifetime computed using Eq. (3). (b) Decay probabilities into each decay channel.

$$\hat{\gamma}^{h,v}(y) = \hat{\gamma}_{nr} + \phi\sum_{i}^{4}\hat{\gamma}_i^{h,v}(y), \tag{2}$$

where y is the dipole's position; $\phi\hat{\gamma}_i^{h,v}$ denotes the normalized decay rates of the four decay channels for (h) horizontal and (v) vertical dipole-moment orientations with respect to the metal plane; and $\hat{\gamma}_{nr}=1-\phi$ is the normalized nonradiative decay rate.

The rates in Eq. (2) are obtained by numerical integration of Eq. (3.30) in Ref. 17 using the local model for silver permittivity and the material permittivities of the structure at λ_e. The integral runs over all wave-vector components parallel to the silver plane, $k_{\|}$. We set its upper limit to $k_{\|}$ =$2.2k_F$ (k_F being the Fermi wave vector) to account approximately for electron screening, which becomes important when the dipole separation from the silver surface is less than a few nanometers. The limit employed corresponds to the upper limit of the EH excitation continuum in silver at λ_e.[17]

Averaging Eq. (2) over the dipole orientations yields the expression for the lifetime of an isotropically oriented dipole,

$$\tau(y) = \tau_0\left[\frac{2}{3}\hat{\gamma}^h(y) + \frac{1}{3}\hat{\gamma}^v(y)\right]^{-1}. \tag{3}$$

Figure 2(a) shows the result of Eq. (3) normalized to τ_0. Note that the lifetime is strongly quenched for distances below ~150 nm and it is practically unaffected when the distance reaches 1 μm. The quenching and oscillatory features are due to the different competing decay channels previously mentioned. To understand the effect of each decay channel on the lifetime we show in Fig. 2(b) their decay probabilities. This probability is defined as the ratio of the particular decay rate over the total decay rate, both for an isotropic dipole. Note that coupling to EH pairs and to the SRSPP mode dominate for distances below 60 nm, causing the strong lifetime quenching within this region. On the other hand, for distances between 60 and 150 nm, the lifetime quenching is mainly due to coupling to SRSPP and LRSPP modes. Finally, coupling to radiation modes (RAD) of the structure

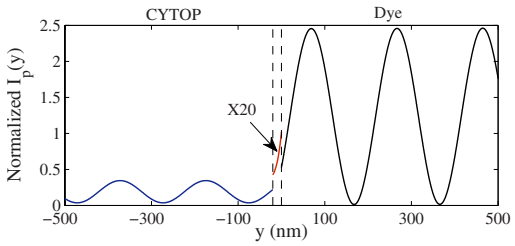

FIG. 3. (Color online) Normalized pump irradiance distribution in the vicinity of the silver film. The irradiance in the silver film is magnified 20 times.

and the NR relaxation dominate above 200 nm being only weakly affected by the LRSPP decay channel.

Although Eq. (3) denotes the lifetime of a *single* dipole, the same expression must hold for a homogeneously distributed collection of them assuming that the interactions between dipoles can be neglected. Such interactions have been observed under large dye concentrations. For R6G in methanol this effect is not significant for concentrations lower than ~5 mM.[21]

We now consider in some detail the spatial dependence of the pump signal. It is taken as a linearly polarized plane wave that illuminates the structure from the top with propagation direction normal to the metal surface. The electric-field distribution across the structure is computed rigorously with a matrix formalism.[28] In the calculations we use the material relative permittivities at λ_p and take the dye relative permittivity as $\epsilon_{r,p}=\epsilon'_{r,p}-iN\sigma_p(\epsilon'_{r,p})^{1/2}\lambda_p/2\pi$, where $\epsilon'_{r,p}$ is the relative permittivity of the dye solvent. Here, we assumed that all the dipoles are in the ground state. This approximation is well justified for a thin dye layer.

The pump irradiance distribution in each medium is computed as[29]

$$I_p(y)=\frac{\mathrm{Re}(\eta)}{2|\eta|^2}|E_p(y)|^2, \tag{4}$$

where $E_p(y)$ is the pump electric-field distribution and η is the medium's characteristic impedance. Figure 3 shows $I_p(y)$ in the vicinity of the silver film normalized to the irradiance of the incoming pump signal. The vertical dashed lines outline the silver film. The lower-cladding thickness was chosen to minimize the resonant coupling to the slab mode. In the dye, the irradiance follows a standing-wave pattern due to field reflection throughout the structure. It presents ~2.5 fold maxima, which enhances the population inversion in those regions. On the other hand, the minima are close to zero, suggesting that population inversion is not possible in those regions.

Substituting Eqs. (4) and (3) into Eq. (1) one obtains a local expression for the gain of the dye, $\alpha_e(y)$. Notice that dipoles in regions where $I_p(y)\approx 0$ or $\tau(y)\approx 0$ act merely as absorbers at λ_e since $\alpha_e(y)\approx -N\sigma_a$. The relative permittivity of the dye at λ_e is then

$$\epsilon_{r,e}(y)=\epsilon'_{r,e}+i\frac{\lambda_e}{2\pi}\alpha_e(y)\sqrt{\epsilon'_{r,e}}, \tag{5}$$

where $\epsilon'_{r,e}$ is the relative permittivity of the dye solvent.

TABLE II. MPG of the LRSPP for the cases under analysis.

Case	A	B	C	Passive
MPG[cm^{-1}]	2.9047	26.4756	22.3423	−105.3036

We proceed to study the amplification of SPP modes. The mode propagation is taken along the $+z$ axis having a complex phase of the form $\exp(-ikz)$, with $k=\beta+i\alpha$ being the complex propagation constant. Thus, a positive (negative) value for α indicates amplification (attenuation) as the mode propagates in the $+z$ direction. The inhomogeneous gain medium is treated as a multilayer structure by discretizing Eq. (5) along the y axis. Then, the transfer matrix method (TMM) (Ref. 30) is used to compute the SPP mode. We assume a R6G concentration of $N=3$ mM ($\sim 1.8\times 10^{18}$ cm^{-3}) and a pump irradiance of 210 $\mathrm{kW/cm}^2$. The parameters for R6G are taken from Ref. 21 as $\sigma_e=3\times 10^{-16}$ cm^2, $\sigma_p=4\times 10^{-16}$ cm^2, $\sigma_a=1\times 10^{-17}$ cm^2, and $\tau_0=3.9$ ns. The gain medium is segmented in 15 000 layers of equal thickness and the TMM analysis is carried out at λ_e using the corresponding material relative permittivities.

To visualize the impact of nonuniform gain distribution near the metal we consider three cases. Case (A) computes the SPP mode in the active structure taking into account both pump and lifetime position dependence. The other two cases use only a partial approach. Case (B) accounts for the pump distribution but assumes a uniform lifetime $\tau=\tau_0$, while case (C) assumes a uniform gain distribution, neglecting both pump and lifetime position dependence.

We shall focus on the nonleaky LRSPP mode supported by the structure. It has lower propagation loss than the SR-SPP mode, which makes it attractive for amplification and lasing applications. The results are summarized in Table II that lists the mode power gain, MPG=2 Im(k), for each case. It also includes the value for the passive case, i.e., when no R6G molecules are present in the solvent. The mode effective index, $n_{\mathrm{eff}}=\lambda_e\,\mathrm{Re}(k)/2\pi$, was evaluated as $n_{\mathrm{eff}}=1.3613$ for all the cases listed in Table II. We note that cases (B) and (C) give similar results, predicting MPG values around 25 cm^{-1}. However, the MPG value for (A) is approximately an order of magnitude smaller. In terms of pump requirements, we found that case (A) requires an extra ~100 $\mathrm{kW/cm}^2$ of irradiance to match the gain predicted by the other two cases.

To understand the difference in these results we consider Fig. 4. It shows the LRSPP mode and gain distributions for the three cases (the mode distribution is practically identical for the three cases). Since mode amplification is a stimulated emission process, it is necessary for the gain and mode distributions to overlap efficiently. For cases (B) and (C) the overlap turns out to be very similar, resulting in similar MPG values. On the other hand, for case (A), the gain is strongly suppressed due to the lifetime quenching. In fact, the medium becomes absorptive within the first few nanometers from the metal surface. This reduces the overlap leading to a smaller MPG. The large discrepancies observed between cases (A) and (B) highlight the importance of accounting for the decay channels of the structure in the analysis of SPP amplification.

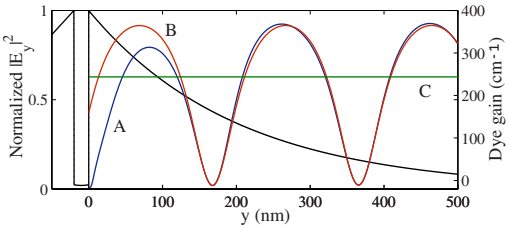

FIG. 4. (Color online) LRSPP mode and gain distributions for the cases under analysis.

Although small, the MPG for case (A) is still positive indicating net amplification. Moreover, larger MPG values seem to be practically attainable since we have assumed a modest R6G concentration and the assumed pump irradiance is well below the output of typical pulsed frequency-doubled Nd:YAG lasers. This suggests that lasing at visible wavelengths should be possible using the LRSPP mode of the proposed structure, provided that the cavity losses are not too high. In addition, the use of a finite width structure (i.e., a silver stripe)[31] would relax the lasing requirements since the mode has a lower propagation loss and the field distribution overlaps better with the gain medium. On the other hand, amplification of the SRSPP mode is quite challenging due to its large intrinsic propagation loss. For instance, considering case (A) one finds MPG=−16438 cm^{-1}.

We note that our results are more optimistic that those reported by Winter *et al.*[12] The reason is because their model limits the gain available to the LRSPP to a fraction equal to the decay probability into this mode. Thus, following their approach, one realizes from Fig. 2(b) that the small decay probability into the LRSPP leads to a small amplification.

In summary, we proposed a theoretical model to describe the amplification of SPP modes in planar structures using optically pumped dipolar gain media. It accounts for the nonuniform gain distribution in close proximity to the metal and its overlap with the SPP mode. We apply the model to study the amplification of the LRSPP mode in a physically realizable structure using R6G molecules in solution as the gain medium. The results suggest that LRSPP net amplification in the visible is feasible using reasonable pump power and molecular concentration. The analysis shows that the gain nonuniformity close to the metal surface resulting from the position-dependent dipole lifetime and pump mechanism must be considered to describe adequately the SPP amplification phenomenon.

*[redacted]
*[redacted]

[1] H. Raether, *Surface Plasmons on Smooth and Rough Surfaces and on Gratings* (Springer, Berlin, 1988).
[2] W. L. Barnes, A. Dereux, and T. W. Ebbesen, Nature (London) **424**, 824 (2003).
[3] G. A. Plotz, H. J. Simon, and J. M. Tucciarone, J. Opt. Soc. Am. **69**, 419 (1979).
[4] A. N. Sudarkin and P. A. Demkovich, Sov. Phys. Tech. Phys. **34**, 764 (1989).
[5] J. Seidel, S. Grafstrom, and L. Eng, Phys. Rev. Lett. **94**, 177401 (2005).
[6] M. A. Noginov, V. A. Podolskiy, G. Zhu, M. Mayy, M. Bahoura, J. A. Adegoke, B. A. Ritzo, and K. Reynolds, Opt. Express **16**, 1385 (2008).
[7] I. Avrutsky, Phys. Rev. B **70**, 155416 (2004).
[8] S. A. Maier, Opt. Commun. **258**, 295 (2006).
[9] M. P. Nezhad, K. Tetz, and Y. Fainman, Opt. Express **12**, 4072 (2004).
[10] M. Z. Alam, J. Meier, J. S. Aitchison, and M. Mojahedi, Opt. Express **15**, 176 (2007).
[11] T. Okamoto, F. H'Dhili, and S. Kawata, Appl. Phys. Lett. **85**, 3968 (2004).
[12] G. Winter, S. Wedge, and W. L. Barnes, New J. Phys. **8**, 125 (2006).
[13] A. Tredicucci, C. Gmachl, F. Capasso, J. E. Hutchison, D. L. Sivco, and A. Y. Cho, Appl. Phys. Lett. **76**, 2164 (2000).
[14] S. Anantha Ramakrishna and J. B. Pendry, Phys. Rev. B **67**, 201101(R) (2003).
[15] D. J. Bergman and M. I. Stockman, Phys. Rev. Lett. **90**, 027402 (2003).
[16] M. A. Noginov, G. Zhu, M. Bahoura, J. Adegoke, C. E. Small, B. A. Ritzo, V. P. Drachev, and V. M. Shalaev, Opt. Lett. **31**, 3022 (2006).
[17] G. W. Ford and W. H. Weber, Phys. Rep. **113**, 195 (1984).
[18] A. Neogi, C. W. Lee, H. O. Everitt, T. Kuroda, A. Tackeuchi, and E. Yablonovitch, Phys. Rev. B **66**, 153305 (2002).
[19] K. T. Shimizu, W. K. Woo, B. R. Fisher, H. J. Eisler, and M. G. Bawendi, Phys. Rev. Lett. **89**, 117401 (2002).
[20] Throughout the text we use the term irradiance to denote both the energy density flux of a standing wave and that of a running wave.
[21] A. Penzkofer and W. Leupacher, J. Lumin. **37**, 61 (1987).
[22] M. Fischer and J. Georges, Chem. Phys. Lett. **260**, 115 (1996).
[23] I. Z. Kozma, P. Krok, and E. Riedle, J. Opt. Soc. Am. B **22**, 1479 (2005).
[24] J. J. Burke, G. I. Stegeman, and T. Tamir, Phys. Rev. B **33**, 5186 (1986).
[25] E. D. Palik, *Handbook of Optical Constants of Solids* (Academic, New York, 1985).
[26] F. Mikes, Y. Yang, I. Teraoka, T. Ishigure, Y. Koike, and Y. Okamato, Macromolecules **38**, 4237 (2005).
[27] L. G. Nair, Prog. Quantum Electron. **7**, 153 (1982).
[28] P. Yeh, *Optical Waves in Layered Media* (Wiley, New York, 1988).
[29] E. Hecht, *Optics*, 4th ed. (Addison-Wesley, Reading, MA, 2002).
[30] C. Chen, P. Berini, D. Feng, S. Tanev, and V. Tzolov, Opt. Express **7**, 260 (2000).
[31] P. Berini, Phys. Rev. B **61**, 10484 (2000).

CHAPTER 3

Modelling SPP amplification in planar structures

3.1 Summary

The theoretical framework introduced in the previous chapter is applied to model the amplification of the single-interface SPP and LRSPP at a visible wavelength. The results obtained with this theory are taken as a baseline to perform a comparative study against two simplified theoretical models: one that neglects the lifetime position dependence and another that assumes a uniform gain medium. The discrepancies between the baseline and the simplified models are explained in terms of gain-mode overlap. The analysis considers a gain medium formed by optically-pumped R6G molecules in solution at moderate and high concentrations. It is shown that complete loss compensation of the LRSPP is possible at moderate molecular concentrations and pump irradiance, while for the single-interface SPP it is only possible when both the molecular concentration and the pump irradiance are high. The work describes in greater detail the theoretical approach presented earlier and points out important considerations that arise when dealing with high molecular concentrations.

3.2 Contribution

The results provided in this chapter were published in the electronic journal *Optics Express*. I implemented the numerical methods, generated and interpreted the results, and wrote the manuscript. Dr. Berini contributed to the interpretation of the results, and revised the manuscript.

3.3 Article

The published article follows verbatim.

Modeling surface plasmon-polariton gain in planar metallic structures

Israel De Leon[1] and Pierre Berini[1,2,3]

[1]*School of Information Technology and Engineering and* [2]*Department of Physics, University of Ottawa, 161 Louis Pasteur, Ottawa, Ontario, K1N 6N5, Canada.*
[3]*Spectalis Corp., P.O. Box 72029, Kanata North RPO, Ottawa, ON, K2K 2P4, Canada.*

Abstract: Amplification of the single-interface and long-range surface plasmon-polariton modes is studied in planar metallic structures incorporating gain media formed by Rhodamine 6G dye molecules in solution. We employ a theoretical model that accounts for the nonuniformity of the gain medium close to the metal surface due to position-dependent dipole lifetime and pump irradiance. The results of this model are used as a baseline for a comparative study against two simplified models: one neglects the position-dependent dipole lifetime while the other assumes a uniform gain medium. The discrepancies between the models are explained in terms of the mode overlap with the gain distribution near the metal. For the cases under analysis, the simplified models estimate the required pump irradiance with deviation factors that vary from 1.45 at the lossless conditions to 8 for gains near saturation. The relevance of describing properly the amount of gain interacting with the SPP mode and the role played by the dipole quantum efficiency are discussed.

OCIS codes: (240.6680) Surface plasmons; (250.4480) Optical amplifiers; (310.6805) Theory and design

References and links

1. H. Raether, *Surface Plasmons on Smooth and Rough Surfaces and on Gratings*, (Springer, Berlin, 1988).
2. W. L. Barnes, A. Dereux, and T. W. Ebbesen, "Surface plasmon subwavelength optics," Nature **424**, 824 (2003).
3. D. J. Bergman, and M. I. Stockman, "Surface plasmon amplification by stimulated emission of radiation: quantum generation of coherent surface plasmons in nanosystems," Phys. Rev. Lett. **90**, 027402 (2003).
4. M. P. Nezhad, K. Tetz, and Y. Fainman, "Gain assisted propagation of surface plasmon polaritons on planar metallic waveguides," Opt. Express **17**, 4072 (2004).
5. I. Avrutsky, "Surface plasmons at nanoscale relief gratings between a metal and a dielectric medium with optical gain," Phys. Rev. B **70**, 155416 (2004).
6. S. A. Maier, "Gain-assisted propagation of electromagnetic energy in subwavelength surface plasmon polariton gap waveguides," Opt. Comm. **258**, 295 (2006).
7. M. Z. Alam, J. Meier, J.S. Aitchison, and M. Mojahedi, "Gain assisted surface plasmon polariton in quantum well structures," Opt. Express **15**, 176 (2007).
8. T. Okamoto, F. H'Dhili, and S. Kawata, "Towards plasmonic band gap laser," App. Phys. Lett. **85**, 3968 (2004).
9. J. Seidel, S. Grafstrom, and L. Eng, "Stimulated emission of surface plasmons at the interface between a silver film and an optically pumped dye solution," Phys. Rev. Lett. **94**, 177401 (2005).
10. M. A. Noginov, V. A. Podolskiy, G. Zhu, M. Mayy, M. Bahoura, J. A. Adegoke, B. A. Ritzo, and K. Reynolds, "Compensation of loss in propagating surface plasmons polariton by gain in adjacent dielectric medium," Opt. Express **16**, 1385 (2008).
11. M. Ambati, S. H. Nam, E. Ulin-Avila, D. A. Genov, G. Bartal, and X. Zhang, "Observation of Stimulated Emission of Surface Plasmon Polaritons," Nano Lett. **8**, 3998 (2008)

#114693 - $15.00 USDReceived 23 Jul 2009; revised 8 Oct 2009; accepted 12 Oct 2009; published 21 Oct 2009

12. M. T. Hill, M. Marell, E. S. Leong, B. Smalbrugge, Y. Zhu, M. Sun, P. J. van Veldhoven, E. J. Geluk, F. Karouta, Y. Oei, R. Notzel, C. Ning, and M. K. Smit, "Lasing in metal-insulator-metal sub-wavelength plasmonic waveguides," Opt. Express. **17**, 11107 (2009).
13. J. Grandidier, G. Colas des Francs, S. Massenot, A. Bouhelier, L. Markey, J. C. Weeber, C. Finot, and A. Dereux, "Gain-Assisted Propagation in a Plasmonic Waveguide at Telecom Wavelength," Nano Lett. **9**, 2935 (2009).
14. G. W. Ford and W.H. Weber, "Electromagnetic interactions of molecules with metal surfaces," Phys. Rep. **113**, 195 (1984).
15. W. L. Barnes, "Fluorescence near interfaces: the role of photonic mode density," J. Mod. Opt. **45**, 661 (1998).
16. G. Winter, S. Wedge, and W. L. Barnes, "Can lasing at visible wavelength be achieved using the low-loss long-range surface plasmon-polariton mode?," New J. Phys. **8**, 125 (2006).
17. T. Okamoto, F. H'Dhili, and S. Kawata, "Plasmonic crystal for efficient energy transfer from fluorescent molecules to long-range surface plasmons," Opt. Express. **17**, 8294 (2009).
18. I. De Leon and P. Berini, "Theory of surface plasmon-polariton amplification in planar structures incorporating dipolar gain media," Phys. Rev. B **78**, 161401(R) (2008).
19. J. J. Burke, G. I. Stegeman, and T. Tamir,"Surface-polariton-like waves guided by thin, lossy metal films," Phys. Rev. B **33**, 5186 (1986).
20. E. D. Palik, *Handbook of Optical Constants of Solids*, (Academic Press, New York, 1985) .
21. F. Mikes, Y. Yang, I. Teraoka, T. Ishigure, Y. Koike, and Y. Okamoto, "Synthesis and Characterization of an Amorphous Perfluoropolymer Poly(perfluoro-2-methylene-4-methyl-13-dioxolane)," Macromolecules **38**, 4237 (2005).
22. I. Z. Kozma, P. Krok, and E. Riedle, "Direct measurement of the group-velocity mismatch and derivation of the refractive-index dispersion for a variety of solvents in the ultraviolet," J. Opt. Soc. Am. B **22**, 1479 (2005).
23. A. Penzkofer and W. Leupacher, "Fluorescence behaviour of highly concentrated rhodamine 6G solutions," J. Lumin. **37**, 61 (1978).
24. W. Falkenstein, A. Penzkofer, and W. Kaiser, "Amplified spontaneous emission in rhodamine dyes: Generation of picosecond light pulses and determination of excited state absorption and relaxation,"Opt. Commun. **27**, 151 (1978).
25. E. Sahar and D. Treves, "Excited singlet-state absorption in dyes and their effect on dye lasers," IEEE J. Quantum Electron. **QE-13**, 962 (1977).
26. H. J. Eichler, U. Klein, and D. Langhans, "Measurement of orientational relaxation times of rhodamine 6G with a streak camera," Chem. Phys. Lett. **67**, 21 (1979).
27. L. G. Nair, "Dye Lasers," Prog. Quantum Electron. **7**, 153 (1982).
28. P. Yeh, *Optical waves in layered media* (Wiley, New York, 1988).
29. S. Astilean and W. L. Barnes, "Quantum efficiency and the photonic control of molecular fluorescence in the solid state," App. Phys. B **75**, 591 (2002).
30. C. Chen, P. Berini, D. Feng, S. Tanev, and V. Tzolov, "Efficient and accurate numerical analysis of multilayer planar optical waveguides in lossy anisotropic media," Opt. Express **7**, 260 (2000).
31. P. Berini, "Bulk and surface sensitivities of surface plasmon waveguides," New J. Phys. **10**, 105010 (2008).
32. Y. Jee, M. F. Becker, and R. M. Walser, "Laser-induced damage on single-crystal metal surfaces," J. Opt. Soc. Am. B **5**, 648 (1988).
33. W. Svendsen, O. Ellegaard, and J. Schou , "Laser ablation deposition measurements from silver and nickel," Appl. Phys. A **63** 247 (1996).
34. A. V. Fedenev, E. I. Lipatov, V. F. Tarasenko, V. M. Orlovskii, M. A. Shulepov, N. N. Koval, and I. M. Goncharenko, "Disturbance of adhesion upon ablation of thin films by laser pulses," Quantum Electron. **34**, 375 (2004).

1. Introduction

Surface plasmon-polaritons (SPPs) are electromagnetic waves coupled to surface plasma oscillations that propagate along the interface between a dielectric and a metal with a negative real part of permittivity [1]. A variety of plasmonic structures have been analyzed exhibiting interesting properties [2], but the intrinsic propagation loss of SPP modes introduces limitations for several potential applications. This problem has created a strong interest in understanding the physics of SPP amplification [3]–[7] as well as exploring experimentally its feasibility [8]–[13]. The rapid progress in active plasmonics has provided exciting results; for instance, stimulated amplification of SPP modes has been observed [9, 10, 11], and very recently, lasing in subwavelength plasmonic waveguides was claimed [12].

Optical dipoles (dye molecules, rare-earth ions, atoms, or semiconductor quantum dots) are of particular interest because they can be integrated with dielectric hosts and conveniently used

#114693 - $15.00 USDReceived 23 Jul 2009; revised 8 Oct 2009; accepted 12 Oct 2009; published 21 Oct 2009

in the construction of active SPP waveguides. Indeed, much research has been done on the complex radiative behaviour of dipoles in close proximity to metallic surfaces [14, 15]. However, few investigations have addressed its consequences on SPP amplification [16, 17, 18]. Close to the metallic surface the pump radiation is generally not uniform and the increased density of modes and coupling to electrons in the metal quench the dipole's lifetime. These two factors play an important role in shaping the gain distribution interacting with a mode during the amplification process. It is the purpose of this paper to address these phenomena.

This paper builds on our previous theoretical work that describes SPP amplification in planar structures accounting for the nonuniformity of optically pumped dipolar gain media [18]. Here, we describe the model in greater detail and employ it to study the amplification of the long-range SPP (LRSPP) and the single-interface SPP modes in two planar structures incorporating gain media formed by Rhodamine 6G (R6G) dye molecules in solution. The analysis considers two dye concentrations taking into account the concentration-dependent quantum efficiency of R6G. We present a comparative study between the proposed model and two simplified models that do not account entirely for the nonuniform nature of the gain near the metal surface. We discuss the relevance of including such effects by analyzing the gain-mode overlap described by the different gain models and express the importance of the dipole quantum efficiency in determining the amount of gain interacting with the SPP mode.

2. Geometries Investigated

The analysis consider the structures shown in Figs. 1(a) and (b). Structure 1 consists of a 20 nm-thick silver film extending infinitely over the $(x,z)-$plane. The bottom cladding is formed by 2 μm of CYTOP, a lossless dielectric, which in turn sits on a semi-infinite silicon substrate; the top surface is covered by R6G dye molecules in a mixture of ethanol and methanol. A semi-infinite CYTOP superstrate lies on top of the dye solution, holding it to within a 1-μm-thick layer. For structure 2 the silver region extends infinitely below the dye region.

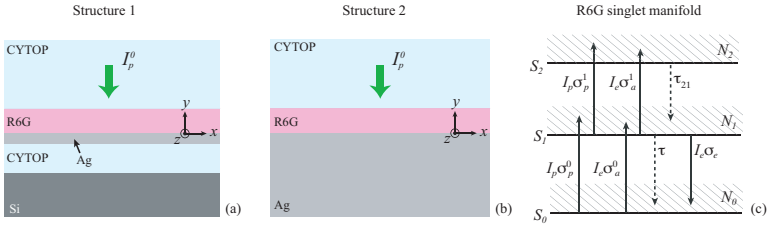

Fig. 1. (a) Thin-film active structure (Structure 1). (b) Semi-infinite metal active structure (Structure 2). (c) Multi-level energy model used for R6G molecules.

In both structures, dye molecules are excited at broadside by a monochromatic pump signal of wavelength $\lambda_p = 532$ nm (frequency-doubled Nd:YAG), which is near the peak absorption of R6G. SPP mode amplification is studied at the peak emission wavelength of the dye, $\lambda_e = 560$ nm. We assume that the real permittivity of the dye solution is matched to CYTOP at λ_e, making structure 1 symmetric. This can be achieved using a mixture of approximately 57% methanol and 43% ethanol as the dye solvent [22]. The analysis considers two dye concentrations, $C_a = 5$ mM and $C_b = 40$ mM, which correspond to dye volume densities of 3.01×10^{18} cm^{-3} and 24.08×10^{18} cm^{-3}, respectively. The concentration-dependent properties of R6G are approximated either in pure methanol or pure ethanol from information available in the literature [23]-[26]. Tables 1 and 2 in the appendix summarize respectively the material relative permittivities and photophysical parameters of R6G at the two wavelengths of interest.

#114693 - $15.00 USDReceived 23 Jul 2009; revised 8 Oct 2009; accepted 12 Oct 2009; published 21 Oct 2009

Structure 1 supports LRSPP and short-range SPP modes [19]. However, the gain analysis of the latter will be omitted because of its large propagation losses. Structure 2 supports the single-interface SPP mode. The proposed structures and pump arrangement are physically realizable and could serve directly to validate the results reported herein.

3. Gain model

The energy levels and transition rates of R6G are depicted schematically in Fig. 1(c). It shows the three most relevant electronic states and associated vibrational and rotational overlapping energy levels (represented by the shaded areas) of the singlet manifold. The parameters in the figure are as follows: S_i denote the ground $(i=0)$, first excited $(i=1)$, and second excited $(i=2)$ energy states, and N_i indicates their respective molecular populations; σ_p^0 and σ_a^0 (σ_p^1 and σ_a^1) are the absorption cross-sections of state S_0 (S_1) at λ_p and λ_e, respectively; τ_{21} is the lifetime (decay time) from state S_2 to S_1, which is approximately the lifetime of state S_2 [24]; σ_e and τ are, respectively, the emission cross-section at λ_e and lifetime of the S_1 state; I_p is the pump irradiance at λ_p and I_e is the stimulated emission irradiance at λ_e. We neglect transitions to the triplet manifold assuming that the pump signal duration is short compared to the reciprocal inter-system crossing rate of $2.8\mu s$ [24]. Yet, we also assume that the pump signal duration is long compared to τ, such that steady state conditions are reached. These assumptions are reasonable for R6G molecules pumped by typical ~ 10 ns-pulse frequency-doubled Nd:YAG lasers.

The small-signal gain coefficient of the dye at λ_e is given by [27]

$$g = N_1\sigma_e^* - N_0\sigma_a^0, \tag{1}$$

where $\sigma_e^* = \sigma_e - \sigma_a^1$ is the effective emission cross-section of the S_1 state. To obtain N_1 at any point in the dye region one must solve the rate equations locally, accounting for the position dependent lifetime and pump radiation. Thus, we replace the constants τ and I_p with their respective position dependent expressions, which will be obtained in the following subsections.

Solving the rate equations locally under steady state conditions and using the small signal approximation, one obtains

$$N_1(y) = \frac{NI_p(y)\tau(y)\sigma_p^0}{I_p(y)\tau(y)\sigma_p^0 + \hbar\omega_p} \tag{2a}$$

$$-\frac{dI_p(y)}{dy} = I_p(y)\left[N\sigma_p^0 - N_1(y)\sigma_p^0 + N_1(y)\sigma_p^1\right], \tag{2b}$$

where N is the total molecular population, ω_p is the pump angular frequency, and $\hbar$ is the reduced Plank constant. In writing Eq. (2) we have taken $N_2 = 0$ assuming that τ_{21}^{-1} is much faster than the rate at which S_2 is populated, $I_p\sigma_p^1 \ll \hbar\omega_p/\tau_{21}$. This holds for $I_p \ll 6\times10^9$ W/cm^2, which also holds throughout the paper. Substituting Eq. (2a) into Eq. (1) one obtains the local small-signal gain coefficient

$$g(y) = N\frac{I_p(y)\tau(y)\sigma_p^0\sigma_e^* - \sigma_a^0\hbar\omega_p}{I_p(y)\tau(y)\sigma_p^0 + \hbar\omega_p}. \tag{3}$$

The present analysis assumes an infinitesimally small amplifier length, in which ASE does not play a role. In a real device, the effect of ASE could be significant when the amplifier's length and dye concentration are large enough. ASE renders g inhomogeneous along the propagation axis, peaking at the center of the amplifier and tailing off towards the facets. Thus, one should expect the present model to be accurate for modeling short-length SPP amplifiers.

#114693 - $15.00 USDReceived 23 Jul 2009; revised 8 Oct 2009; accepted 12 Oct 2009; published 21 Oct 2009

3.1. *Position dependent pump irradiance*

We model the pump signal as a linearly polarized plane wave of wavelength λ_p and irradiance I_p^0 that illuminates the structure from the top with propagation direction normal to the metal plane. Its absorption trough the dye is described by Eq. (2b) and satisfies the following approximations:

$$-\frac{dI_p(y)}{dy} \approx \begin{cases} I_p(y)N\sigma_p^0, & \text{if } I_p(y) \ll \hbar\omega_p/\sigma_p^0\tau(y) \\ I_p(y)N\sigma_p^1, & \text{if } I_p(y) \gg \hbar\omega_p/\sigma_p^1\tau(y), \end{cases} \tag{4}$$

where we have used the fact that $\sigma_p^1 < \sigma_p^0$ for R6G, as it is typically the case for most dyes. The behavior of $I_p(y)$ is non-linear and monotonic between these limiting cases. A rigorous non-linear treatment is out of the scope of this paper; instead we henceforth employ the *linear approximation* described by the top form in Eq. (4), which is also valid for an optically thin dye region regardless of the value of I_p. Under this approximation, the relative permittivity of the dye at λ_p can be expressed as

$$\varepsilon_{r,p} = \varepsilon'_{r,p} - i\frac{\lambda_e}{2\pi}N\sigma_p(\varepsilon'_{r,p})^{1/2}, \tag{5}$$

where $\varepsilon'_{r,p}$ is the relative permittivity of the dye solvent. Using this expression we compute the pump electric-field distribution throughout the structure, $E_p(y)$, using a transfer matrix formalism [28]. Then, the irradiance distribution is obtained as

$$I_p(y) = \frac{\text{Re}\,\eta(y)}{2|\eta(y)|^2}|E_p(y)|^2, \tag{6}$$

where $\eta(y)$ is the characteristic impedance of the medium at the location y.

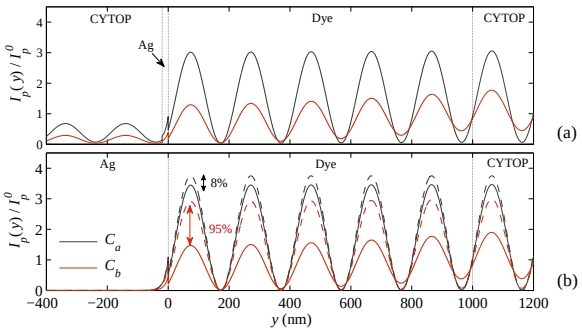

Fig. 2. Normalized pump irradiance distribution (solid lines) across (a) structure 1 and (b) structure 2. The dashed lines are computed for I_p^0 satisfying the bottom form in Eq. (4). The irradiance in the metal region in both structures is magnified 20 times.

The normalized pump irradiance distribution, $I_p(y)/I_p^0$, in Structure 1 and 2 is shown in Figs. 2(a) and (b), respectively. Each figure show results for the two dye concentrations. The pump distribution above the metal is similar in both structures, following a standing-wave pattern due to field reflections throughout the structure. The peak values in both structures reach similar values because the lower-cladding thickness in structure 1 was chosen to reduce resonant coupling into the slab mode and increase the peak irradiance in the dye region.

The dashed curves in Fig. 2(b) illustrate the case where the bottom form in Eq. (4) is satisfied. Thus, the difference between dashed and solid curves represents the worst case error due to

#114693 - $15.00 USDReceived 23 Jul 2009; revised 8 Oct 2009; accepted 12 Oct 2009; published 21 Oct 2009

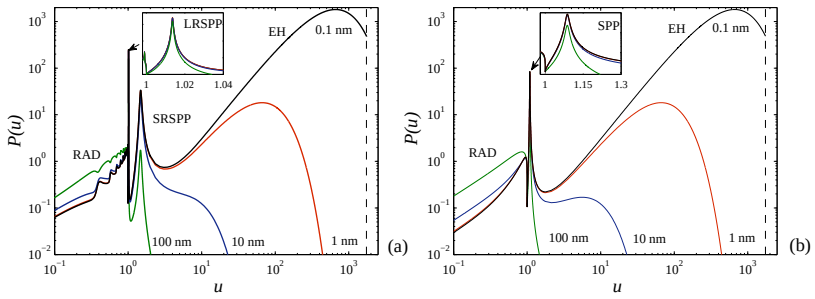

Fig. 3. Normalized power dissipation density of an isotropically oriented dipole located at the labeled metal-dipole separations for (a) Structure 1 and (b) Structure 2.

the linear approximation. For concentration C_a the dye layer is optically thin and the error is only 8%. This is not the case for concentration C_b, where the error reaches 95%. Similar errors apply to Structure 1. In general, the absorption is overestimated when the adopted linear approximation is not valid. In such a case, $N_1(y)$ in Eq. (2b) and consequently $g(y)$ in Eq. (3) take lower-bounded values set by the low-I_p linear absorption.

3.2. Position dependent dipole lifetime

The position-dependent lifetime, $\tau(y)$, in Eq. (3) is obtained following a classical treatment that considers molecules as dipoles being driven by the reflection of its own radiation at the metal surface [14, 15]. Within this framework, the normalized decay rate of a dipole located at a distance y from the metal surface and with dipole-moment oriented along μ can be written as

$$\hat{\gamma}_\mu(y) = \hat{\gamma}_{nr} + \phi \int_0^\infty P_\mu(u,y)\, du, \tag{7}$$

where $\gamma_{nr} = 1-\phi$ is the normalized non-radiative decay rate and ϕ is the dipole's quantum efficiency; $u = k_\parallel/k$ is the component of the dipole's field wave vector parallel to the metal plane ($k_\parallel$) normalized to the magnitude of the dipole's far-field wave vector (k); and P_μ is the dipole's power dissipation density normalized to the power dissipation far from the metal. The components of P_μ with dipole-moment orientation perpendicular ($\perp$) and parallel ($\parallel$) to the metal plane are

$$\begin{aligned} P_\perp(u,y) &= \mathrm{Re}\,\frac{3}{2}\frac{u^3}{\sqrt{1-u^2}}\left\{1 + r_\mathrm{P}\exp\left(i2k_\parallel y\right)\right\} \\ P_\parallel(u,y) &= \mathrm{Re}\,\frac{3}{4}\frac{u}{\sqrt{1-u^2}}\left\{\left(1 + r_\mathrm{S}\exp\left(i2k_\parallel y\right)\right) + \left(1-u^2\right)\left(1 - r_\mathrm{P}\exp\left(i2k_\parallel y\right)\right)\right\}, \end{aligned} \tag{8}$$

where $r_{\mathrm{S,P}}$ are the Fresnel reflection coefficients of the multilayer structure for waves polarized perpendicular (S) and parallel (P) to the metal plane.

For concentration C_a, the rotational reorientation time of R6G in a similar solvent, τ_{or}, is much smaller than the lifetime, τ (see Table 2), leading to an isotropic excited dipole population. On the contrary, τ_{or} is comparable to τ for concentration C_b; nonetheless Förster-type energy transfer between dipoles renders the excited dipole population isotropic [23]. Hence, for our analysis we consider the isotropic normalized power dissipation density obtained by averaging over all possible dipole-moment orientations

$$P(u,y) = \frac{2}{3}P_\parallel(u,y) + \frac{1}{3}P_\perp(u,y). \tag{9}$$

#114693 - $15.00 USDReceived 23 Jul 2009; revised 8 Oct 2009; accepted 12 Oct 2009; published 21 Oct 2009

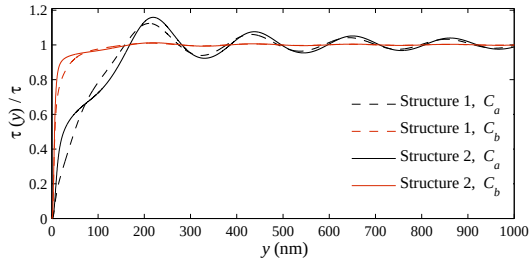

Fig. 4. Normalized lifetime distribution of an isotropically oriented dipole in structure 1 (dashed lines) and structure 2 (solid lines) for both concentrations, C_a (black) and C_b (red).

The results of Eq. (9) at λ_e for several metal-dipole separations are shown in Fig. 3(a) and (b) for structures 1 and 2, respectively. The features present over different intervals of u are associated with the particular decay channel labeled on the figure. These decay channels include coupling to radiative modes (RAD), where the dipole emits a photon; coupling to SRSPP, LRSPP, and single-interface SPP, where the dipole emits a SPP; and coupling to electron-hole (EH) pairs in the metal, where the dipole's energy is transferred directly to the metal in a dipole-dipole interaction. The latter, characterized by the broad peaks present at large u values and short dipole-metal separations, is strongly suppressed by electron screening when u reaches the upper limit of the EH excitation continuum [14]. For silver at λ_e this limit is $u = 2.2k_F/k$ (k_F being the Fermi wave vector). We account approximately for this effect by limiting the u-domain to values below $2.2k_F/k$ as indicated by the vertical dashed lines in Fig. 3.

The lifetime of an isotropically oriented dipole as a function of its distance from the metal surface is given by

$$\tau(y) = \hat{\gamma}(y)^{-1}\tau, \tag{10}$$

where $\hat{\gamma}(y)$ is the normalized decay rate of an isotropically oriented dipole obtained from Eq. (7) using Eq. (9) as the integrand. The results of Eq. (10) normalized to τ are shown in Fig. 4 for both structures and for both dye concentrations. For concentration C_a, $\phi = 0.9$ and Eq. (7) is dominated by the second term, which comprises the different decay channels discussed above. In this case, dipole relaxation through the multiple decay channels causes the characteristic strong quenching near the metal surface and the oscillatory behaviour in $\tau(y)$. For concentration C_b, the quantum efficiency drops to $\phi = 0.08$ due to Förster-type energy transfer between dipoles [23] and Eq. (7) is dominated by the non-radiative term. Thus, for concentration C_b the lifetime is practically position independent, except for very short dipole-metal separations where the EH, SRSPP, and SPP decay channels still have significant effects.

The above mentioned effects have been confirmed experimentally for two dyes with different intrinsic quantum efficiency [29]. Yet, there are no experimental reports addressing the case where the quantum efficiency is altered due to a Förster type energy transfer between dipoles.

4. Numerical analysis

The gain medium is characterized by its inhomogeneous complex permittivity at λ_e,

$$\varepsilon_{r,e}(y) = \varepsilon'_{r,e} + i\frac{\lambda_e}{2\pi}g(y)(\varepsilon'_{r,e})^{1/2}, \tag{11}$$

where $\varepsilon'_{r,e}$ is the relative permittivity of the dye solvent. The SPP modes of the structures are obtained using the transfer matrix method [30]. In this calculation, $\varepsilon_{r,e}(y)$ is divided into

#114693 - $15.00 USDReceived 23 Jul 2009; revised 8 Oct 2009; accepted 12 Oct 2009; published 21 Oct 2009

15,000 layers of equal thickness, keeping its value constant within each layer. We take the SPP mode propagation along the z-axis with mode fields having a complex phase of the form $\exp[z(-i\beta+\alpha)]$. Thus, a positive (negative) value of α indicates amplification (attenuation) as the mode propagates in the positive z-direction. The *mode power gain coefficient* is given by

$$G = 2\alpha. \tag{12}$$

In what follows we compare the results obtained using three different models for $g(y)$. Our baseline model is described in Section 3 and will be referred to as model A; model B accounts for $I_p(y)$ but assumes a uniform lifetime of the from $\tau(y) = \tau$; and model C assumes a uniform pump distribution of the form $I_p(y) = I_p^0$ and the same uniform lifetime as model B. In all our calculations we have used the material relative permittivities and concentration-dependent photophysical parameters of R6G listed in the appendix.

4.1. Gain-mode overlap

The mode-gain overlap is depicted in Figs. 5(a,b) and (c,d) for the LRSPP mode of structure 1 and single-interface SPP mode of structure 2, respectively. They show the mode's normalized $|E_y|^2$ distribution and the dye's gain coefficient distributions obtained with models A, B, and C (labeled g_A, g_B, and g_C) for both dye concentrations and two pump irradiances: $I_{p,l} = 300$ kW/cm^2 and $I_{p,h} = 10$ MW/cm^2 for concentration C_a, and $I_{p,l} = 3$ MW/cm^2 and $I_{p,h} = 30$ MW/cm^2 for concentration C_b. The magenta dashed lines indicate the gain saturation limit, $g_s = N\sigma_{em}^*$. The mode distributions obtained with the different gain models and pump irradiances on each figure are very similar and lay on top of each other. The embedded movies show the evolution of $g(y)$ and $|E_y|^2$ over the range $0 < I_p^0 < 30$ MW/cm^2.

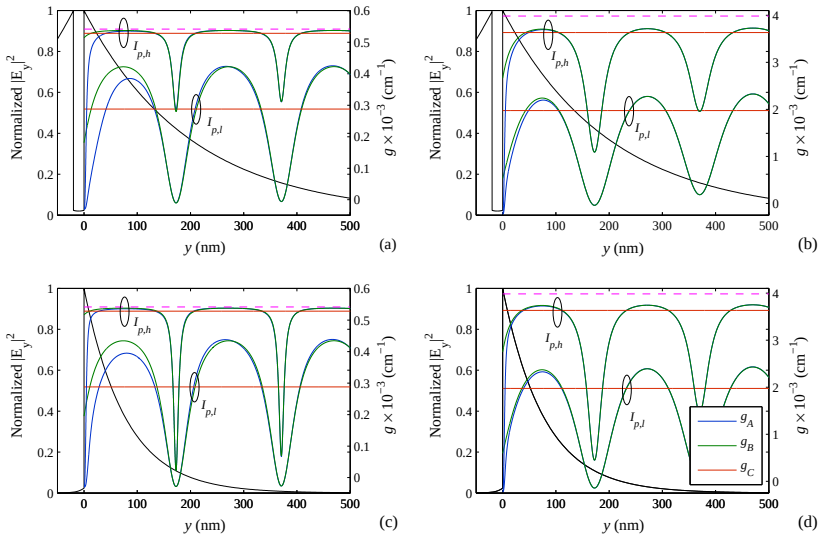

Fig. 5. Dye's gain coefficient distribution, $g(y)$, and the normalized $|E_y|^2$ distribution for the LRSPP mode using concentration (a) C_a (Media 1) and (b) C_b (Media 2), and for the single-interface SPP mode using concentrations (c) C_a (Media 3) and (d) C_b (Media 4).

In calculating $g(y)$ we have included the effects of gain reduction due to the formation of weakly-fluorescent dimers at high concentrations. The dimer molar fraction, d, is obtained

#114693 - $15.00 USDReceived 23 Jul 2009; revised 8 Oct 2009; accepted 12 Oct 2009; published 21 Oct 2009

from [23] as 0.08 and 0 for concentration C_b and C_a, respectively. The gain coefficients are obtained from Eq. (3) by letting $N \to N(1-d)$. The large $g(y)$ values obtained have not been demonstrated experimentally with R6G; however, they should be achievable in principle since the two dye concentrations are well bellow the solubility limit (~ 0.6 M in methanol) of R6G.

In general, the values of g_A, g_B, and g_C obtained for Structure 1 are similar to those obtained for structure 2. This is expected as we note from Figs. 2 and 4 that $I_p(y)$ and $\tau(y)$ are similar for both structures. For concentration C_a and pump irradiance $I_{p,l}$ the gain coefficients are far from the saturation limit; g_A and g_B follow closely the pump profile given by Eq. (6) whereas g_C is well below their peaks because model *C* does not account for pump reflection. However, g_A is significantly suppressed for $y < 150$ nm, which reduces the gain-mode overlap. This is consequence of the lifetime quenching discussed in Section 3.2. On the other hand, for $I_{p,h}$, the three gain models approach the saturation limit. The high pump irradiance overcomes to some extent the lifetime quenching reducing the discrepancy between g_A and g_B to within a smaller region, $y < 80$ nm. The results for concentration C_b show two main differences. First, saturation effects are not as evident because of the large dye concentration; and second, the low quantum efficiency reduces the lifetime quenching near the metal surface causing g_A and g_B to differ within a reduced range, $y < 90$ nm, that depends weakly on the pump irradiance.

The gain-mode overlap can be very different in both structures because of the different mode penetration depths into the gain medium. For the LRSPP mode, $|E_y|^2$ drops a factor of e^{-2} at $y = 400$ nm whereas for the single-interface SPP mode it occurs at $y = 155$ nm. Thus, in the latter case the gain nonuniformities close to the metal surface have a stronger impact in the gain-mode overlap.

4.2. Mode power gain versus pump irradiance

In this subsection we study the properties of G as a function of I_p^0 using the three gain models previously described. Figs. 6(a,b) and (c,d) show $G(I_p^0)$ computed with the three models (labeled G_A, G_B, and G_C) for the LRSPP and single-interface SPP modes, respectively. The results are computed for the range $0 < I_p^0 < 30$ MW/cm^2. The dashed magenta lines indicate the saturation limit, $G_s = G(I_p^0 \to \infty)$, and the quantity $D = G_s - G(0)$ given on each figure represents the amplification range. Observe that for cases with the same dye concentration, D is approximately 2.45 times larger for the single-interface SPP mode. The factor of 2 is expected because only half of the LRSPP mode interacts with the gain medium. The remainder is attributed to the larger bulk sensitivity of the single-interface SPP mode [31].

The lossless condition calculated with model *A* is indicated by the black dashed lines on the figures. For the LRSPP mode, this condition is achieved with reasonably low pump irradiances; ie., $I_p^0 = 175$ kW/cm^2 and $I_p^0 = 430$ kW/cm^2 for concentrations C_a and C_b, respectively. The value for concentration C_b is larger because of the larger dye absorption at λ_e, which attenuates the amplified light, and because of the larger dye absorption at λ_p, which reduces the pump irradiance in the dye region as shown in Fig 2. On the other hand, the lossless condition for single-interface SPP mode can be achieved only with concentration C_b when $I_p^0 = 3.455$ MW/cm^2. Note that this value could be overestimated by up to a factor of two because it does not satisfy the linear absorption approximation as stated by the top form of Eq. (4), which was adopted in the calculations. On the contrary, the I_p^0 values required for lossless propagation of the LRSPP mode do satisfy this approximation.

The pump irradiances required for lossless propagation in both structures are attainable using commercial lasers; however, the maximum I_p^0 value that can be sustained is determined by the metal damage threshold. Laser-induced metal damage develops over a number of phases that aggravate with increasing irradiance [32]. The first signs of damage appear in the form of microscopic defects and deformations on the surface; as the irradiance increases the surface melts

#114693 - $15.00 USDReceived 23 Jul 2009; revised 8 Oct 2009; accepted 12 Oct 2009; published 21 Oct 2009

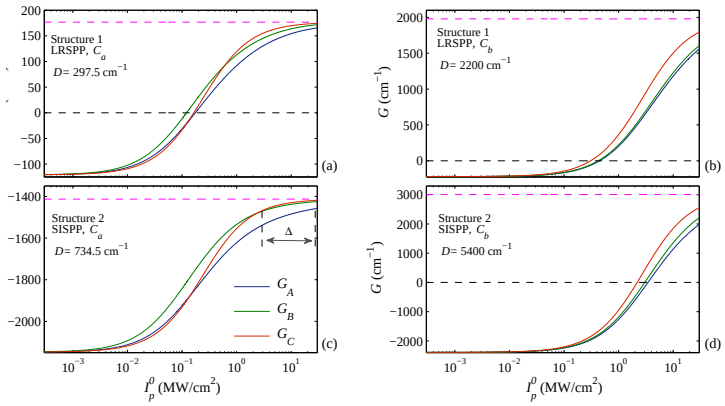

Fig. 6. Comparative analysis of $G(I_p^0)$. The curves for the three different models are plotted for the LRSPP mode using concentration (a) C_a and (b) C_b, and for the single-interface SPP mode using concentrations (c) C_a and (d) C_b.

and eventually evaporates leading to ablation. The damage threshold of a plasmonic structure must be defined in terms of the metal quality needed to support a particular SPP mode and could be lower than the ablation threshold, which has been estimated as ~ 160 MW/cm^2 for bulk silver exposed during 20 minutes to pulsed (0.8 J/cm^2, 5 ns duration, 0.16 Hz repetition rate) 532 nm radiation [33]. For thin films, factors such as loss of adhesion due to thermal stress [34] and lower heat dissipation capacity could further reduce this damage threshold.

From the results in Fig. 6(a-d) we note that model A generally requires higher I_p^0 values to achieve the same G values estimated by the other two models because it considers factors that reduce the dye's gain over the mode region. To quantify these deviations we define the factor

$$f_x = \frac{I_{p,A}}{I_{p,x}}, \tag{13}$$

where x stands for either model B or C and $I_{p,A}$ ($I_{p,x}$) is the pump irradiance required to obtain a particular value of G using model A (model x). f is plotted for both concentrations in Figs. 7(a,b) and (c,d) for the LRSPP and single-interface SPP modes, respectively.

Consider first the factors associated with model B, which result from neglecting the lifetime position dependence. From the f_B curves for concentration C_a and structure 1 (structure 2) we note that model A estimates pump irradiances that are factors of 1.3 to 2.5 (1.5 to 6.8) larger than those of model B. The larger values obtained for structure 2 occur because the mode-gain overlap of the single-interface SPP mode is more sensitive to the changes in $g(y)$ that result from neglecting lifetime quenching included in $\tau(y)$. Yet, for concentration C_b and for both structures, f_B is close to unity for most values of G. This accentuates that model B can be a good approximation to model A when the dipole quantum efficiency is low because in this case $\tau(y) \approx \tau$.

Consider now the factors associated with model C, which result from neglecting both the lifetime and pump position dependence. Interestingly, for concentration C_a, there exist a region over which $f_C \approx 1$ (also shown in Figs. 6(a) and (c) as similar G_A and G_C curves in the region $I_p^0 < 200$ kW/cm^2). This is merely coincidental and cannot be generalized for an arbitrary

#114693 - $15.00 USDReceived 23 Jul 2009; revised 8 Oct 2009; accepted 12 Oct 2009; published 21 Oct 2009

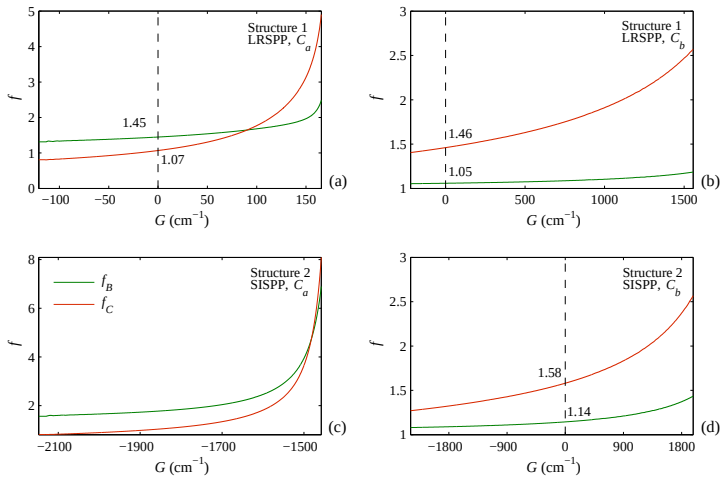

Fig. 7. Pump irradiance increment factors, f_B and f_C, for the LRSPP mode using concentration (a) C_a and (b) C_b, and for the single-interface SPP mode using concentrations (c) C_a and (d) C_b. The vertical dashed lines represent the lossless condition, $G_A = 0$

structure. Indeed, this is supported by the results for concentration C_b and structure 1 (structure 2), where f_C ranges from 1.45 to 2.55 (1.27 to 2.5). In general, G_C reaches saturation with lower I_p^0 values than G_A because model C assumes a perfect gain-mode overlap and neglects the pump absorption through the dye. This results in large f_C values at large G values. A clear example is given in Fig. 6(c), where the I_p^0 deviation (Δ) covers almost one decade; this yields $f_C = 8$ as shown in Fig. 7(c).

The values of f_B and f_C at the lossless propagation condition are indicated on Figs. 7(a), (b), and (d). Some of them represent deviations of $\sim 50\%$ in the pump irradiance estimated by model A. These values are rather significant, especially if the pump irradiance is close to the damage threshold of the metal. Also, from the discussion above, we note that model A provides large corrections to the other two models around the gain saturation region. Thus, the use of model A would be particularly important for weaker gain media, where the lossless condition could be achieved close to gain saturation.

5. Summary

In summary, we study the amplification of the LRSPP and single-interface SPP modes in planar metallic structures incorporating gain media formed by Rhodamine 6G dye molecules in solution. We employ a theoretical model that accounts for the nonuniform gain distribution in close proximity to the metal and its overlap with the SPP mode. The analysis considers two dye concentrations, 5 mM and 40 mM, accounting for the concentration-dependent quantum efficiency of R6G. Within the limitations of the model, the results suggest that lossless propagation is possible in the visible for both SPP modes using the proposed structures and pump arrangement. For the LRSPP mode, the lossless propagation condition was obtained using reasonable pump irradiances; ie., 175 kW/cm^2 and 430 kW/cm^2 for 5 mM and 40 mM dye concentration, respectively. For the single-interface SPP mode, lossless propagation was obtained only with the 40 mM dye concentration using an intense pump irradiance of 3.45 MW/cm^2.

#114693 - $15.00 USDReceived 23 Jul 2009; revised 8 Oct 2009; accepted 12 Oct 2009; published 21 Oct 2009

The proposed model is taken as baseline to perform a comparative study against two simplified models: one neglects the lifetime position dependence, while the other assumes a uniform gain medium. The discrepancies between the baseline and the simplified models are explained in terms of gain-mode overlap. For the cases under analysis, the simplified models estimate the required pump irradiance with deviation factors that vary from 1.45 at the lossless conditions to 8 for gains near saturation. The relevance of describing properly the amount of gain interacting with the SPP mode and the role played by the dipole quantum efficiency are discussed. In particular, the results show that the discrepancies due to ignoring the lifetime position dependence are not considerable when the dye's quantum efficiency is low.

6. Appendix: Relative permittivities and R6G parameters

Table 1. Relative permittivities (ε_r) at $\lambda_p = 532$ nm and $\lambda_e = 560$ nm.

Material	$\varepsilon_r(\lambda_p)$	$\varepsilon_r(\lambda_e)$	Reference
Silver	$-10.18 - i\,0.8311$	$-11.68 - i\,0.8283$	[20]
Silicon	$17.22 - i\,0.3646$	$16.42 - i\,0.2936$	[20]
CYTOP	1.8053	1.8039	[21]
Dye solvent	1.8068	1.8039	[22]

Table 2. Photophysical parameters of Rhodamine 6G. The last four parameters (below horizontal line) are assumed to be concentration-independent. * Values for monomers.

Parameter	Concentration	Value	Reference
ϕ	C_a	0.9	[23]
ϕ	C_b	0.08	[23]
τ	C_a	3.9 ns	[23]
τ	C_b	312 ps	[23]
σ_e	C_a, C_b	3×10^{-16} cm^2 *	[23]
σ_p^0	C_a, C_b	4×10^{-16} cm^2 *	[23]
σ_a^0	C_a, C_b	1×10^{-17} cm^2 *	[23]
τ_{12}	–	0.5 ps	[24]
σ_p^1	–	1.2×10^{-16} cm^2	[25]
σ_a^1	–	1.2×10^{-16} cm^2	[25]
τ_{or}	–	~ 100 ps	[26]

#114693 - $15.00 USDReceived 23 Jul 2009; revised 8 Oct 2009; accepted 12 Oct 2009; published 21 Oct 2009

3.4 Errata

- The first sentence below Eq.(3) should read:
  The present analysis assumes an infinitesimally small amplifier length, in which amplified spontaneous emission (ASE) does not play a role.

- The last paragraph in section 3.2 should read:
  The above-mentioned effects have been confirmed experimentally for two dyes with different intrinsic quantum efficiencies [29]. However, there are no experimental reports confirming whether this holds for dipoles whose quantum efficiency is affected by Förster type energy transfer between dipoles.

CHAPTER 4

Amplification of long-range SPPs by a dipolar gain medium

4.1 Summary

This chapter provides a direct measurement of gain (beyond complete compensation of propagation losses) in propagating plasmons using the LRSPP supported by a symmetric metal stripe waveguide that incorporates optically pumped dye molecules in solution as the gain medium. The gain is measured directly as the ratio of the output power to the input power. In addition, the mode power gain of the amplified mode is obtained from measurements of gain as a function of the amplifier length. The measurements indicate that the LRSPP propagates with a mode power gain of 8.55 dB mm^{-1}. Furthermore, a reduction of 6.3 dB in the spontaneous emission intensity in the vicinity of the waveguide relative to that in the bulk gain medium is measured. A qualitative explanation of this phenomenon is given in terms of the spontaneous emission probabilities into the different energy decay channels supported by the metallic structure as well as energy absorption of each of these channels. The supplementary information section discusses the waveguide's passive operation, absorption and emission properties of the dye solution, and gold surface degradation due to pump radiation.

4.2 Contribution

The results provided in this chapter were published as an article in the journal *Nature Photonics*. I designed and built the experimental setup; I developed the active structure used for the experimentation based on a passive waveguide provided by Dr. Berini; I implemented the numerical methods used for the theoretical analysis; I generated and interpreted the theoretical and experimental results, and wrote the manuscript. Dr. Berini contributed to the design of the experiments and experimental setup, the interpretation of the results, and revised the manuscript.

4.3 Article

The published article follows verbatim.

nature photonics

ARTICLES

PUBLISHED ONLINE: 28 MARCH 2010 | DOI: 10.1038/NPHOTON.2010.37

Amplification of long-range surface plasmons by a dipolar gain medium

Israel De Leon[1] and Pierre Berini[1,2,3]*

Surface plasmon–polaritons, collective electron oscillations coupled to light waves at the surface of a metal, show unique properties that are valuable in a broad range of scientific fields. However, the intrinsic propagation loss of these waves poses a fundamental problem to many potential applications. To overcome this drawback, researchers have explored the possibility of loss compensation by means of surface plasmon–polariton amplification. Here we provide the first direct measurement of gain in propagating plasmons using the long-range surface plasmon–polariton supported by a symmetric metal stripe waveguide that incorporates optically pumped dye molecules in solution as the gain medium. The measured mode power gain is 8.55 dB mm^{-1}. Furthermore, it is shown that this new class of amplifier benefits from reduced spontaneous emission into the amplified mode, potentially leading to low-noise optical amplification.

Surface plasmon–polaritons (SPPs) are transverse magnetic (TM) polarized optical surface waves that propagate along a metal–dielectric interface and whose fields are coupled to charge density oscillations in the metal[1]. SPPs show unique properties including strong electromagnetic field enhancement, subwavelength localization and high sensitivity to the bounding dielectric environment. Such properties make SPPs attractive for applications in fields such as nanophotonics[2], metamaterials[3], imaging[4] and biosensing[5]. However, such applications face limitations imposed by the short lifetimes of SPPs at visible and near-infrared wavelengths, caused by energy dissipation in the metal due to electron collisions and other loss mechanisms. This obstacle has stimulated great interest in understanding the physics of SPP amplification as well as exploring the feasibility of achieving SPP loss compensation using this mechanism[6–23].

The stimulated emission of SPPs has been observed for various planar plasmonic structures. Stimulated emission has been observed in an SPP supported by a silver film in the Kretschmann configuration, coated on its backside with an optically pumped dye solution[15], and in similar structures in which the gain medium comprised a dye-doped polymer[16,17]. In other research, emission has been studied in symmetrical metal-stripe waveguides clad with erbium-doped SiO_2 using a propagating pump arrangement[18]. Grandidier and colleagues[19] demonstrated a 27% increase in the SPP propagation length at telecommunication wavelengths in a quantum-dot-doped polymer-strip-loaded plasmonic waveguide, and Oulton and colleagues[20] demonstrated lasing at visible wavelengths in hybrid plasmon modes supported by a silver film coupled to a cadmium sulphide nanowire. Stimulated emission of SPPs has also been studied in metallic nanostructures. Lasing at telecommunication wavelengths has been observed in metal-coated nanocavities filled with an electrically pumped semiconductor gain medium[21,22], and coherent generation of localized SPPs has been demonstrated at visible wavelengths in an arrangement using gold nanoparticles encapsulated in dye-doped silica shells[23].

Previous studies have argued SPP gain on the basis of a theoretical interpretation of SPP stimulated emission[17] or through the observation of laser-like behaviour of light coupled out of active plasmonic structures[20–23]. In this work we report the first direct measurement of gain in propagating SPPs. The experiments were conducted using the long-range SPP (LRSPP)[24–29] supported by a symmetric gold-stripe plasmonic waveguide[30] incorporating a gain medium in the form of optically pumped dye molecules in solution. We demonstrate that the LRSPP, supported by the structure, propagates with a mode power gain of 8.55 dB mm^{-1}. Furthermore, we show that this class of amplifier benefits from low spontaneous emission into the LRSPP, potentially leading to low-noise optical amplification. We demonstrate a 6.3-dB reduction of spontaneous emission noise in the vicinity of the plasmonic waveguide relative to that in the bulk gain medium.

The realization of LRSPP amplifiers has potential in a number of applications. For instance, the integration of LRSPP amplifiers with grating structures[31,32] could lead to the development of LRSPP lasers that inherit the pure TM polarization of SPP modes, suggesting that a highly polarized output with polarization extinction ratio limited only by the spontaneous emission noise could be achieved. Also, LRSPP amplifiers and lasers could be conveniently integrated with an existing complement of passive optical components[33,34] such as four-port couplers, y-junctions, bandgap structures and Mach–Zehnder interferometers, leading to devices and components with sophisticated functionality. Finally, low-noise optical amplification would improve the performance of biosensors[35].

The LRSPP is not confined to use in very small modal dimensions (subwavelength), but it does propagate with lower loss, which reduces the material gain required to achieve modal gain. Total loss compensation in deep subwavelength SPPs still remains a challenge due to the high propagation losses present, particularly at visible and near-infrared wavelengths.

Results

Guiding structure. The plasmonic waveguides used in the present experiments were derived from wafer X023506.15 as reported in ref. 36, and the fabrication details and results of physical characterization are provided therein. A cross-sectional view of the waveguide structure is shown in Fig. 1a. The gold stripe was 20 nm thick and 1 μm wide, with a root-mean-square (r.m.s.)

[1]School of Information Technology and Engineering, University of Ottawa, 161 Louis Pasteur, Ottawa, Ontario, K1N 6N5, Canada, [2]Department of Physics, University of Ottawa, 150 Louis Pasteur, Ottawa, Ontario, K1N 6N5, Canada, [3]Spectalis Corp., PO Box 72029, Kanata North RPO, Ottawa, Ontario, K2K 2P4, Canada. *e-mail: [redacted]

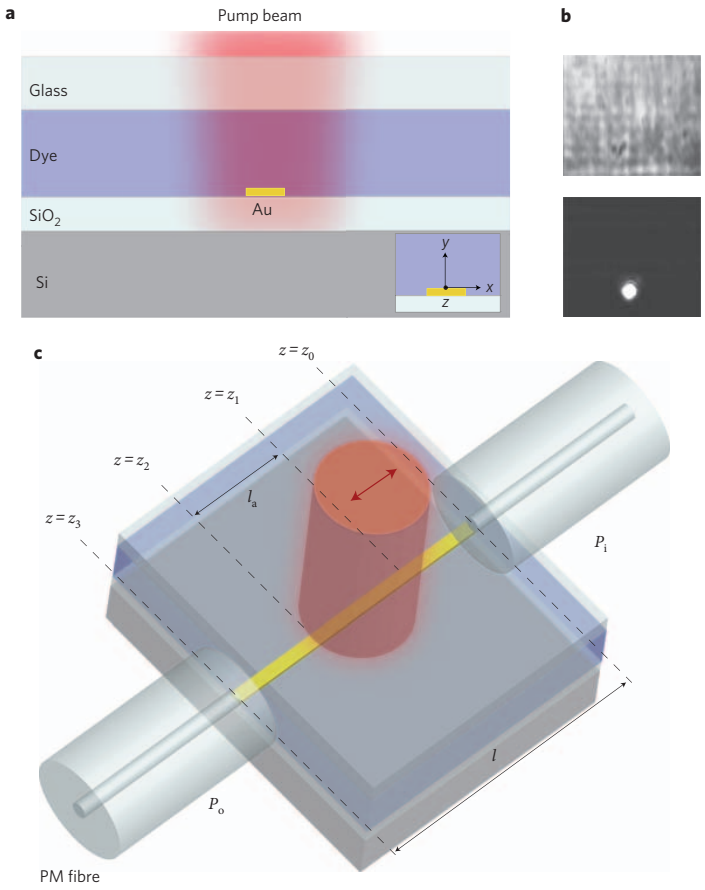

Figure 1 | Guiding structure. a, Cross-sectional view of active structure (not to scale). The gain medium is in the form of a laser dye in solution. Inset: coordinate system with the $+z$-direction coming out of the page. **b**, x-Polarized (top) and y-polarized (bottom) light collected from the output facet of the structure while being pumped by x-polarized light. **c**, Pump and probe signal coupling arrangements used for amplification experiments. Pump polarization, indicated by the red arrow, is parallel to the waveguide length (z-axis). A probe signal is coupled in and out of the structure by means of end-fire coupling using polarization-maintaining (PM) fibres.

surface roughness of less than 1 nm, and lay on a 15-μm-thick SiO_2 layer thermally grown on a silicon substrate and was covered by a gain layer ~100 μm thick consisting of optically pumped IR140 dye molecules (Sigma Aldrich) in solution. The dye was pumped at $\lambda_p = 808$ nm and the LRSPP was probed (excited) at $\lambda_e = 882$ nm, close to the peak absorption and emission of the dye, respectively (see Supplementary Information). The arrangement used for pumping and probing is depicted in Fig. 1c. The pump light was normally incident onto the top side of the structure, linearly polarized along the z-axis, and consisted of 8-ns FWHM (full-width at half-maximum) pulses with a repetition rate of 10 Hz. It uniformly illuminated the central region of the structure with a spot diameter smaller than the length l of the structure. The continuous-wave probe signal was coupled in and out of the LRSPP by means of end-fire coupling using polarization-maintaining fibre (see Methods).

The dye concentration was 1 mM, corresponding to a molecular density of $N = 6 \times 10^{17}$ cm^{-3}, and the solvent was a mixture of 30.4% ethylene glycol and 69.6% dimethyl sulphoxide. At a temperature of 23 °C, the dye solution was index-matched to SiO_2 at λ_e, forming a symmetric waveguiding structure. When fully inverted, the dye is expected to provide a gain of $N\sigma_e \approx 360$ cm^{-1}, with $\sigma_e \approx 6 \times 10^{16}$ being the emission cross-section at λ_e (see Supplementary Information). Figure 1b shows images of light collected from the output facet of the structure while being pumped by x-polarized light and with the LRSPP excited by the probe signal. For the top (bottom) image the output light is passed through a polarizer oriented along the x (y) direction. The bright spot on the bottom image corresponds to the LRSPP intensity profile. It is not visible in the top image because $E_x \approx 0$ for this mode[30]. The brightness of the background in Fig. 1b is proportional to the amplified spontaneous emission (ASE) in the gain medium. Clearly, the ASE is predominantly polarized along the pump electric field (top image), with substantially no emission being measured with orthogonal polarization (bottom image). This suggests a significant degree of gain anisotropy, which follows from the preferential excitation of molecules with a transition dipole moment parallel to the pump electric field and the rather viscous solvent mixture that inhibits molecular reorientation during the short spontaneous emission lifetime of the dye molecule, $\tau \approx 240$ ps (ref. 37).

The rate of stimulated emission into the LRSPP for a pair of energy levels a and b is proportional to the dipole moment matrix element $\mathbf{D}_{ab}$ and the electric field of the LRSPP, $\mathbf{E} = [\sim 0, E_y, E_z]$, and has the following form[38]:

$$W_{ab} \propto |\mathbf{E} \cdot \mathbf{D}_{ab}|^2 \quad (1)$$

Because of the inhibited molecular reorientation, excited molecules have dipole moments oriented predominantly in the (x, z)-plane for

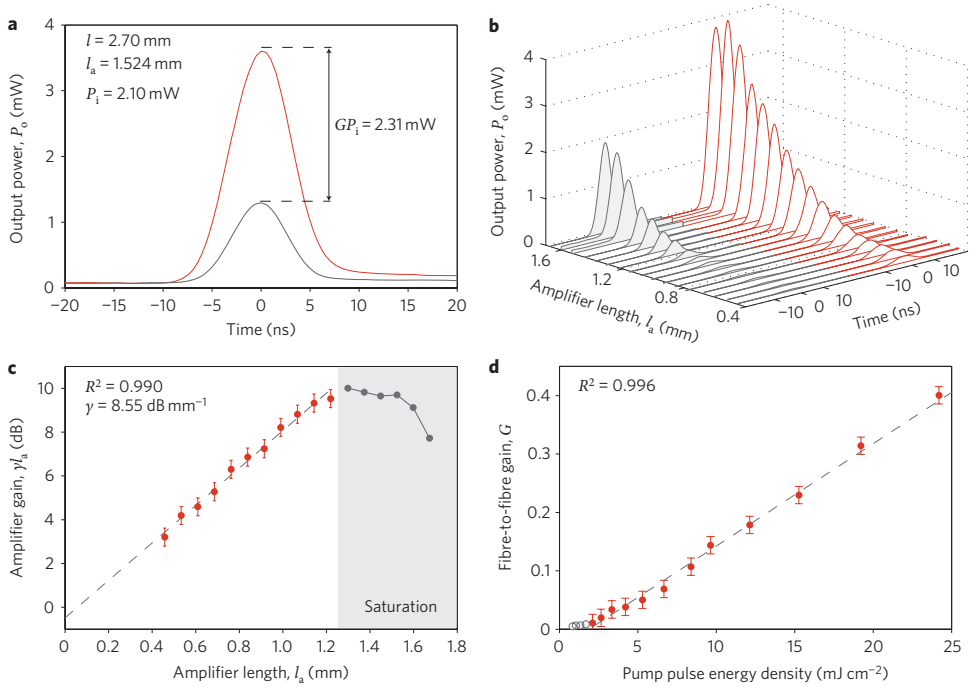

Figure 2 | Active operation. a, Instantaneous power of the amplified probe signal ($P_o = GP_i + \eta$) coupled out of a 2.70-mm-long structure with amplifier length $l_a = 1.524$ mm. The red and grey curves correspond to P_o and η, respectively. The pump energy density and input probe power are set to $E_p = 20 \pm 5$ mJ cm^{-2} and $P_i = 2.10$ mW, respectively. **b**, Measurements of P_o and η as a function of the amplifier length l_a, under the same pump and probe conditions as **a**. **c**, Measurements of amplifier gain versus amplifier length. A linear fit to the unsaturated data yields an LRSPP mode power gain of $\gamma = 8.55$ dB mm^{-1} (error bar, ± 0.412 dB). **d**, Measurements of fibre-to-fibre gain G as a function of the pump energy density for a structure with $l = 2.70$ mm and $l_a = 1$ mm using an input power of $P_i = 0.7$ mW. The linear fit to the data yields an error bar of ± 0.0149.

a normally incident pump of any polarization. For the chosen pump polarization (Fig. 1c), the dot product in equation (1) suggests that LRSPP stimulated emission occurs mainly through the weak E_z field component of the mode, which is approximately two orders of magnitude smaller than E_y (see Supplementary Information). However, as the pump intensity increases, the degree of gain anisotropy is reduced, allowing a stronger interaction of E_y with the gain medium[39,40]. For instance, following the model for an ensemble of randomly oriented rigid dipoles[40], we estimate that for the maximum pump intensity used in our experiments the gain along the y-axis at the surface of the dye layer is ~40% of that along the z-axis.

Passive operation. The passive operation of typical structures was verified before the amplification experiments by measuring the intrinsic mode power attenuation, α_i and the coupling loss per facet C_f by means of cutback[36] at the probe wavelength. Insertion loss measurements were performed on several samples of different lengths using the solvent mixture without dye molecules as the upper cladding to exclude losses due to the ground-state absorption of molecules at λ_e. The measured values of $\alpha_i = 3.06$ dB mm^{-1} and $C_f = 0.360$ dB agree well with theoretical results ($\alpha_i = 3.24$ dB mm^{-1} and $C_f = 0.316$ dB; see Supplementary Information). The low coupling loss guarantees that 92% of the probe power is coupled into the LRSPP. The remaining 8% is reflected, coupled into short-range SPPs (SRSPPs)[30] or coupled into radiation modes. The LRSPP intensity distribution is fairly circular, and its diameter is estimated numerically as ~2.5 μm (see Supplementary Information).

Active operation. During the pump pulse, the structure is composed of three sections defined by the reference planes z_n ($n = 0, 1, 2, 3$) in Fig. 1c. The amplifier section is delimited by the pump beam spot, which covers the region $z_1 < z < z_2$, while two lossy sections, one preceding ($z_0 < z < z_1$) and one following ($z_2 < z < z_3$) the amplifier, are delimited by the unpumped regions. The LRSPP propagates in the $+z$-direction with a complex phase of the form $\exp[(-i\beta + \kappa_n)(z - z_n)]$, where κ_n and β are the field gain ($\kappa_0 = \kappa_2$ being negative) and phase constants, respectively ($e^{i\omega t}$ time-harmonic form assumed). The latter is independent of z, because the real part of the dye refractive index is practically invariant along the structure[37]. Also, for this reason, coupling losses at the planes $z = z_1$ and $z = z_2$ are negligible. The fibre-to-fibre gain expressed in decibels is then given by

$$G_{dB} = \gamma l_a - \alpha_u (l - l_a) - 2C_f \qquad (2)$$

where l_a is the amplifier length, $\gamma = 20\log_{10}(e)\kappa_1$ is the mode power gain due to stimulated emission in the amplifier section, and $\alpha_u = -20\log_{10}(e)\kappa_0$ is the mode power attenuation in the unpumped regions. The latter is larger than α_i due to the ground-state absorption of dye molecules at λ_e.

The power coupled out of the structure (in watts) is given by $P_o = GP_i + \eta$, where P_i is the power delivered by the input fibre, G is the linear fibre-to-fibre gain, and η is the spontaneous emission noise power captured by the output fibre. Figure 2a shows P_o measured with a calibrated a.c.-coupled photoreceiver (see Methods) averaged over 25 pump pulses. The pump pulse energy density is $E_p = 20 \pm 5$ mJ cm^{-2} and the waveguide and amplifier lengths are $l = 2.70$ mm and $l_a = 1.524$ mm, respectively. The grey curve is measured with $P_i = 0$ and corresponds to η. It arises mainly from spontaneous emission into radiation modes (see next section) that fall within the numerical aperture (NA = 0.12) of the fibre integrated over the full emission spectrum of the IR140 dye

molecule, spanning from 850 nm to 930 nm. The red curve is obtained with $P_i = 2.10$ mW. The increment between the two curves represents the amplified mode power GP_i, from which G is obtained straightforwardly. Observe that for this case $GP_i = 2.31$ mW, which yields $G = 1.10$. This indicates not only complete compensation of the losses of the structure (that is, intrinsic mode propagation loss, coupling loss due to both facets and loss due to dye ground-state absorption in the unpumped sections), but also a power gain of 10%. Gain measurements were performed on the same structure for several amplifier lengths over the range $0.457 \leq l_a \leq 1.676$ mm in increments of 0.0762 mm while maintaining the same input power and pump energy density. The resulting curves are shown in Fig. 2b as a function of l_a.

The gain γl_a of the amplifier section is deduced from equation (2) using the fibre-to-fibre gain measurements in Fig. 2b and measured values of C_f (passive operation section) and α_u. The dye behaves as a saturable absorber at λ_e and can present variations due to instabilities during the measurements. To obtain accurate values of α_u, the passive insertion loss ($\alpha_u l + 2C_f$) of the structure is measured *in situ* simultaneously with each of the gain measurements (see Methods). We obtained a value of $\alpha_u = 7.4$ dB mm^{-1} that decreased monotonically by ~0.5 dB mm^{-1} over the duration of the measurements (~5 min). This could be attributed to a slight blueshift in the absorption spectrum caused by photochemical modifications of dye molecules by both pump and probe radiation, probably due to the small volume (~50 μl) and static conditions of the dye solution. The measured amplifier gain is plotted in Fig. 2c as a function of l_a. The linear amplification region is determined as $0 \leq l_a \leq 1.22$ mm by fitting a linear model to data points, adding l_a incrementally from the smallest value until the goodness of fit (as measured by the Pearson product–moment correlation coefficient R^2) began to degrade substantially. The red data points (Fig. 2c) were selected in this manner to participate in the linear model, whereas the grey ones were deemed to fall within the non-linear region of the amplifier. The slope of the linear model yields $\gamma = 8.55$ dB mm^{-1}, with error bars of ± 0.412 dB and $R^2 = 0.990$. The coupling loss at the amplifier interfaces (planes z_1 and z_2) is obtained as the intercept, yielding 0.48 dB. This deviation from the expected value of zero is comparable to the experimental error. Clearly, for $l_a > 1.22$ mm, the amplifier gain is not linear; this is attributed mainly to mode gain saturation.

A signature of stimulated emission is the linear (unsaturated) gain behaviour as a function of the pump energy density E_p. To strengthen the observation of stimulated emission into the LRSPP, fibre-to-fibre gain (G) measurements are plotted in Fig. 2d as a function of E_p, while maintaining a fixed amplifier length of $l_a = 1$ mm (for the 2.70-mm-long structure) and constant input power of $P_i = 0.7$ mW. Gain measurements for $E_p \leq 2$ mJ cm^{-2} (open circles) fall below the noise level of our detection system. For larger values of E_p the linearity of G is supported by an excellent linear fit with $R^2 = 0.996$. No saturation effects are observed within the measurement range of $2 < E_p < 24.5$ mJ cm^{-2}.

Reduced spontaneous emission noise. In a plasmonic amplifier, the spontaneous emission exhibits a complex behaviour due to a variety of energy decay channels engendered by the metal[42–44]. For the structure investigated here, these decay channels include spontaneous emission into the radiation modes of the structure, spontaneous emission into the LRSPP and SRSPP modes, and coupling to electron–hole pairs in the metal film, where the energy is directly transferred from the molecule to carriers in the metal by means of a dipole–dipole interaction. Excited molecules preferentially relax through specific decay channels depending on their distance from the metal and their dipole–moment orientation. To illustrate this phenomenon, we consider for simplicity the one-dimensional variant of the structure in Fig. 1a

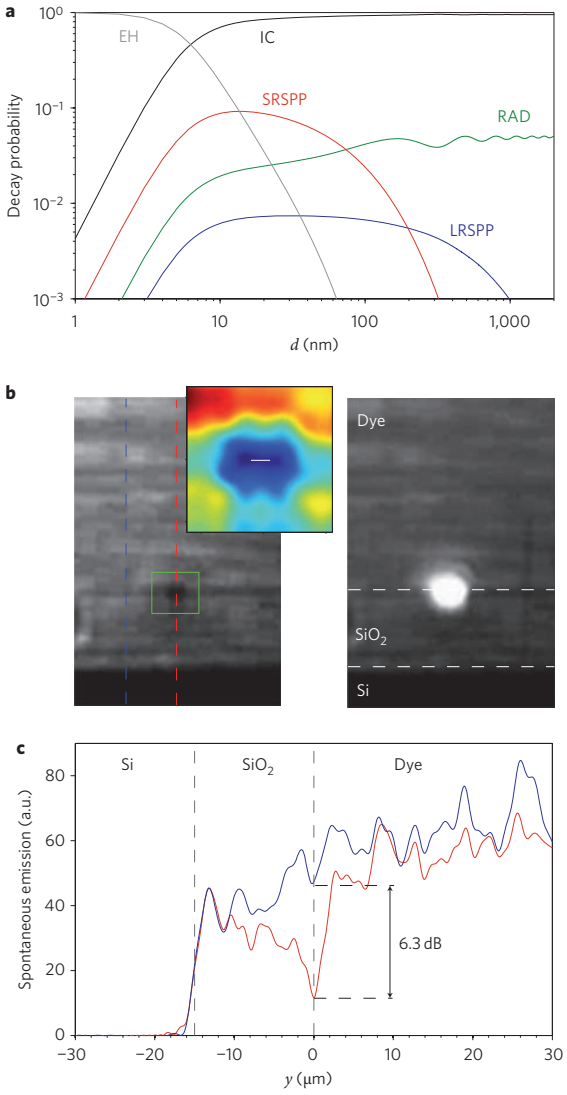

Figure 3 | Reduced spontaneous emission. a, Decay probability of isotropically oriented dipoles near a metal slab into various channels calculated for the one-dimensional variant of the structure on Fig. 1a. **b**, Light collected from the output facet of a structure pumped with *z*-polarized light. Left image, probe off; right image; probe on. The inset shows the intensity distribution (in false colour scale) near the 1-μm-wide metal stripe (indicated by the white line). **c**, Spontaneous emission intensity distribution in arbitrary units along the vertical cuts indicated by the red and blue dashed lines in **b** (left). EH, electron-hole pair; IC, internal conversion; SRSSP, short-range surface plasmon-polarition; RAD, radiative modes.

(infinite metal stripe width) with a semi-infinite gain medium formed of isotropically excited dipoles. The decay probabilities are shown in Fig. 3a as a function of molecule–metal separation d. These curves are computed using the classical theory of molecular fluorescence near a metal (see Methods). Molecules relax mainly via non-radiative channels, that is, through internal conversion for $d > 5$ nm due to the low quantum efficiency of IR140 ($\phi \approx 0.05$) and through coupling to electron–hole pairs in the metal for $d < 5$ nm. The remaining channels involve spontaneous emission into modes of the structure (LRSPP, SRSPP and radiative modes, RAD) and contribute to the optical noise of

the amplifier. Note that spontaneous emission into the SRSPP is the dominant decay channel for $d < 100$ nm, being 10 and 5 times more probable than decay into the LRSPP and RAD channels, respectively. For $d > 100$ nm, the RAD channel dominates, being at least 5 times more probable than decay into the LRSPP channel.

Consider now Fig. 3b, which shows images of light collected from the output facet of a structure with $l = 1.8$ mm and $l_a = 1.05$ mm while being pumped by z-polarized light. The images on the left and right correspond to cases where the probe signal is turned off and on, respectively. The background fluorescence is randomly polarized, as expected from a collection of excited molecules with a symmetrical dipole–moment distribution about the z-axis[41]. From the image on the left, a significant reduction of spontaneous emission is observed near the metal stripe compared to the background. The inset enlarges this region, scaling the light intensity in false colour. Figure 3c shows the spontaneous emission intensity distribution along the two cuts indicated by the vertical dashed lines in Fig. 3b (left). The red curve corresponds to the cut approximately through the centre of the metal stripe and the blue curve corresponds to a cut shifted approximately 10 μm to the left of the metal stripe. The latter corresponds to spontaneous emission into radiation modes; molecules are distant enough from the metal stripe that their fluorescence is not affected. The spontaneous emission reduction relative to the emission in the bulk is 6.3 dB, as given by the difference between the two curves at $y \approx 0$. These curves are obtained from a diffraction-limited image, so the low-intensity region is blurred by the surrounding light. The measured reduction is therefore probably underestimated.

These measurements could be explained qualitatively by elements of the decay calculations shown in Fig. 3a. First, the spontaneous emission probability into the LRSPP is much smaller than that of the main radiative decay channels near the metal. The LRSPP therefore conveys little spontaneous emission to the output facet. Second, the probability of spontaneous emission into radiative modes is considerably reduced close to the metal. Third, the large emission into the SRSPP is quickly absorbed by the metal (through high modal loss), so the SRSPP also conveys little emission to the output facet. Finally, the fluorescence quenching caused by coupling to electron–hole pairs in the metal also reduces the spontaneous emission; however, it affects only a small region near the metal.

The gain and low spontaneous emission noise into the LRSPP are important attributes of this class of amplifier. Furthermore, the large spontaneous emission into the SRSPP combined with its large propagation loss equips the amplifier with an efficient quenching mechanism of guided noise. These attributes suggest the possibility of low-noise optical amplification through the LRSPP, provided that the LRSPP can be isolated from the unguided noise carried by the radiation modes of the structure.

Methods

Experimental set-up. For the amplification measurements the active waveguide structure was mounted on a thermo-electric cooling device to stabilize the temperature of the dye solution to 23 °C and avoid refractive index fluctuations due to thermo-optic effects. The active waveguide was also enclosed in a nitrogen capsule to provide the dry environment necessary to stabilize the hygroscopic dye solution. The pump light, consisting of 8-ns (FWHM) pulses with a repetition rate of 10 Hz, was generated with a frequency-doubled Nd:YAG pumped dye laser (Spectra-Physics Mod. Quanta-Ray Lab10/Cobra-Stertch). The energy and polarization of the pump beam were controlled with a $\lambda/2$ wave plate followed by a Glan-Laser polarizer, and its spot size, which defines the amplifier section was carefully controlled with a micrometre driven variable slit.

For both passive (without dye molecules and with unpumped dye molecules) and active measurements, a tuneable c.w. Ti:sapphire laser (Spectra-Physics Mod. 3900 CW) coupled to a panda-type polarization-maintaining (PM) fibre (Thorlabs Mod. PM780-HP) was used to generate the probe signal. This was then passed through a 10-dB PM fibre splitter, which was used to monitor the input power in real time during the measurements. The LRSPP was coupled in and out of the structure via end-fire coupling using the same type of PM fibre. Both fibres were mounted on five-axis micropositioners and carefully aligned to the waveguide structure in terms of position and polarization. Light collected by the output fibre was collimated and passed through a TM polarizer to remove residual transverse electric (TE) light. A 3-dB splitter then divided the signal into two branches, one of which delivered the signal to a calibrated a.c.-coupled fast photoreceiver (Newport Mod. 818-BB-21A) to perform the gain measurements. The photoreceiver was monitored with a radio-frequency oscilloscope, which in turn was synchronized to the 10-Hz pump signal. All gain measurements were averaged over 25 pump pulses to minimize errors due to possible pulse-to-pulse energy variations. The second branch delivered the optical signal to a low-power c.w. photodetector (Newport Mod. 918D-SL), which was used to monitor the insertion loss of the structure during the measurements. Because the amplified signal was only 8 ns in duration, it did not significantly alter the average power of the c.w. component. Hence, the value measured by the low-power c.w. photodetector was used to compute the passive insertion loss (unpumped) of the structure, given by $\alpha_u l + 2C_f$.

For the measurements of gain anisotropy and reduced spontaneous emission, the light intensity distribution at the output facet of the structure was imaged onto a vidicon-type infrared camera (Electrophysics Mod. MicronViewer 7290) equipped with an 808-nm blocking filter using a ×20 microscope objective. Gain anisotropy was measured by placing a polarization filter before the camera to visualize the spontaneous emission with a particular electric field component; no polarization filter was used for the measurement of reduced spontaneous emission. For both measurements, the camera recorded images over a long time interval, capturing the dye spontaneous emission and LRSPP intensities at a frame rate of 50 Hz. Images presented throughout the paper correspond to video frames where the recorded spontaneous emission is maximum. Images were corrected for the background intensity (ambient light) by subtracting from every pixel of an image the grey-scale value of the bottom pixel in the silicon layer. Because silicon absorbs efficiently over the emission spectrum of the dye, the subtracted value does not affect the spontaneous emission level.

Numerical techniques. The probabilities of energy decay into the different channels in the vicinity of the metallic film were obtained following the classical theory of molecular fluorescence near metallic surfaces; refs 42–44 provide a comprehensive discussion of the theory. The material refractive indices used in our simulations are those used for modelling the passive structure (see Supplementary Information). To account approximately for electron screening in the metal (which becomes important only when the distance between the molecule and the metal is a few nanometres) we considered only dipole field components with in-plane wave vectors $k_{\|}$ within the electron–hole excitation continuum of gold at λ_e; that is, $k_{\|} < (2m_e\omega_e/\hbar + k_F^2)^{1/2} + k_F$, where k_F is the Fermi wave vector, $\hbar$ is the reduced Planck's constant, m_e is the electron mass and ω_e is the angular frequency of light.

Received 3 September 2009; accepted 17 February 2010; published online 28 March 2010

References

1. Raether, H. *Surface Plasmons on Smooth and Rough Surfaces and on Gratings* (Springer, 1988).
2. Barnes, W. L., Dereux, A. & Ebbesen, T. W. Surface plasmon subwavelength optics. *Nature.* **424,** 824–830 (2003).
3. Shalaev, V. M. Optical negative-index metamaterials. *Nature Photon.* **1,** 41–48 (2007).
4. Kawata, S., Inouye, Y. & Verma, P. Plasmonics for near-field nano-imaging and superlensing. *Nature Photon.* **3,** 388–394 (2009).
5. Anker, J. N. *et al.* Biosensing with plasmonic nanosensors. *Nature Mater.* **6,** 442–453 (2008).
6. Bergman, D. J. & Stockman, M. I. Surface plasmon amplification by stimulated emission of radiation: quantum generation of coherent surface plasmons in nanosystems. *Phys. Rev. Lett.* **90,** 027402 (2003).
7. Nezhad, M. P., Tetz, K. & Fainman, Y. Gain assisted propagation of surface plasmon polaritons on planar metallic waveguides. *Opt. Express.* **12,** 4072–4079 (2004).
8. Avrutsky, I. Surface plasmons at nanoscale relief gratings between a metal and a dielectric medium with optical gain. *Phys. Rev. B.* **70,** 155416 (2004).
9. Okamoto, T., H'Dhili, F. & Kawata, S. Towards plasmonic band gap laser. *Appl. Phys. Lett.* **85,** 3968–3970 (2004).
10. Maier, S. A. Gain-assisted propagation of electromagnetic energy in subwavelength surface plasmon polariton gap waveguides. *Opt. Commun.* **258,** 295–299 (2006).
11. Winter, G., Wedge, S. & Barnes, W. L. Can lasing at visible wavelength be achieved using the low-loss long-range surface plasmon–polariton mode? *New J. Phys.* **8,** 125 (2006).
12. Alam, M. Z., Meier, J., Aitchison, J. S. & Mojahedi, M. Gain assisted surface plasmon polariton in quantum well structures. *Opt. Express.* **15,** 176–182 (2007).
13. De Leon, I. & Berini, P. Theory of surface plasmon–polariton amplification in planar structures incorporating dipolar gain media. *Phys. Rev. B.* **78,** 161401(R) (2008).
14. De Leon, I. & Berini, P. Modeling surface plasmon–polariton gain in planar metallic structures. *Opt. Express.* **17,** 20191–20202 (2009).

15. Seidel, J., Grafstrom, S. & Eng, L. Stimulated emission of surface plasmons at the interface between a silver film and an optically pumped dye solution. *Phys. Rev. Lett.* **94,** 177401 (2005).
16. Noginov, M. A. *et al.* Compensation of loss in propagating surface plasmons polariton by gain in adjacent dielectric medium. *Opt. Express.* **16,** 1385–1392 (2008).
17. Noginov, M. A. *et al.* Stimulated emission of surface plasmon polaritons. *Phys. Rev. Lett.* **101,** 226806 (2008).
18. Ambati, M. *et al.* Observation of stimulated emission of surface plasmon polaritons. *Nano Lett.* **8,** 3998–4001 (2008).
19. Grandidier, J. *et al.* Gain-assisted propagation in a plasmonic waveguide at telecom wavelength. *Nano Lett.* **9,** 2935–2939 (2009).
20. Oulton, R. F. *et al.* Plasmon lasers at deep subwavelength scale. *Nature*. **461,** 629–632 (2009).
21. Hill, M. T. *et al.* Lasing in metallic-coated nanocavities. *Nature Photon*. **1,** 589–594 (2007).
22. Hill, M. T. *et al.* Lasing in metal–insulator–metal sub-wavelength plasmonic waveguides. *Opt. Express*. **17,** 11107–11112 (2009).
23. Noginov, M. A. *et al.* Demonstration of a spaser-based nanolaser. *Nature.* **460,** 1110–1113 (2009).
24. Kovacs, G. J. Optical excitation of surface plasma waves in an indium film bounded by dielectric layers. *Thin Solid Films* **60,** 33–44 (1979).
25. Fukui, M. *et al.* Lifetimes of surface plasmons in thin silver films. *Phys. Stat. Sol. B.* **91,** K61–K64 (1979).
26. Sarid, D. Long-range surface-plasma waves on very thin metal films. *Phys. Rev. Lett.* **47,** 1927–1930 (1981).
27. Burke, J. J., Stegeman, G. I. & Tamir, T. Surface-polariton-like waves guided by thin, lossy metal films. *Phys. Rev. B.* **33,** 5186–5201 (1986).
28. Yang, F., Sambles, J. R., & Bradberry, G. W. Long-range surface modes supported by thin films. *Phys. Rev. B.* **44,** 5855–5872 (1991).
29. Berini, P. Long-range surface plasmon polaritons. *Adv. Opt. Photon*. **1,** 484–588 (2009).
30. Berini, P. Plasmon–polariton waves guided by thin lossy metal films of finite width: bound modes of symmetric structures. *Phys. Rev. B.* **61,** 10484–10503 (2000).
31. Jette-Charbonneau, S., Charbonneau, R., Lahoud, N., Mattiussi, G. & Berini, P. Bragg gratings based on long-range surface plasmon-polariton waveguides: comparison of theory and experiment. *IEEE J. Quantum Electron*. **98,** 1480–1491 (2005).
32. Bozhevolnyi, S. I., Boltasseva, A., Sondergaard, T., Nikolajsen, T. & Leosson, K. Photonic bandgap structures for long-range surface plasmon polaritons. *Opt. Commun.* **250,** 328–333 (2005).
33. Charbonneau, R. *et al.* Passive integrated optics elements based on long-range surface plasmon polaritons. *J. Lightwave Technol.* **24,** 477–494 (2006).
34. Boltasseva, A. *et al.* Integrated optical components utilizing long-range surface plasmon polaritons. *J. Lightwave Technol.* **23,** 413–422 (2005).
35. Berini, P. Bulk and surface sensitivities of surface plasmon waveguides. *New J. Phys.* **10,** 105010 (2008).
36. Berini, P., Charbonneau, R., Lahoud, N. & Mattiussi, G. Characterization of long-range surface-plasmon-polariton waveguides. *J. Appl. Phys.* **98,** 043109 (2005).
37. Sperber, P., Spangler, W., Meier, B. & Penzkofer, A. Experimental and theoretical investigation of tunable picosecond pulse generation in longitudinally pumped dye laser generators and amplifiers. *Opt. Quantum Electron*. **20,** 395–431 (1988).
38. Bransden, B. H. & Joachain, C. J. *Physics of Atoms and Molecules* (Longman, 1983).
39. Mourou, G. & Denariez, M. M. Polarization of fluorescence and bleaching of dyes in a high-viscosity solvent, *IEEE J. Quantum Electron*. **QE9,** 787–790 (1973).
40. Reyzer, K. C. & Casperson, L. W. Polarization characteristics of dye-laser amplifiers II. Isotropic molecular distribution. *J. Appl. Phys.* **51,** 6083–6090 (1980).
41. Valeur, B. *Molecular Fluorescence, Principles and Applications* (Wiley-VCH, 2002).
42. Chance, R. R., Prock, A. & Silbey, R. Molecular fluorescence and energy transfer near interfaces. *Adv. Chem. Phys.* **37,** 1–65 (1978).
43. Ford, G. W. & Weber, W. H. Electromagnetic interactions of molecules with metal surfaces. *Phys. Rep.* **113,** 195–287 (1984).
44. Barnes, W. L. Fluorescence near interfaces: the role of photonic mode density. *J. Mod. Opt.* **45,** 661–699 (1998).

Acknowledgements

The authors thank Prof. J.C. (Tito) Scaiano, M. Grenier, and other members of the photochemistry laboratory at the University of Ottawa for their assistance in measuring the IR140 absorption spectrum. This work was generously supported by the Natural Sciences and Engineering Research Council of Canada.

Author contributions

I.D.L. carried out the experimental work, performed the theoretical analysis, and prepared the manuscript. P.B. directed the project and contributed to the manuscript preparation. I.D.L and P.B. designed the experiments and the set-up, and analysed and interpreted the experimental results.

Additional information

The authors declare no competing financial interests. Supplementary information accompanies this paper at www.nature.com/naturephotonics. Reprints and permission information is available online at http://npg.nature.com/reprintsandpermissions/. Correspondence and requests for materials should be addressed to P.B.

nature photonics

SUPPLEMENTARY INFORMATION

DOI: 10.1038/NPHOTON.2010.37

IR140 emission and absorption spectra. The IR140 molecule is a commercial tricarbocyanine used typically as a laser dye. Figure 1 shows the normalized absorption and fluorescence spectra of molecules dissolved in a mixture of 69.6 % dimethyl sulfoxide and 30.4 % ethylene glycol. The fluorescence spectrum of the 1 mM dye sample was measured with a near-infrared spectrometer (Oriel Mod. OSM2-400) using a 500 μm path-length cell capable of holding 50 μL of dye and a tungsten halogen lamp continuous wave excitation source. For the absorption measurements the dye sample was diluted approximately 300 times ($C \approx 3$ μM) in 3 mL of dye solvent and the spectrum was measured using a spectrophotometer (Varian Inc. Mod. Cary-100).

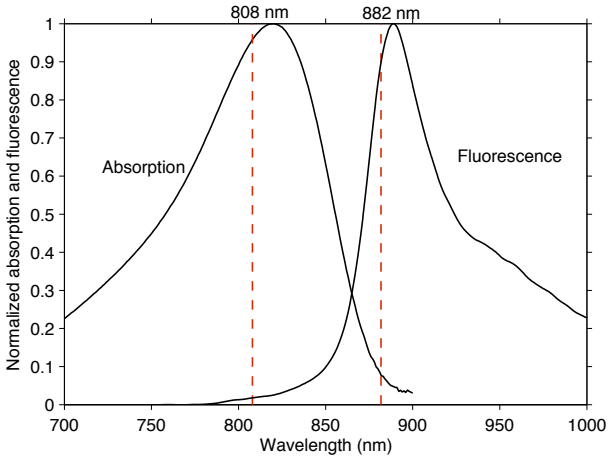

Figure 1 | IR140 dye absorption and fluorescence spectra. Normalized absorption ($C \approx 3$ μM) and fluorescence ($C = 1$ mM) spectra. The vertical dashed lines indicate the pump ($\lambda_p = 808$ nm) and probe ($\lambda_e = 882$ nm) wavelengths used for the experimentation.

The absorption spectrum presents a broad peak with FWHM (full width half maximum) bandwidth of 98 nm centred around $\lambda_{a,0} = 819$ nm. The fluorescence spectrum is considerably narrower, having FWHM bandwidth of 50 nm centred at $\lambda_{e,0} = 889$ nm. The vertical dashed lines in Figure 1 indicate the pump ($\lambda_p = 808$ nm) and probe ($\lambda_e = 882$ nm) wavelengths. Using the peak absorption and emission cross-sections given in Ref. 1 we approximate the cross-sections as $\sigma_a(\lambda_p) \approx 5.7 \times 10^{-16}$ cm^2, $\sigma_a(\lambda_e) \approx 4 \times 10^{-17}$ cm^2, and $\sigma_e(\lambda_e) \approx 6 \times 10^{-16}$ cm^2.

Passive operation of plasmonic structure. The passive operation of typical structures used for the experimentation was verified prior to the amplification experiments by measuring the intrinsic mode power attenuation, α_i, and the coupling loss per facet, C_f, via cutback [2]. A continuous-wave probe signal of wavelength λ_e is coupled in and out of the structure via end-fire coupling using polarisation-maintaining fibers in the same way as for the active experiments (see Fig. 1c in main text). The insertion loss of five waveguides of different length was measured using the solvent mixture without dye molecules as upper cladding to exclude losses due to the ground-state absorption of molecules

DOI: 10.1038/NPHOTON.2010.37

at λ_e. The insertion loss measurements are plotted in Fig. 2a as a function of the waveguide length and a linear model is fitted to the data using the linear least squares approach. The goodness of the fit as given by the squared Pearson product-moment correlation coefficient is $R^2 = 0.985$. A value of $\alpha_i = 3.06$ dB/mm is deduced from the slope of the linear model and the coupling loss due to both facets $2C_f = 0.72$ dB is obtained as the intercept. The low coupling loss guarantees that 92% of the probe power is coupled into the LRSPP. The remaining 8% is reflected, coupled into short-range SPPs (SRSPPs) also supported by the structure [3], or coupled into radiation modes. The inset in Fig. 2a shows a typical mode intensity profile measured at the output of a passive waveguide. The absence of light in the background indicates that most of the input power is coupled into the LRSPP as expected.

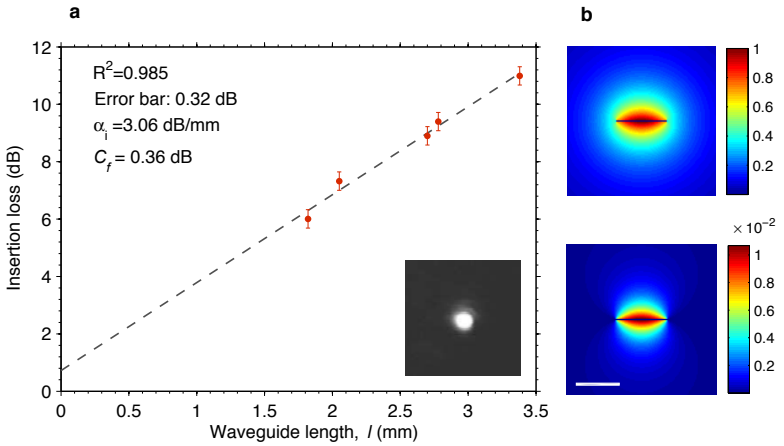

Figure 2 | **Passive operation. a,** Attenuation and coupling loss measurements at $\lambda_e = 882$ nm of passive waveguide structures cladded with the solvent mixture without dye. The inset shows a typical measured mode intensity profile. **b,** Computed $|E_y|^2$ (top) and $|E_z|^2$ (bottom) fields of the LRSPP mode. The scale bar is 1 μm and applies for both top and bottom figures.

A commercial finite-element package (Comsol Multiphysics) was used to solve Maxwell's equations in the passive structure (without dye molecules) to obtain the theoretical mode intensity profile and intrinsic mode power attenuation of the LRSPP. In our simulations we use the bulk refractive index of SiO_2 and Si given in Ref. 4. Previous characterisation of these waveguides showed that the refractive index of the 20 nm gold film deviates from its bulk value [2]. To account for this deviation we estimate the refractive index of the gold stripe using the approximation in Ref. 2; i.e., $n_{\mathrm{Au},20} = 1.5\ \mathrm{Re}(n_{\mathrm{Au}}) + i0.92\ \mathrm{Im}(n_{\mathrm{Au}})$, where n_{Au} is the bulk refractive index of gold obtained from Ref. 4. The experimental results are in good agreement with the obtained theoretical values, $\alpha_i = 3.24$ dB/mm and $2C_f = 0.632$ dB. The coupling efficiency per facet is obtained by computing the overlap between the LRSPP and the fundamental fibre mode [2]. We modelled the fibre mode profile as Gaussian with a mode field diameter of 6.442 μm, measured as the e^{-2} diameter of the mode power distribution. The LRSPP mode is fairly circular and its diameter is 2.54 μm, as given by the e^{-2} diameter of the computed $|E_y|^2$ field distribution.

The computed $|E_y|^2$ and $|E_z|^2$ distributions are shown in the top and bottom panes of Fig. 2b, respectively. The magnitude squared of both fields is normalized to $|E_y|^2$. Note that $|E_z|^2$ is two orders of magnitude smaller than $|E_y|^2$.

From equation (1) in the main text, it follows that a stronger amplification is expected with a transverse *y*-polarised pump arrangement such that excited molecules have a dipole moment oriented predominantly along the *y*-axis and thus parallel to the main field component of the LRSPP, E_y. Such a pump arrangement however is less convenient and adds experimental complexity.

Gold surface degradation. Scanning electron microscope images obtained for two representative samples, one before and one after a series of amplification experiments, are shown in Fig. 3a and b, respectively. The image taken after the amplification experiments clearly suggests a modification to the gold film and reveals what appears to be the beginning of a slight gold islandisation. We believe that the islandisation is due to local heating of the gold film during the pump pulse. Slight islandisation as observed in Fig. 3b can degrade the performance of the waveguide but not catastrophically. A discussion of the optical properties and experimental review of LRSPP modes on islandised films can be found in Ref 5.

A measurement of the intrinsic mode power attenuation (α_i) taken after the amplification experiments (reported in Figs. 2c and d of main text) showed a slight increase of 0.26 dB/mm with respect to the original measurement taken prior to any amplification test. This is attributed to a gold surface degradation; however, it is not clear if the condition of the gold film during the measurement was comparable to that shown in Fig. 3b.

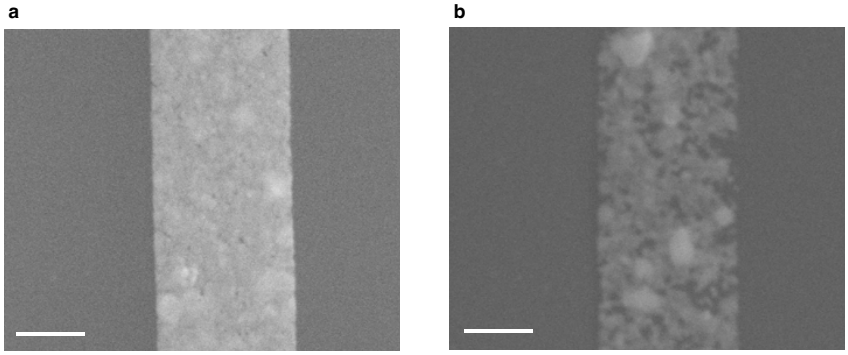

Figure 3 | Gold surface degradation. Scanning electron microscope images of two representative structures used for the experimentation: **a,** prior amplification experiments and **b,** after a series of amplification experiments. The scale bars are 500 nm.

References

1. Sperber, P., Spangler, W., Meier, B. & Penzkofer, A. Experimental and theoretical investigation of tunable picosecond pulse generation in longitudinally pumped dye laser generators and amplifiers. *Opt. Quant. Electron.* **20,** 395-431 (1988).

2. Berini, P., Charbonneau, R., Lahoud, N. & Mattiussi, G. Characterization of long-range surface-plasmon-polariton waveguides. *J. App. Phys.* **98,** 043109 (2005).

3. Berini, P. Plasmon-polariton waves guided by thin lossy metal films of finite width: Bound modes of symmetric structures. *Phys. Rev. B.* **61,** 10484-10503 (2000).

4. Palik, E. D. *Handbook of Optical Constants of Solids*. (Academic Press, New York, 1985).

5. Berini, P. Long-range surface plasmon polaritons. *Adv. Opt. Photon.* **1** 484-588 (2009).

CHAPTER 5

Spontaneous emission in long-range SPP amplifiers

5.1 Summary

This chapter presents and discusses experimental findings on spontaneous emission and ASE of LRSPPs (ASE-LRSPP) in a plasmonic amplifier similar to that described in Chapter 4. The experimental results demonstrate an effective noise input power of 7.47×10^{-4} fW/Hz at the peak ASE-LRSPP wavelength. The effective noise input power is the power at the amplifier's input needed to produce an output signal with unitary signal to noise ratio; it can also be interpreted as the power at the input of the idealised (noiseless) amplifier needed to generate an output signal with power equal to the measured noise signal. The measured noise level is close to the theoretical limit of linear (phase-insensitive) optical amplifiers. A theoretical model to describe ASE of SPPs in modes supported by planar structures is presented. The theory links the amplifier's noise to the spontaneous emission rate into the amplified mode. The model is applied to the experimental situation and provides good agreement with the experimental results.

5.2 Contribution

The results provided in this chapter have been accepted for publication as a *Rapid Communication* in the journal *Physical Review B*. I designed and built the experimental setup; I developed the active structure used for the experimentation based on a passive waveguide provided by Dr. Berini; I developed the theoretical model and implemented the numerical methods used for the theoretical analysis; I generated and interpreted the theoretical and experimental results, and wrote the manuscript. Dr. Berini contributed to the design of the experiments and experimental setup, the interpretation of the results, and revised the manuscript.

5.3 Article

The submitted article follows verbatim.

Spontaneous emission in long-range surface plasmon-polariton amplifiers

Israel De Leon*
School of Information Technology and Engineering, University of Ottawa, 161 Louis Pasteur, Ottawa, Ontario, K1N 6N5, Canada.

Pierre Berini†
School of Information Technology and Engineering, University of Ottawa, 161 Louis Pasteur, Ottawa, Ontario, K1N 6N5, Canada.
Department of Physics, University of Ottawa, 150 Louis Pasteur, Ottawa, Ontario, K1N 6N5, Canada.

(Dated: February 8, 2011)

Measurements of amplified spontaneous emission are conducted on a long-range surface plasmon-polariton amplifier consisting of a symmetric metallic waveguide incorporating a gain medium in the form of optically pumped dye molecules in solution. An effective input noise power per unit bandwidth of 7.47×10^{-4} fW/Hz is measured at $\lambda = 876$ nm, which is 3.3 times larger than the theoretical minimum for phase-insensitive optical amplifiers. A semi-classical theoretical model describing the amplified spontaneous emission of long-range surface plasmon-polaritons (and other types of surface plasmon modes) is proposed, finding good agreement with experimental results. It is shown that the amplifier's low noise follows from a low spontaneous emission rate of long-range surface plasmon-polaritons.

PACS numbers: 78.45.+h, 42.55.Ah, 73.20.Mf, 42.82.Et

Surface plasmon-polaritons (SPPs) are lossy transverse-magnetic (TM) polarised surface waves formed through the interaction of photons with free electrons at the surface of metals[1]. The spontaneous emission rate of optical dipoles can be significantly enhanced in the vicinity of metallic surfaces mostly because the supported SPPs increase the density of electromagnetic modes through which the excited dipoles can relax[2]. This effect has been exploited to achieve single molecule detection[3], and to develop devices with enhanced photoluminescence[4] and fluorescence[5]. Spontaneous emission is a phenomenon of central importance in optical amplifiers and lasers as it is a form of noise that limits the performance of optical systems. Recent work on SPP amplification[6–17] provides strong motivation for studying this phenomenon in active plasmonic devices. It has been shown that SPP-enhanced spontaneous emission can lead to a low threshold plasmonic laser[13]. But it can reduce[18] and limit[19] the gain available for SPP amplification.

Thin metal films or stripes bounded by symmetric dielectrics support bound modes termed long-range SPPs (LRSPPs) and short-range SPPs (SRSPPs)[20]. LRSPPs are less confined to the metal and exhibit much lower propagation loss than SRSPPs and single-interface SPPs. In this type of structure, the spontaneous emission rate of dipoles close to the metal is also affected by SPPs; however, most of the spontaneous emission is in the form of SRSPPs while only a small fraction is in the form of LRSPPs[18,21], suggesting the possibility of low-noise optical amplification with LRSPPs[15].

In this paper we present quantitative measurements of amplified spontaneous emission (ASE) noise power in a LRSPP amplifier. We report plasmonic amplification with a noise level that is close to the theoretical minimum for phase-insensitive optical amplifiers. A theoretical model describing ASE of LRSPPs (ASE-LRSPP) is proposed, directly linking the amplifier noise to the spontaneous emission rate of LRSPPs. The theory is applied to the experimental situation showing good agreement with the measurements.

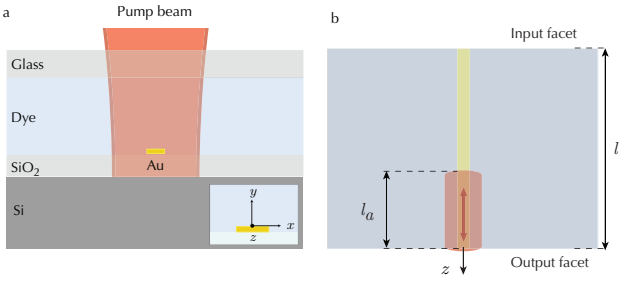

FIG. 1. (Colour online) (a) Cross-sectional view of active structure (not to scale). Inset: coordinate system with the $+z$-axis coming out of the page. (b) Top view; the pump polarisation indicated by the red arrow.

A schematic cross-sectional view of the plasmonic structure used for the experimentation is shown in Fig. 1a. It consist of a 20 nm-thick and 1 μm-wide gold stripe of length $l = 1.45$ mm on a 15 μm-thick SiO_2 layer thermally grown on a Si substrate. Details of fabrication and physical characterisation of similar structures are given in Ref. 22. The gold stripe is covered by a gain medium in the form of optically pumped IR140 dye molecules in solution. A 150 μm-thick glass slide lies on top of the dye holding it to within a ~ 90 μm-thick layer. The dye concentration is 0.5 mM, corresponding to a molecular density of 3×10^{17} cm^{-3} and the solvent (30.4% ethylene glycol and 69.6% dimethyl sulfoxide) is index matched to SiO_2 at 23° C. All experiments are carried out at this temperature, with the dye flowing at a constant rate of 1 μL/min.

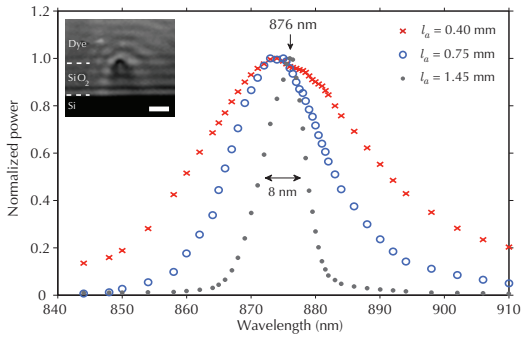

FIG. 2. (Colour online) Measured ASE-LRSPP spectra for three different amplifier lengths. Inset: ASE intensity distribution at the output facet as captured by an infra-red camera (scale bar is 10 μm).

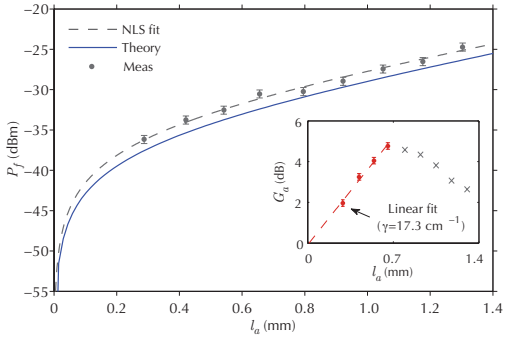

FIG. 3. (Colour online) The ASE-LRSPP power in the fibre at $\lambda_{\rm ASE}$ for several values of l_a. Inset: Amplifier gain versus l_a obtained from LRSPP stimulated emission measurements.

The dye is pumped with pulsed light of wavelength 810 nm, pulse duration of 8 ns, and pulse energy of $\sim$ 10 mJ/cm^2, normally incident onto the top of the structure and linearly polarised along the waveguide's longitudinal axis. Fig. 1b illustrates a top-view of the structure. The pump beam is shaped into a stripe of width $\sim$ 150 μm and illuminates the end region of the waveguide, defining an amplifier section of length l_a. As the structure is pumped, the LRSPP spontaneous emission at the output facet is extracted from the structure via butt-coupling to a polarisation-maintaining fibre carefully aligned to the waveguide in position and (TM) polarisation. The signal exiting the fibre is then filtered by a TM polariser followed by a monochromator with a full-width-half-maximum (FWHM) optical bandwidth of $B_\lambda = 1.2$ nm. Finally, the filtered signal is measured using a calibrated AC-coupled avalanche photodetector module (see supplementary information for details on experimental techniques).

Fig. 2 shows LRSPP spontaneous emission spectra measured for three values of l_a by scanning the monochromator in the range $840 \leq \lambda \leq 910$ nm. The spectrum narrows as l_a increases to a FWHM linewidth of 8 nm when $l_a = l$. Spectral linewidth narrowing with increasing amplifier lengths for a fixed pump energy (or vice-versa) is characteristic of ASE[23]. Thus, the observed linewidth narrowing indicates that the dye provides enough gain to overcome the LRSPP propagation loss and to enable ASE-LRSPP.

The inset in Fig. 2 shows the diffraction-limited ASE intensity distribution at the output facet of a typical structure (time averaged over many pump pulses) as captured by an infrared camera. The apparent intensity reduction over the central region of the image, where the metal stripe is located, is a consequence of the large (small) spontaneous emission rate of SRSPPs (LRSPPs and radiative modes) close to the metal along with the high modal loss of SRSPPs[15].

To assess quantitatively the amplifier's noise performance we conducted measurements of ASE-LRSPP power at the peak wavelength, $\lambda_{\rm ASE} = 876$ nm. Fig. 3 shows measurements of the ASE-LRSPP power captured by the fiber, P_f, as a function of l_a. It can be described by the familiar form[24]

$$P_f = C_{\rm eff} P_N (e^{\gamma l_a} - 1), \qquad (1)$$

where γ is the LRSPP mode power gain coefficient, P_N is the effective input noise power, and $C_{\rm eff} = 0.93$ is the fibre coupling efficiency, whose value was obtained via finite element calculations (supplementary information). Fitting Eq. (1) to the ASE-LRSPP measurements using the non-linear least-squares (NLS) formulation and the Levenberg-Marquardt coefficient minimisation algorithm yields $P_N = 0.37$ μW and $\gamma = 16.9$ cm^{-1}. The inset in Fig. 3 shows the amplifier gain in decibels, $G_a = 10\log(e)\gamma l_a$, as a function of l_a, obtained from measurements of LRSPP stimulated emission using a (practically) monochromatic probe signal tuned to $\lambda_{\rm ASE}$. Following Ref. 15, a mode power gain coefficient of $\gamma = 17.3$ cm^{-1} was obtained by fitting a linear model to the linear amplification region. Note that γ as obtained with both techniques corresponds to the *small-signal* LRSPP gain coefficient; thus, from the good agreement between the two values we conclude that the measured ASE signal is indeed due to spontaneous emission of LRSPPs.

The effective input noise power per unit bandwidth is given by $P_N B_\nu^{-1}$, where $B_\nu = 0.468$ THz is the optical bandwidth of the detected signal (corresponding to B_λ centred at $\lambda_{\rm ASE}$). Using the experimental value for P_N we obtain $P_N B_\nu^{-1} = 7.45 \times 10^{-19}$ W/Hz. This value is 3.3 times larger than the theoretical minimum for a phase-insensitive optical amplifier[25], and is comparable to noise measurements conducted in other nearly optimum optical amplifiers[24,26].

Next we present a simple theoretical model to describe ASE-LRSPP, which captures the essence of the phenomenon and explains the experimental observations. We follow the standard theory for linear photon amplifiers, where the amplifier signal is taken as a uniform photon flux, ϕ, that propagates in a definite direction

obeying the linear differential equation[27]

$$\frac{d}{dz}\phi(z) = \gamma\phi(z) + \xi. \quad (2)$$

Here, z is the propagation direction referenced to the amplifier's input plane, γ is the power gain coefficient, and ξ is the photon spontaneous emission rate per unit volume coupled to the amplifier signal. We adapt this model to the LRSPP amplifier simply by assuming that ϕ represents the flux of LRSPPs propagating along the metal stripe in the $+z$-direction, ξ describes the spontaneous emission rate of LRSPPs per unit volume in this same direction, and γ is the LRSPP mode power gain coefficient.

Solving Eq. (2) with $\phi(0) = 0$ leads to Eq. (1) describing the ASE-LRSPP power in the fibre with

$$P_N = Ah\nu\xi\gamma^{-1}, \quad (3)$$

where h is Planck's constant, ν is the frequency of light at λ_{ASE}, and A is the effective LRSPP mode area. Since the LRSPP transverse field is approximately Gaussian[22] we express $A = \pi w^2$ with $2w$ being the LRSPP e^{-1} mode field diameter. Furthermore, inspired by the treatment of Saleh and Teich for photons[27], we define

$$\xi = Ng(\nu)B_\nu\Gamma F, \quad (4)$$

where N is the effective uniform excited-state molecular density, $g(\nu)$ is the emission lineshape, and the product ΓF represents the average spontaneous emission rate of LRSPPs propagating in the $+z$-direction.

To estimate ΓF we consider for simplicity the one-dimensional variant of the structure in Fig. 1 (infinitely wide metal stripe) and describe the gain medium as a homogeneously distributed ensemble of uncoupled dipoles, which is a valid representation since dimer formations have not been observed at the molecular concentration used in our experiments[28]. Excited dipoles close to the metal may loose energy through different channels. Two of them, internal conversion (IC) and coupling to electron-hole (EH) pairs in the metal, are non-radiative, while the others involve radiative processes such as spontaneous emission of SRSPPs, LRSPPs, and radiative modes (RAD). The decay rate of each channel depends on the dipole position and dipole-moment orientation with respect to the metal surface. Following Ref. 2, we computed these rates assuming isotropically oriented dipoles. The results are shown in Fig. 4 as a function of the y coordinate and normalised to the natural dipole decay rate, $\Gamma_{\mathrm{o}} = \tau_f^{-1}$, with τ_f being the fluorescence lifetime. We observe that excited IR140 molecules decay mainly through non-radiative processes, where the large IC rate is caused by the low molecular quantum efficiency of IR140 (~ 0.05). On the other hand, the radiative processes are dominated by spontaneous emission of SRSPPs (radiative modes) for y values smaller (larger) than ~ 100 nm. Furthermore, we note that the spontaneous emission rate of LRSPPs is smaller than the other rates over most of the dipole positions considered.

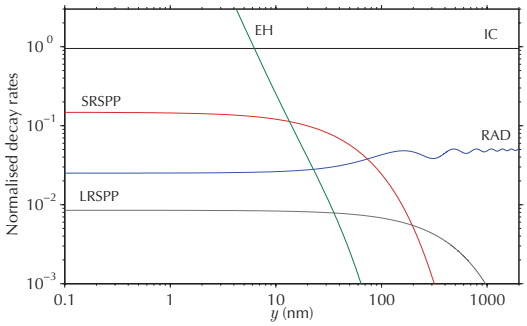

FIG. 4. (Colour online) Normalised excited state decay rates of isotropic dipoles into the different energy decay channels supported by the one-dimensional variant of the structure in Fig. 1.

In our experiments, the dipole orientation is anisotropic in the (x, z)-plane and isotropic in the (x, y)-plane; however, for the purposes of this analysis the dipole orientation can be assumed isotropic because dipoles oriented in the (x, z)-plane do not interact efficiently with the weak LRSPP electric field components in this plane ($E_x \approx 0$ and $E_z \approx 10^{-2}E_y$; Ref. 15). Moreover, the LRSPP field distribution in the case of the metal film is very similar to that of the stripe over its central-width region, where most of the field is concentrated. Therefore, Fig. 4 should provide a fair representation of the LRSPP spontaneous emission in the experimental situation.

The average spontaneous emission rate of LRSPPs in the case of the metal film is obtained as

$$\Gamma = \frac{1}{\delta}\int_0^\infty \Gamma_{\mathrm{LRSPP}}(y)dy, \quad (5)$$

where the normalisation length, δ, is the e^{-1} LRSPP field penetration depth into the gain medium. Γ assumes spontaneous emission of LRSPPs propagating in all directions over the metal plane. The role of F in Eq. (4) is to restrict the in-plane wavevectors of LRSPPs in the film to the range of wavevectors supported by the stripe's LRSPP propagating in the $+z$-direction. Since the transverse LRSPP field profile in the stripe has Gaussian-like distribution along the x-axis[22], one obtains (supplementary information)

$$F \approx \frac{\lambda_{\mathrm{ASE}}}{\pi^2 w n_{\mathrm{eff}}}, \quad (6)$$

where n_{eff} is the LRSPP effective index.

The asymmetric distribution of the gain medium, the pump reflection at the metal surface, and the position-dependent decay rates render the excited-state molecular density a position-dependent quantity. However, the effective uniform value, N, in Eq. (4) can be obtained from the experimental measurement of γ through the relation

$$\gamma = N\sigma_e - \alpha_i, \quad (7)$$

where σ_e is the molecule's emission cross-section at λ_{ASE}, α_i is the intrinsic LRSPP mode power attenuation.

The theoretical ASE-LRSPP curve in Fig. 3 was computed using the set of equations described above. For the calculations we have used $\tau_f = 240$ ps, $\sigma_e = 8 \times 10^{-16}$ cm^2, and a Lorentzian lineshape with FWHM bandwidth of 50 nm as the photophysical parameters of IR140[28]; values of $n_{\text{eff}} = 1.4528$, $2w = 2.5$ μm, and $\delta = 0.9$ μm, as obtained from numerical calculations; and $N = 7.4 \times 10^{16}$ cm^{-3}, obtained from Eq. (7) using measured values $\gamma = 17.3$ cm^{-1} and $\alpha_i = 12.23$ cm^{-1} (we have used the value of γ obtained from the stimulated emission measurements because it is deemed to be more reliable as it led to smaller error bars in the fit). Details on the numerical calculations and measurement of α_i are given in supplementary information.

The theoretical results show good agreement with the experimental data, with $P_N = 0.30$ μW. The slightly higher experimental value ($P_N = 0.37$ μW) could be attributed to bulk ASE coupled to the fibre and/or to the approximations made in our model. On the basis of the present theoretical model, one realises that the amplifier's low noise measured experimentally is due to the low spontaneous emission rate of LRSPPs.

Note that the factor ΓF, as described above, is approximate for the LRSPP mode in question. A more accurate estimate would require computing Γ by integrating the two-dimensional distribution of the LRSPP spontaneous emission rate obtained (for example) following Ref. 29, using the integration area as normalisation constant, and setting $F = 1/2$. On the other hand, the theory described here applies directly to one-dimensional structures and could also be used to model ASE of other supported plasmon modes, such as single-interface SPPs and SRSPPs, by writing Eq. (5) appropriately.

In summary, we have measured low spontaneous emission noise in a LRSPP amplifier consisting of a thin gold stripe on SiO_2 covered with an index matched gain medium in the form of IR140 dye molecules in solution. ASE-LRSPP power measurements yielded an effective input noise power per unit bandwidth of 7.47×10^{-4} fW/Hz, which is close to the theoretical minimum for phase-insensitive optical amplifiers. A theoretical model was proposed to describe ASE-LRSPP, finding good agreement with the experimental results. The model is based on the standard theory of linear photon amplifiers and is adapted to LRSPPs by proper calculations of the LRSPP spontaneous emission rate. The model can also be applied directly to other planar structures supporting plasmon modes.

* [redacted]
† [redacted]

[1] H. Raether, *Surface Plasmons on Smooth and Rough Surfaces and on Gratings.* (Springer, Berlin, 1988)
[2] G. W. Ford and W. H. Weber, Phys. Rep. **113**, 195 (1984)
[3] F. D. Stefani, K. Vasilev, N. Bocchio, N. Stoyanova, and M. Kreiter, Phys Rev. Lett. **94**, 023005 (2005)
[4] K. Okamoto, I. Niki, A. Shvartser, Y. Narukawa, T. Mukai, and A. Scherer, Nature Mater. **3**, 601 (2004)
[5] F. Tam, G. P. Goodrich, B. R. Johnson, and N. J. Halas, Nano Lett. **7**, 496 (2007)
[6] D. J. Bergman and M. I. Stockman, Phys. Rev. Lett. **90**, 027402 (2003)
[7] A. Archambault, F. Marquier, J. J. Greffet, and C. Arnold, Phys. Rev. B. **82**, 035411 (2010)
[8] J. Seidel, S. Grafstrom, and L. Eng, Phys. Rev. Lett. **94**, 177401 (2005)
[9] M. T. Hill, Y.-S. Oei, B. Smalbrugge, Y. Zhu, T. D. Vries, P. J. V. Veldhoven, F. W. M. Van Otten, T. J. Eijkemans, J. P. Turkiewicz, H. D. Waardt, E. J. Geluk, S.-H. Kwon, Y.-H. Lee, R. Notzel, and M. K. Smit, Nature Photon. **1**, 589 (2007)
[10] M. A. Noginov, G. Zhu, M. Mayy, B. A. Ritzo, N. Noginova, and V. A. Podolskiy, Phys. Rev. Lett. **101**, 226806 (2008)
[11] M. Ambati, S. H. Nam, E. Ulin-Avila, D. A. Genov, G. Bartal, and X. Zhang, Nano Lett. **8**, 3998 (2008)
[12] J. Grandidier, G. Colas des Francs, S. Massenot, A. Bouhelier, L. Markey, J.-C. Weeber, C. Finot, and A. Dereux, Nano Lett. **9**, 2935 (2009)
[13] R. F. Oulton, V. J. Sorger, T. Zentgraf, R.-M. Ma, C. Gladden, L. Dai, G. Bartal, and X. Zhang, Nature **461**, 629 (2009)
[14] M. A. Noginov, G. Zhu, A. M. Belgrave, R. Bakker, V. M. Shalaev, E. E. Narimanov, S. Stout, E. Herz, T. Suteewong, and U. Wiesner, Nature **460**, 1110 (2009)
[15] I. De Leon and P. Berini, Nature Photon. **4**, 382 (2010)
[16] M. C. Gather, K. Meerholz, N. Danz, and K. Leosson, Nature Photon. **4**, 457 (2010)
[17] I. P. Radko, M. G. Nielsen, O. Albrektsen, and S. I. Bozhevolnyi, Opt. Express. **18**, 18633 (2010)
[18] I. De Leon and P. Berini, Phys. Rev. B. **78**, 161401 (2008)
[19] P. M. Bolger, W. Dickson, A. V. Krasavin, L. Liebscher, S. G. Hickey, D. V. Skryabin, and A. V. Zayats, Opt. Lett. **35**, 1197 (2010)
[20] P. Berini, Adv. Opt. Photon. **1**, 484 (2009)
[21] G. Winter, S. Wedge, and W. L. Barnes, New J. Phys. **8**, 125 (2006)
[22] P. Berini, R. Charbonneau, N. Lahoud, and G. Mattiussi, J. Appl. Phys. **98**, 043109 (2005)
[23] M. D. McGehee, R. Gupta, S. Veenstra, E. K. Miller, M. A. Diaz-Garcia, and A. J. Heeger, Physical Review B **58**, 7035 (1998)
[24] J. W. Kluver, J. App. Phys. **37** (1966)
[25] A. Yariv, *Quantum Electronics.* (Wiley, New York, 1989)
[26] R. A. Paananen, H. Statz, D. L. Bobroff, and A. Adams, App. Phys. Lett. **4**, 149 (1964)
[27] B. E. A. Saleh and M. C. Teich, *Fundamentals of photonics, 1st. Edition.* (John Wiley & Sons, New York,, 1991)
[28] P. Sperber, W. Spangler, B. Meier, and A. Penzkofer, Opt. Quant. Electron. **20**, 395 (1988)
[29] G. Colas Des Francs, P. Bramant, J. Grandidier, A. Bouhelier, J. C. Weeber, and A. Dereux, Opt. Express **18**, 16327 (2010)

Spontaneous emission in long-range surface plasmon-polariton amplifiers: Supplementary information

Israel De Leon*

School of Information Technology and Engineering, University of Ottawa,

161 Louis Pasteur, Ottawa, Ontario, K1N 6N5, Canada.

Pierre Berini†

School of Information Technology and Engineering, University of Ottawa,

161 Louis Pasteur, Ottawa, Ontario, K1N 6N5, Canada.

Department of Physics, University of Ottawa,

150 Louis Pasteur, Ottawa, Ontario, K1N 6N5, Canada.

Abstract

This document provides supplementary information for the manuscript entitled 'Spontaneous emission in long-range surface plasmon-polariton amplifiers'. It includes a description of the numerical and experimental techniques employed in our analysis, a measurement of the monochromator's optical bandwidth, and a detail description of our approach to define equation (6) in the main text.

I. EXPERIMENTAL TECHNIQUES

A. Measurements of spontaneous and stimulated emission of LRSPPs

Both ASE-LRSPP and LRSPP stimulated emission measurements are obtained for several amplifier lengths (l_a) during the same experimental run. For this, a linearly polarised and substantially monochromatic probe signal is generated with a tuneable Ti:Sapphire laser tuned to the peak ASE-LRSPP wavelength, $\lambda_{\rm ASE} = 876$ nm. The probe signal is coupled to a panda-type polarisation-maintaining (PM) fibre with the electric field aligned along the fibre's slow axis. The probe power in the fibre is measured as ~ -14 dBm. The probe signal is coupled into and out of the LRSPP via butt-coupling using PM fibres of the same type. Both input and output fibres are aligned to the waveguide in position and (TM) polarisation in order to minimise the insertion loss. Once the fibres are aligned, the probe signal is turned off and the structure illuminated by the pump. The signal collected by the output fibre is collimated and passed through a TM polariser and through a monochromator with a full-width-half-maximum (FWHM) optical bandwidth of $B_\lambda = 1.2$ nm centred at $\lambda_{\rm ASE}$ (see Sec. I C). The filtered signal is then focused onto the active area of a calibrated AC-coupled avalanche photodetector (APD) module monitored with a RF oscilloscope.

For each value of l_a two time-resolved power measurements are taken over the 8 ns pump pulse interval using the APD module. The first measurement, taken with the *probe signal on*, corresponds to a measurement of LRSPP stimulated emission plus ASE-LRSPP; the second one, taken with the *probe signal off*, follows approximately 500 ms after the first one and corresponds to a measurement of ASE-LRSPP. The peak-power of these time-resolved measurements are shown in Fig. 1.s as a function of l_a. The probe-off and probe-on measurements are denoted by the crosses and open circles, respectively. The full circles denote measurements of LRSPP probe stimulated emission obtained by subtracting the probe-off measurements to the probe-on measurements.

As mentioned in the main text, the ASE-LRSPP measurements are fitted to Eq. (1) using a non-linear least-squares (NLS) formulation and the Levenberg-Marquardt coefficient minimisation algorithm, with P_N and γ as fitting parameters. The value of γ is also obtained from the LRSPP stimulated emission measurements following the procedure detailed in Ref. 1. A good agreement between the gain coefficients measured with both techniques ensures that the measurements are reliable. In general, we observed that ASE-LRSPP measurements were very sensitive to slight fibre misalignments; however, a good agreement between the gain coefficients obtained with both techniques was observed when the fibres were carefully aligned (as for the case considered in the main text).

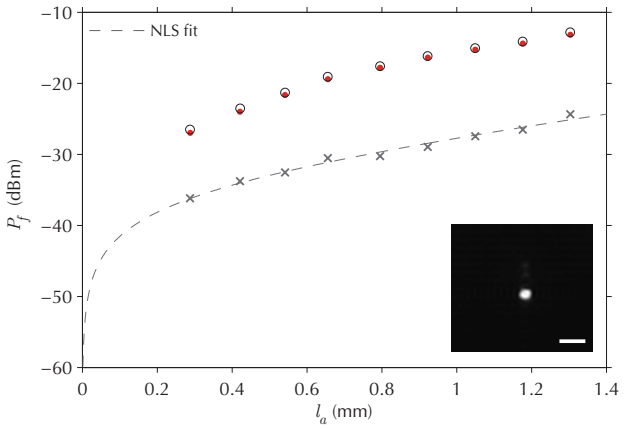

FIG. 1.s. Stimulated emission and ASE measurements: probe-on measurements (open circles), probe-off measurements (crosses), LRSPP probe stimulated emission (full circles) Inset: LRSPP mode intensity distribution at the output facet of the device used for the experimentation as captured by an infra-red camera (scale bar is 10 μm)

B. Passive operation

The passive operation of the waveguide at λ_{ASE} was verified by measuring the intrinsic LRSPP mode power attenuation coefficient employing dye solvent (without molecules) as the upper cladding to exclude additional losses due to ground state absorption of dye molecules. A fibre-to-fibre insertion loss measurement was taken by butt-coupling a probe signal of wavelength λ_{ASE} into and out of the LRSPP of the structure (as described in Sec. I A) and aligning the input and output fibres in order to minimise the insertion loss. A value of $\alpha_i = 12.23$ cm^{-1} was determined from the insertion loss measurement and the coupling efficiency of the LRSPP into the fibre mode, $C_{\mathrm{eff}} = 0.93$, obtained from finite-element analysis (see Sec. II). The measured α_i is slightly larger than that obtained through numerical calculations, 9.03 cm^{-1}. Nonetheless, the LRSPP mode quality was very good (see inset in Fig. 1.s) with most of the input power coupled into the LRSPP mode and virtually no light scattered into the claddings.

C. Monochromator bandwidth

The monochromator bandwidth is measured under similar conditions as those present during the amplified spontaneous emission experiments and with the same detection system. For this, the output of a Ti:Sapphire CW laser (used to probe the LRSPP mode during the stimulated emission measurements) is modulated in amplitude using an acousto-optic modulator to produce pulses with

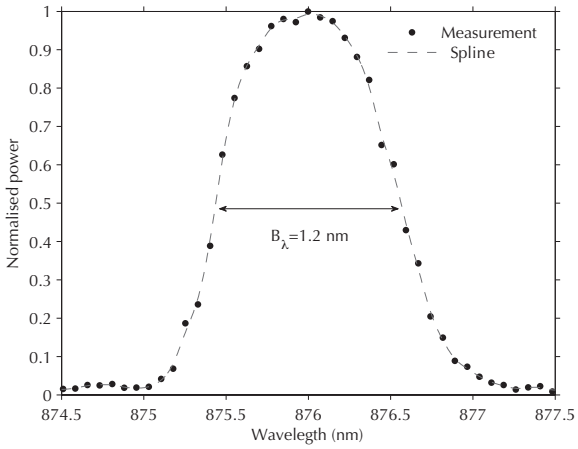

FIG. 2.s. Measurement of the monochromator's bandwidth around λ_{ASE}.

approximately 100 ns in duration, which fall within the bandwidth of the photodetector. The laser wavelength is set to λ_{ASE} and the monochromators central wavelength is scanned over the range $\lambda_{\mathrm{ASE}} \pm 1.5$ nm in steps of 0.08 nm. Fig. 2.s shows the measured peak powers at each wavelength (circles) normalised to the power measured at λ_{ASE}. Spline interpolation (dashed line) is used as a reference to measure the FWHM bandwidth of the monochromator, $B_\lambda = 1.2$ nm.

II. NUMERICAL TECHNIQUES

A commercial finite-element package (Comsol Multiphysics) was used to solve Maxwell's equations in the passive structure (without dye molecules) to obtain the theoretical mode field profile and intrinsic mode power attenuation of the LRSPP, α_i. For our simulations we have used the bulk refractive index of SiO_2 (assumed identical to that of the dye solvent), Si and Au at λ_{ASE} as given in Ref. 2. For Au, the deviations from the bulk refractive index due to the small thickness of the stripe are estimated as[3] $n_{\mathrm{Au},20} = 1.5\ \mathrm{Re}(n_{\mathrm{Au}}) + i0.92\ \mathrm{Im}(n_{\mathrm{Au}})$, where n_{Au} is the bulk refractive index of gold. The simulations yield $\alpha_i = 9.03\mathrm{cm}^{-1}$ and a fairly circular LRSPP field profile, from which a mode field diameter $2w = 2.5$ μm was obtained as the e^{-1} diameter of the y-polarised electric field magnitude distribution, $|E_y(y)|$. A coupling efficiency per facet of $C_{\mathrm{eff}} = 0.93$ was obtained by computing the overlap factor using the transverse spatial distribution of the main transverse electric-field components of the LRSPP and fibre modes[3]. The latter was modelled as Gaussian with a mode field diameter of 6.2 μm, which was measured using a beam profiler. As expected, C_{eff} is very similar to the value of 0.92 obtained from cut-back measurements of similar structures at a slightly different wavelength ($\lambda = 882$ nm; Ref. 1).

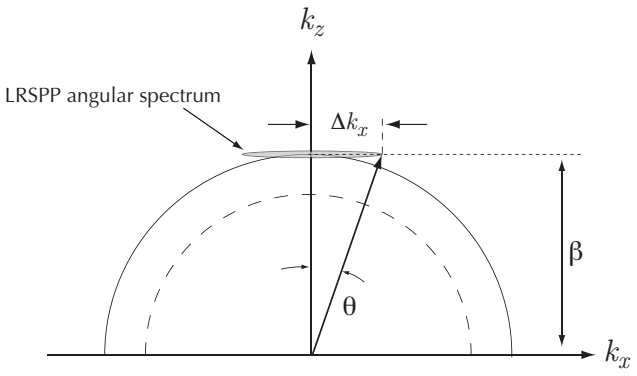

FIG. 3.s. Wavevector components of the LRSPP mode of the stripe. Angular spectrum of the LRSPP mode of the stripe is sketched in the momentum space as the grey ellipse. For reference, the dashed and solid semi-circles denote the allowed wavevectors (with positive k_z component only) for plane-waves in free space and for LRSPPs in the metal film, respectively.

The LRSPP mode in the thin film structure was computed using a multilayer waveguide mode solver[4] employing the same material properties as for the finite width structure. The normalisation length, $\delta = 0.9$ μm, was obtained as the e^{-1} extension of $|E_y(y)|$ (the field penetration depth) into the gain medium.

The normalised decay rates into the different channels supported by the thin metal film were obtained following Ref. 5. The material refractive indices used in our simulations are those mentioned above. To account approximately for electron screening in the metal we consider only dipole field components with in-plane wave vectors $k_{||}$ within the electron-hole excitation continuum of gold at λ_{ASE}; i.e, $k_{||} < (2m_e\omega_e/\hbar + k_F^2)^{1/2} + k_F$, where k_F is the Fermi wave vector, $\hbar$ is the reduced Planck's constant, m_e is the electron mass, ω_e is the angular frequency of light.

III. IN-PLANE WAVEVECTOR COMPONENTS OF THE STRIPE'S LRSPP MODE

In Eq. (4), F represents the ratio of the range of wavevectors supported by the stripe's LRSPP propagating in the $+z$-direction to all possible LRSPP wavevectors in the film. To estimate this quantity we consider Fig. 3.s, which sketches the in-plane components of the LRSPP angular spectrum (in momentum space). For reference, the dashed semi-circle denotes free-space (with positive k_z component only) wavevectors and the solid semi-circle denotes real wavevectors of LRSPPs supported by the metal film, both at the operation frequency $\nu = c/\lambda_{\mathrm{ASE}}$, with c being the speed of light in free space.

The transverse field profile of the stripe's LRSPP has a Gaussian-like distribution along the x-axis[3] (the inset in Fig. 1a in main text shows the reference coordinate system). It follows that, if its field distribution along the x-axis has a e^{-1} width of $2w$, the associated Gaussian angular spectrum along the k_x-axis has a e^{-1} width of $2\Delta k_x = 4/w$ (see Fig. 3.s). Furthermore, since the stripe's LRSPP is guided along the z-axis, its angular spectrum has a unique k_z component denoted by β, the LRSPP's phase propagation constant. Note that the regions of the spectrum falling off the solid semicircle denote evanescent wavevector components. As long as $\beta \gg \Delta k_x$ one can write $F \approx 2\theta/2\pi$, where θ is defined in Fig. 3.s and is given by

$$\theta = \tan\left(\frac{2}{w\beta}\right) \approx \frac{\lambda_{\text{ASE}}}{\pi w n_{\text{eff}}}, \tag{1.s}$$

where n_{eff} is the LRSPP effective index. Thus,

$$F \approx \frac{\lambda_{\text{ASE}}}{\pi^2 w n_{\text{eff}}}. \tag{2.s}$$

The approximation is well-satisfied for the selected waveguide because $\beta \gg 2/w$.

---

* [redacted]

† [redacted]

[1] I. De Leon and P. Berini, "Amplification of long-range surface plasmons by a dipolar gain medium," *Nature Photon.* **4,** 382-387 (2010).

[2] E. D. Palik, *Handbook of Optical Constants of Solids.* (Academic Press, New York, 1985).

[3] P. Berini, R. Charbonneau, N. Lahoud, and G. Mattiussi, "Characterization of long-range surface-plasmon-polariton waveguides," *J. App. Phys.* **98,** 043109 (2005).

[4] C. Chen, P. Berini, D. Feng, S. Tanev and V. P. Tzolov, "Efficient and accurate numerical analysis of multilayer planar optical waveguides in lossy anisotropic media," *Opt. Express.* **7,** 260-272 (2000).

[5] G. W. Ford and W. H. Weber, "Electromagnetic interactions of molecules with metal surfaces," *Phys. Rep.* **113,** 195-287 (1984).

CHAPTER 6

Gain and noise measurements in active long-range SPP waveguides

6.1 Summary

This chapter describes techniques and an experimental setup to measure the gain and noise of SPP amplifiers similar to those described in Chapters 5 and 4. The setup is capable of acquiring absolute power measurements at the amplifier's output over a narrow optical bandwidth. The LRSPP amplifier's gain can be determined independently from two different methods using the data generated in a single experimental run. The first method was described in Chapter 4 and employs stimulated emission measurements of a probe LRSPP signal; the second method was described in Chapter 5 and employs measurements of ASE-LRSPP over a narrow optical bandwidth. The chapter discusses in detail the setup configuration, the calibration and alignment techniques, the mechanical and thermal stability of the setup-amplifier system, and the measurement procedures. It also presents a series of experimental results conducted under similar conditions, from which the repeatability of the experimental setup was assessed. It was noted that small fibre misalignments can impact appreciably the gain measurements obtained through ASE-LRSPP measurements. Also, a poor pump beam quality and inaccurate pump alignment are factors that can limit the system repeatability.

6.2 Contribution

The results provided in this chapter have been accepted for publication in *Review of Scientific Instruments*. I designed and built the experimental setup; I developed the active structure used for the experimentation based on a passive waveguide provided by Dr. Berini; I generated and interpreted the experimental results, and wrote the manuscript. Dr. Berini contributed to the design of the experiments and experimental setup, the interpretation of the results, and revised the manuscript.

6.3 Article

The submitted article follows verbatim.

Measuring gain and noise in active long-range surface plasmon-polariton waveguides

Israel De Leon[1, a)] and Pierre Berini[1, b)]
School of Information Technology and Engineering, University of Ottawa, 161 Louis Pasteur, Ottawa, Ontario, K1N 6N5, Canada.

(Dated: 8 February 2011)

We describe techniques and an experimental setup to measure the gain and noise characteristics of a long-range surface plasmon-polariton amplifier consisting of a symmetric metallic stripe waveguide incorporating optically pumped dye molecules in solution as the gain medium. The setup is capable of acquiring absolute power measurements at the amplifier's output over a narrow optical bandwidth. This allows independent characterisation of the amplifier's gain via measurements of stimulated emission and via measurements amplified spontaneous emission over a narrow optical bandwidth, both obtained during the same experimental run. In addition, the absolute power measurements of amplified spontaneous emission quantify directly the amplifier's noise.

I. INTRODUCTION

A metal-dielectric interface can support transverse-magnetic (TM) polarised optical surface waves called surface plasmon-polaritons[1] (SPPs), which result from the coupling of photons to free electrons at the metal surface. SPPs dissipate power in the metal mainly through electron scattering, resulting in high propagation losses at visible and near-infrared wavelengths. SPPs can exhibit interesting optical properties, such as subwavelength field confinement, high surface sensitivity, and extremely slow group velocity, and have found practical use in a number of scientific and engineering areas[2–6]. However, their scope for application remains limited by large propagation losses. Sufficiently thin metal slabs and stripes (finite width slabs) support low loss SPPs termed long-range SPPs[7] (LRSPPs). Several applications benefiting from the LRSPP's low loss have been demonstrated[8–11]. However, the loss reduction comes at the cost of a weaker field confinement. Optical amplification has been suggested as a means to reduce or even eliminate SPP losses without compromising key attributes[12–18] and recently a number of experimental studies have explored this possibility[19–28].

Different techniques have been employed to measure the mode power attenuation of gain assisted SPPs. For instance, Noginov *et al.*[20] investigated the amplification of SPPs supported by a silver film attached to a glass prism on one side (Kretschmann-Raether configuration) and in contact with an optically-pumped dye-doped polymer on the other side. They estimated the loss reduction by measuring the angle-dependent reflectivity at the metal-glass interface with and without pumping the gain medium and fitting the results to a theoretical model. Grandidier *et al.*[21] measured a reduction in the propagation loss of SPPs supported by a quantum-dot-doped dielectric-loaded plasmonic waveguide via leakage radiation microscopy[29]. This technique estimates the SPP attenuation by fitting an exponential decay function to the SPP intensity distribution measured in the propagation plane through radiation leakage into the substrate. Gather *et al.*[26] measured gain in LRSPPs supported by a thin gold film embedded in an index-symmetric medium incorporating gain on one side of the film in the form of an optically-pumped fluorescent polymer. Their gain measurements were obtained using the variable pump stripe method[30], which consists of pumping the gain medium with a beam shaped in the form of a narrow stripe and measuring the generated amplified spontaneous emission (ASE) intensity as a function of the pump stripe's length. Finally, De Leon and Berini[25] measured gain in LRSPPs supported by a symmetrically cladded thin gold stripe incorporating gain in one cladding in the form of optically-pumped dye molecules in solution. The LRSPP gain was obtained directly from cut-back measurements of LRSPP stimulated emission using a probe signal butt-coupled into and out of the LRSPP via polarisation-maintaining (PM) fibres.

In this paper we describe techniques and an experimental setup to measure the fibre-to-fibre gain, mode power gain coefficient, and noise in a LRSPP amplifier consisting of a thin metallic stripe incorporating a gain medium in the form of optically-pumped dye molecules in solution, which is similar to that investigated in Ref. 25. The technique consists of obtaining absolute power measurements of LRSPP stimulated emission through a (practically) monochromatic probe signal as well as measurements of ASE of LRSPPs (ASE-LRSPP) over a narrow optical bandwidth. The LRSPP mode power gain coefficient is obtained following two approaches from the same set of measurements; one approach is based on measurements of ASE-LRSPP and the other is based on measurements of LRSPP probe stimulated emission. Thus, this work also provides a direct comparison between two measurement modalities reported previously in Refs. 25 and 26. In addition, the absolute ASE-LRSPP measurements allow a direct evaluation of an effective in-

[a)] Electronic mail: [redacted]
[b)] Also Department of Physics, University of Ottawa, 150 Louis Pasteur, Ottawa, Ontario, K1N 6N5, Canada; and Spectalis Corp., P.O. Box 72029, Kanata North RPO, Ottawa, ON, K2K 2P4, Canada. Electronic mail: [redacted]

put noise power, which characterises the amplifier's noise.

The remainder of this paper is organised as follows. Section II describes the active plasmonic structure used for the experimentation; section III details the experimental setup, system calibration and alignment, system stability, and measurement procedure; section IV describes the approach to determine experimentally the fibre-to-fibre gain, the LRSPP mode power gain coefficient, and the amplifier's noise; section V discusses how the system performance is affected by pump and fibre misalignments; and finally section VI summarises our work and provides concluding remarks.

II. PLASMONIC STRUCTURE

The structure used for the experimentation was built upon a LRSPP waveguide obtained from wafer X023506.15 as reported in Ref. 31. A front cross-sectional view of the plasmonic structure (PS) is sketched in Fig. 1a. It consist of a 20 nm-thick and 1 μm-wide gold stripe on a 15 μm-thick SiO_2 layer thermally grown on a Si substrate. The stripe is covered by a gain medium in the form of optically pumped IR140 dye molecules (Sigma Aldrich) in solution and a ~ 150 μm-thick glass slide lies on top of the dye holding it to within a ~ 90 μm-thick layer. Fig. 1b shows the PS from the top. The waveguide's total length is $l = 1.45$ mm. Dye molecules are pumped by a linearly polarised laser beam shaped as a narrow stripe that impinges at normal incidence onto the top of the structure with its electric field aligned along the waveguide's longitudinal axis (z-axis). The pump beam illuminates the end region of the waveguide over a length l_a, which defines the amplifier section.

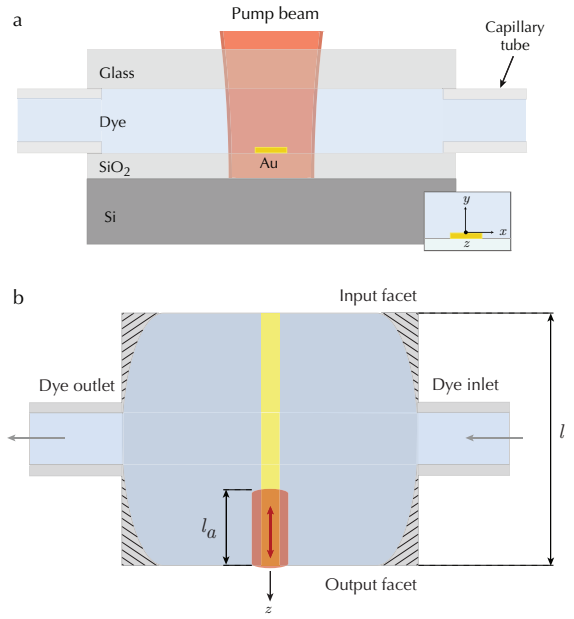

FIG. 1. Adapted from Ref. 32. (a) Front cross-sectional view of the plasmonic structure considered for the experimentation (not to scale). The inset shows the coordinate system with the $+z$-axis coming out of the page. (b) Top view. The lengths of the waveguide and the amplifier section are l and l_a, respectively. The pump polarization is indicated by the arrow.

The dye concentration is 0.5 mM, corresponding to a molecular density of 3×10^{17} cm^{-3} and the solvent is a mixture of 30.4% ethylene glycol and 69.6% dimethyl sulfoxide. The dye is pumped at a wavelength $\lambda_p = 810$ nm, close to the peak absorption wavelength, and LRSPP amplification is analysed at $\lambda_e = 876$ nm, which corresponds to the peak ASE-LRSPP wavelength[32]. At a temperature of 23° C, the dye solution is index matched to SiO_2 at λ_e, forming a symmetric waveguiding structure supporting purely bound LRSPPs.

The PS incorporates SiO_2 capillary tubes at opposite ends (see Fig. 1b) for use as an inlet and outlet for the dye solution. They are built onto the SiO_2/Si structure using optical-grade UV-curable epoxy (Norland Products Inc., NOA61). The shaded regions in Fig. 1b indicate the places where the epoxy is cured to keep the inlet/outlet and the cover glass-slide in place. Note that the input and output optical facets are open to ensure a homogeneous medium along the full optical path. A syringe pump is used to inject the dye into the PS at a rate of 1 μL/min. The dye fills the region below the cover glass covering the gold stripe in full length and flows through by capillary action until it reaches the outlet were it is collected and then wasted.

III. SETUP

A. Block diagram

A block diagram of the experimental setup is shown in Fig. 2. The broken and solid lines in the diagram indicate free-space and fibre-guided light propagation, respectively. Three main branches are identified in the figure: the *pump branch* that delivers the pump light to the PS, the *input branch* that delivers the probe signal to the PS, and the *output branch* collects and delivers the PS's output signal to the detection instruments. All the optical fibres employed in the setup are panda-type PM fibres (Thorlabs Mod. PM780-HP) and the guided light has its electric field vector oriented along the fibre's slow axis.

The beam in the pump branch is generated with a tuneable dye laser pumped by a pulsed frequency-doubled Nd:YAG laser (Spectra-Physics, Mod. Quanta-Ray Lab10 / Sirah Mod. Cobra-Stretch). The dye laser is tuned to λ_p; it provides pulses of duration ~ 8 nm full-width-half-maximum (FWHM) and a repetition rate of 10 Hz. The pump energy and polarisation are controlled with a $\lambda/2$ wave plate (WP1) followed by a Glan-Laser polariser (PBS1). A solid metallic plate attached to an electro-mechanical actuator (SW1) is used to blank the pump signal as needed. A cylindrical lens (L2) with focal length of 50 mm is used to shape the beam into a narrow

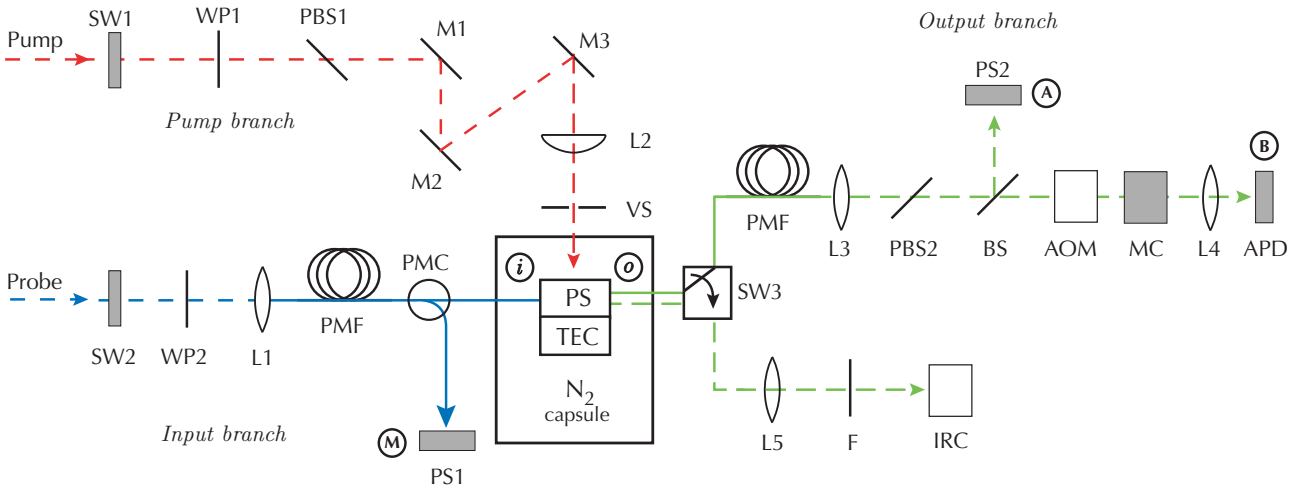

FIG. 2. Experimental setup configuration. Broken paths: Free-space beam; solid paths: fibre guided. AOM: Acousto-optic modulator; APD: avalanche photodetector; BS: 10 dB beam splitter; F: long-pass filter; IRC: infrared camera; L1, L3, L4 and L5: microscope objective lenses; L2: cylindrical lens; M1, M2, and M3: silver mirrors; MC: monochromator; PBS1 and PBS2: polarisation beam splitters; PMC: polarisation maintaining coupler; PMF: polarisation maintaining fibre; PS: plasmonic structure; PS1 and PS2: CW low-power sensors; SW1 and SW2: beam bankers; SW3: fibre-coupling/free-space-coupling selection switch; TEC: thermo-electric cooler; VS: variable slit; WP1 and WP2: $\lambda/2$ wave-plates.

stripe, as shown in Fig. 1b. L2 provides a depth of focus of ~ 1 mm and a beam waist of ~ 10 μm, and is placed slightly out of focus to achieve a width of ~ 150 μm at the surface of the PS. The maximum length of the pump stripe is ~ 3.5 mm and it is adjusted during the experiments using a micrometer driven single-blade variable slit (VS) located between L2 and the PS. Mirrors M1, M2, and M3 are used to align the pump beam so it impinges normally onto the top of the structure. M3, L2, and VS are mounted on a two-axis stage (not shown) controlled with micro-positioners to adjust the pump beam position in the (x, z)-plane relative to the PS.

In the input branch, a linearly polarised probe beam is generated with a tuneable continuous-wave (CW) Ti:Sapphire laser (Spectra-Physics, Mod. 3900-CW) tuned to λ_e. The laser light is coupled into a PM fibre using a 40× microscope objective (L1). The probe's electric field vector is aligned along the fibre's slow-axis using a $\lambda/2$ wave plate (WP2). The guided light is then passed through a 10 dB PM fibre coupler (PMC) with its through port connected to a fibre patch-cord with a cleaved end, henceforth referred to as the *input fibre*, which delivers the signal to the PS. The coupler's coupled port is connected to a low-power sensor (PS1), which allows real-time monitoring of the power delivered by the input fibre. A solid metallic plate attached to an electromechanical actuator (SW2) is used to blank the probe signal as needed.

In the output branch, a customised switching fixture (SW3) allows the selection of one of two paths for signal analysis. The bottom path (see Fig. 2) images the light emitted from the PS's output facet onto a vidicon-type infrared camera (IRC; Electrophysics, Mod. MicronViewer 7290) using a 25× microscope objective with long working-distance (L5). A long-pass filter (F) with a cut-on wavelength of 850 nm is used to block the pump light. The top path couples the LRSPP emerging from the waveguide to a cleaved PM fibre, henceforth referred to as the *output fibre*. Using a 6.3× microscope objective (L3), the light exiting the output fibre is focused onto the input of a monochromator (MC; Oriel, Mod. Cornerstone-130) that provides spectral filtering with a FWHM bandwidth of $B_\lambda = 1.2$ nm. Prior to reaching the monochromator, the signal is passed through a TM polariser (PBS2) to remove residual TE light and then is sampled by a 10 dB beam splitter (BS) to monitor its power using the low-power sensor (PS2). An acousto-optic modulator (AOM; Gooch & Housego, Mod. 23080) placed between BS and MC is used only for alignment purposes. Its zeroth diffraction order is aligned with the optical path such that light is deflected only when a modulation signal is provided. The signal exiting the monochromator is focused onto a calibrated AC-coupled avalanche photodiode module (APD; Hammamatsu, Mod. C5658) using a 6.3× microscope objective (L4). The APD is monitored with an RF oscilloscope (Tektronix, Mod. TDS540A; not shown) which in turn is synchronised to the 10 Hz pump signal.

SW3 consists of a brass mount machined to hold on one side a fibre chuck (holding the output fibre) and on the other a microscope objective (L5); the brass mount slides on a magnetic base mounted on a micro-positioning stage enabling to switch between the two output paths with minimum realignment.

Both the PS1 and PS2 power sensors (Newport, Mod. 918D-SL) are connected to a dual channel power meter (Newport, Mod. 2930C) with low-pass electrical bandwidth cutting off at 5 Hz. Thus, these sensors detect

only the CW component of the (possibly pulsed) optical signal. Both input and output fibres are mounted on five-axis micro-positioners. The elements depicted as grey boxes in Fig. 2 are controlled and/or monitored by a computer.

B. System calibration

Calibration of the input and top-output branches is required to perform absolute measurements of gain and noise. In Fig. 2, the locations marked by circled letters indicate the calibration reference planes. In what follows, each letter is used as a subindex to denote the power at the respective location. Thus, P_i is the power emerging from input fibre; P_o is the power captured by the output fibre; $P_{\rm A}$ is the power measured by PS2; $P_{\rm B}$ is the power reaching the APD; and $P_{\rm M}$ is the input-power monitor as measured by PS1. In particular, it is necessary to measure the losses of the optical paths oA and oB, as well as the power relation between M and i. All the calibration measurements are taken with the AOM turned off (no modulation signal provided) and with the probe and monochromator central wavelengths set to λ_e.

Prior to calibration all polarisations are aligned (WP1, PBS2, input and output fibres) to each other. For this, the probe signal is injected into the output branch by (end-fire) coupling the input and output fibres with index matching fluid between them. Then, with PBS2 set to pass TM light, the slow axes of both fibres are aligned to maximise $P_{\rm A}$. Typically, for a good alignment, a polarisation extinction ratio of ~ 30 dB was obtained.

The calibration procedure consists of three differential power measurements (in dB). First, the relation between the input-power monitor and the input power, $\Delta_{i\rm M} = P_i - P_{\rm M}$, is obtained by measuring simultaneously the power at M and i using PS2 at i. To obtain the loss of the oA path, the probe signal is injected into the output branch by end-fire coupling the input and output fibres with index matching fluid between them, and the fibres are aligned to maximise $P_{\rm A}$. Then, the powers at M and A are measured simultaneously to obtain $\Delta_{\rm AM} = P_{\rm A} - P_{\rm M}$; the oA path loss is then calculated as $\Delta_{o\rm A} = \Delta_{i\rm M} - \Delta_{\rm AM}$. Finally, with the input and output fibres still aligned, the powers at A and B are measured simultaneously using PS1 at B (instead of the APD) to obtain $\Delta_{\rm BA} = P_{\rm B} - P_{\rm A}$; the oB path loss is then calculated as $\Delta_{o\rm B} = \Delta_{o\rm A} - \Delta_{\rm BA}$. The calibration values obtained at λ_e are $\Delta_{i\rm M} = 8.48$ dB, $\Delta_{o\rm A} = 12.39$ dB, and $\Delta_{o\rm B} = 8.39$ dB. The APD responsivity at λ_e was measured separately as 3.94×10^4 V/W by applying a modulated optical signal with known peak power and pulse duration of ~ 100 ns, which is well within the APD's electrical bandwidth.

At the end of the calibration procedure the detectors are returned to their respective locations as indicated in Fig. 2. All of the elements remain aligned except the APD. To align the APD, the probe signal is injected into the top-output branch and a modulation signal is provided to the AOM such that a pulsed probe signal with pulse duration ~ 100 ns is generated at location B. The APD, mounted on a 3-axis micro-positioning stage, is aligned to the probe beam to maximise the output voltage signal. Finally, the power measured by the APD is related to that measured at location A through $P_{\rm B} = P_{\rm A} + \Delta_{\rm BA}$. For a good alignment these two values agree to within 5%.

C. Probe coupling and stability

Since the waveguide is very sensitive to asymmetry in the index of refraction above and below the metal, it is imperative to control and stabilise the dye solution. The dye solvent is hygroscopic; a humid environment thus results in a fast reduction of its refractive index due to water absorption. To provide a dry environment, the PS is enclosed in a 20 $\rm cm^3$ acrylic capsule filled with N_2 flowing at a rate of 1 SCFH. The dye flow, set always to 1 μL/min, is required to eliminate problems related to refractive index and ground state absorption changes due to photochemical modifications in the dye molecules caused by the probe and/or pump radiation. Also, it is crucial to fine-tune the refractive index of the dye solution such that it matches precisely that of the SiO_2 lower cladding. Thus, the PS is attached to a thermoelectric cooler (TEC) using a thermally conductive ad-

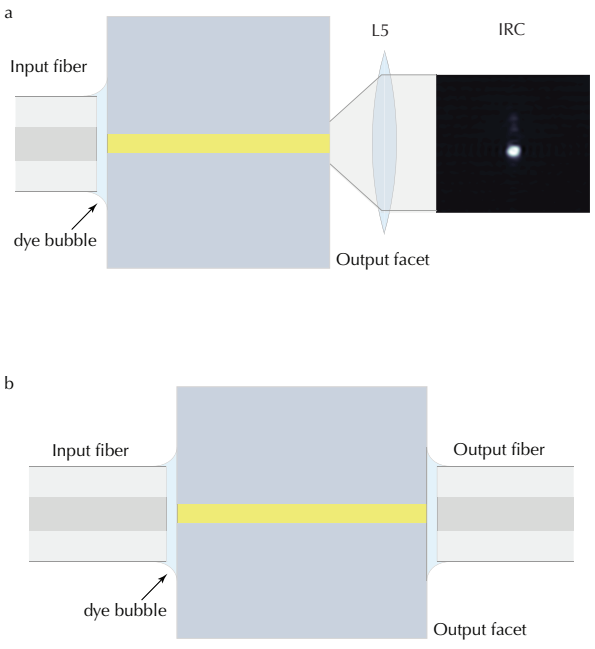

FIG. 3. Top view of plasmonic structure illustrating (a) end-fire coupling of probe light into the LRSPP using optical fibre and lens and (b) end-fire coupling to the LRSPP using two optical fibres. The image on the far right of (a) shows the LRSPP mode intensity profile at the output facet as captured by the infrared camera.

hesive, which in turn is mounted on a one-axis micro-positioning stage with movement along the x-axis. The thermal operating point is determined by inspecting the LRSPP mode at the waveguide's output under high magnification (using the bottom-output branch in Fig. 2) and adjusting the temperature until the most symmetric mode pattern is achieved and no signs of radiation into the claddings are visible. For this, the probe signal is end-fire coupled into the LRSPP via the input fibre and the mode at the output is inspected under high magnification using the infrared camera, as illustrated in Fig. 3a. The input fibre is aligned to the waveguide in position and (TM) polarisation in order to maximise the coupling efficiency, indicated by a maximum intensity in the output mode pattern. The operating temperature must be stable in order to avoid refractive index fluctuations due to thermo-optic effects. Thus, a feedback loop signal is provided to the temperature controller using a thermistor mounted on the TEC surface. A temperature of 23° C at the TEC surface was required to achieve index symmetry at λ_e. The image on the far right on Fig. 3a shows the LRSPP mode intensity profile as captured by the infrared camera after the input fibre has been properly aligned and the other experimental parameters have been adjusted. Clearly, most of the probe light is coupled into the LRSPP with virtually no light scattered into the claddings.

Once the input-fibre has been aligned and the temperature, dye flow, and nitrogen flow have been adjusted to ensure the proper passive performance of the device, the LRSPP is coupled out of the structure via end-fire coupling using the output fibre as illustrated in Fig. 3b. When coupling to fibres, a small gap filled with dye solution is always left between the fibre and the PS to avoid damaging the facets. The output fibre is aligned to the waveguide by minimising the insertion loss as measured between points M and A. Since PBS2 is in the optical path, the insertion loss is minimised when the the fibre is well aligned to the waveguide and its slow-axis is oriented along the LRSPP electric field.

Fig. 4 shows an insertion loss measurement at λ_e conducted over time on the PS with dye solvent (without dye molecules) as the upper cladding. In this case, the temperature was set to 21.5° C because of the slightly lower refractive index of the solvent relative to that of the dye solution. The other experimental parameters, (dye and nitrogen flow rates) are set to those mentioned above. The mean trend (best linear fit) is indicated by the dashed line. The variation in the mean insertion loss is attributed to input and output fibre misalignments caused by a mechanical drift in the micro-positioning stages. On the other hand, the variations about the mean trend are due to polarisation fluctuations in the probe signal. We observe that the measurement is very stable, with mean variation of only ~ 0.05 dB over a period of 30 minutes. Since a typical experimental run is completed in approximately 4 minutes, we conclude the experimental setup provides very good mechanical and environmental stability.

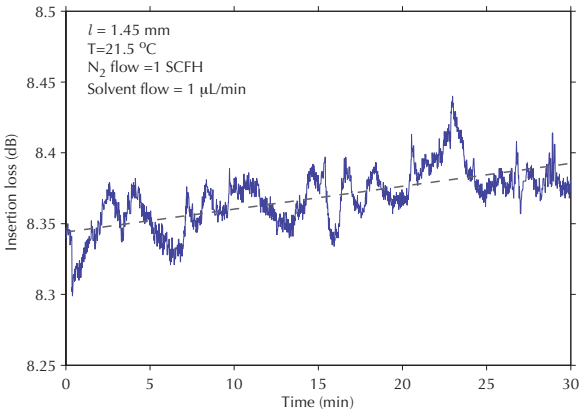

FIG. 4. Stability of insertion loss measurement conducted on the plasmonic structure under consideration using dye solvent (without dye molecules) as upper cladding.

The measured value of insertion loss, ~ 8.35 dB, includes the LRSPP propagation loss and fibre coupling losses at both input and output facets. The measured insertion loss is slightly higher than the theoretical expectation of 5.8 dB, obtained through finite element calculations. Despite this discrepancy, Fig. 3a shows that the quality of the LRSPP mode profile is very good with most of the power coupled into the LRSPP and practically no radiation scattered into the background.

D. Pump alignment and homogeneity

A preliminary alignment of the pump incidence angle is done without L2 and with VS completely open by placing a thin mirror on the PS and aligning the incident pump beam such that its reflection is collinear. Then L2 is placed in the optical path and aligned manually such that the generated pump stripe is centred roughly in the same place as without L2. The mirror is then removed and the pump beam is aligned to illuminate the end region of the waveguide (as illustrated in Fig. 1b) by adjusting the position of M3, L2 and VS in the (x, z)-plane. The alignment procedure is as follows: the output fibre is aligned to the waveguide and photographic paper is placed flat over the PS. Then, the pump stripe is set to illuminate the PS at a length of $l_a \approx 2$ mm. By examining the beam burn on the photographic paper under high magnification (through a long-working-distance microscope; not shown), the pump stripe position in the x-direction is adjusted until the beam burn is perfectly aligned with the output fibre (and thus the metal stripe). The same process is repeated for the alignment in the z-direction, making sure that the edge of the pump stripe coincides with the tip of the output fibre.

The intensity distribution of the pump stripe in the (x, y)-plane was assessed qualitatively by observing the ASE intensity distribution generated at the PS output. After the pump beam has been aligned to the waveguide,

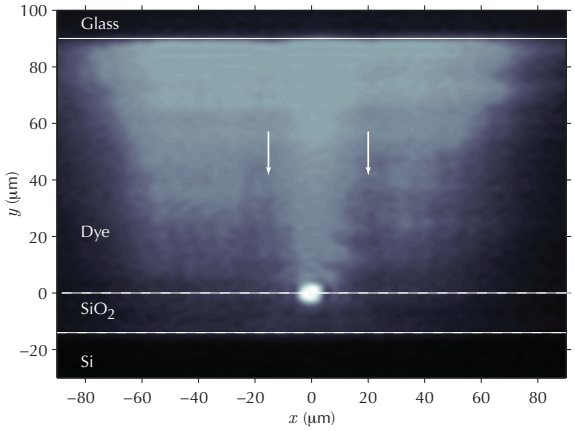

FIG. 5. Time averaged intensity distribution at the plasmonic structure's output facet while being pumped as captured by the infrared camera.

a probe signal is coupled into the LRSPP and the mode intensity at the output facet is imaged on the infrared camera (see Sect. III C). The PS is then pumped at full length ($l_a = l$) using the same pump wavelength and pulse energy as for the amplification experiments. During this process, fine-tuning of the pump stripe position along the x-axis is achieved by shifting the PS using a micro-positioner until the ASE intensity distribution is best aligned with the LRSPP mode. The camera records images during a long time interval capturing the ASE and LRSPP intensities over many pump pulses at a frame rate of 50 Hz. An image corresponding to a video frame that captured strong ASE intensity is selected for analysis and shown as Fig. 5. The ambient light intensity is removed from the image by subtracting from every pixel the grey-scale value of the bottom-right pixel in the Si layer. Since Si absorbs efficiently over the emission spectrum of the dye, the subtracted value does not affect the ASE level. As expected, the ASE exhibits the maximum intensity close to the dye-glass interface because the pump energy is absorbed as it penetrates into the dye. Moreover, the image reveals that the intensity distribution along the x-axis is not uniform but it shows two regions of low intensity indicated by the arrows in Fig. 5. This was caused by a poor quality in the pump beam profile along the x-axis, which in turn was caused by diffraction effects within the dye laser itself.

Although inconvenient, the pump inhomogeneity along the x-axis is not a limitation for the gain measurements. On the other hand, homogeneous pump illumination over the z-axis is required such that a constant gain per unit length is generated along the length of the waveguide. Measurements of the pump stripe intensity homogeneity along this axis were performed prior to mounting the PS. For these measurements, a broadband thermopile optical power sensor (Newport, Mod. 818P-001-12) replaces the PS and the pump power is measured as a function of the stripe length (l_a) over the central region of the beam covering the range $0.3 \leq l_a \leq 2.54$ mm. The measurements indicate a maximum variance of 5% in the pump intensity over this length.

E. Measurement procedure

Prior to conducting the gain and noise measurements the setup is calibrated and aligned (Sec. III B), the pump beam is aligned (Sec. III D), and the PS to be tested is prepared (Sec. III C). The latter step includes coupling the input probe signal into the LRSPP, routing the PS output to the top output branch (see Fig. 3b), and ensuring stability of the system. Furthermore, the AOM modulation signal is turned off, the probe and monochromator central wavelengths are set to λ_e, the pump wavelength is set to λ_p, and the VS is adjusted to the initial amplifier length ($l_a = 0.2$ mm).

The measurement procedure consists of five steps: (*1*) the pump signal is turned on; (*2*) the probe signal is turned on and a measurement of amplified probe signal resolved in time over the pump pulse interval is taken with the APD module and the oscilloscope averaging over seven seconds; (*3*) immediately after (*2*) the probe signal is turned off and a measurement of ASE-LRSPP resolved in time over the pump pulse interval is taken with the APD module and the oscilloscope averaging also over seven seconds; (*4*) while averaging measurements in steps (*2*) and (*3*), P_i and the CW component of P_o are measured *in situ* by PS1 and PS2 and the passive insertion loss is calculated (since the pump duty cycle is very small, the CW component of P_o is just the power in the absence of the pump); and (*5*) steps (*2*)-(*4*) are repeated for incremental values of l_a in the range $0.2 < l_a < 1.37$ mm. Steps (*1*)-(*4*) are performed automatically by a computer through a LabView-based instrumentation control code developed in house.

IV. RESULTS AND DISCUSSION

The measurements given in this section are taken with a probe input power $P_i = 41$ μW (-13.9 dBm) and with a pump pulse energy $E_p \approx 10$ mJ/cm^2. The measurements follow the procedure described in Section III E. The methods for obtaining the amplifier's fibre-to-fibre gain, LRSPP mode power gain, and amplifier's noise have already been described in Refs. 25 and 32 but they are also discussed here for completeness.

A. Fibre-to-fibre gain

Fig. 6a shows experimental measurements of P_o resolved in time over the pump pulse interval obtained for several amplifier lengths, l_a. The curves on the right and left result from measurements with the probe signal turned on and off, respectively. The amplifier's noise is due to ASE-LRSPP and corresponds to the probe-off measurements, while the probe-on measurements in-

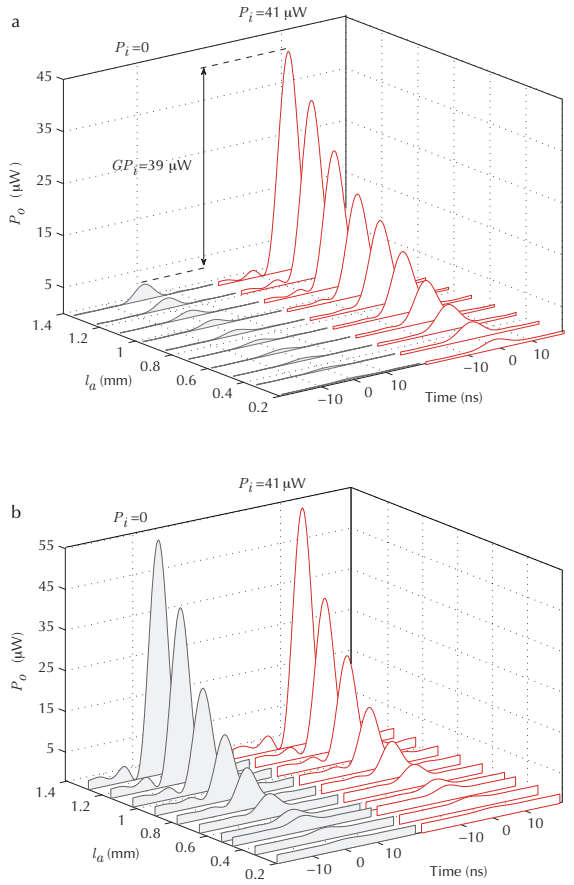

FIG. 6. Probe on (curves on right) and probe off (curves on left) measurements conducted on the plasmonic structure under consideration for cases (a) where the probe signal is coupled into and out of the LRSPP as shown in Fig. 3b, and (b) where the waveguide is shifted ~ 5 μm along the x-axis keeping the fibres and the pump with the original alignment.

clude the probe stimulated emission plus the noise. As expected, both measurements are characterised by an exponential growth as l_a increases.

The fibre-to-fibre gain of the active PS is obtained by relating the powers at the input and output fibres considering only the stimulated emission of the probe signal. Thus, if the noise power is denoted by η, the fibre-to-fibre gain during the pump interval is

$$G = \frac{P_o - \eta}{P_i}. \tag{1}$$

The quantity GP_i for a particular value of l_a is obtained from the measurements as the absolute difference between the peak values of the two curves. For the longest amplifier length considered in this experiment we obtained $GP_i = 39$ μW (see Fig. 6a). Thus, from the known input power, P_i (measured *in situ* during the experiments) the fibre-to-fibre gain is calculated as $G = 0.951$; or expressed in decibels, $G_{\rm dB} = -0.217$ dB.

To confirm that the measured gain is solely due to stimulated emission of LRSPPs, the experiment was repeated with the LRSPP waveguide shifted ~ 5 μm along the x-axis and leaving the input and output fibres and the pump beam with the original alignment. In this configuration, the probe signal is slab-guided in the region between the glass cover and the Si substrate and amplified before it is captured by the output fibre. Fig. 6b presents the experimental results in the same format as in Fig. 6a. These measurements are practically identical regardless of whether the probe signal is on or off, indicating that the power captured by the output fibre is that generated by *background* ASE only ($GP_i = 0$). This is not surprising given the low coupling efficiency expected between the fibre's fundamental mode and the modes of the large slab waveguide. With these results we conclude that the fibre-to-fibre gain obtained from the measurements in Fig. 6a is the result of LRSPP stimulated emission only.

B. LRSPP mode power gain

Once the fibre-to-fibre gain has been obtained, the gain of the amplifier section (in dB) can be calculated as

$$G_a = G_{\rm dB} + A + 2C_f, \tag{2}$$

where $A = 10\log_{10}(e)\alpha_u(l - l_a)$ is the LRSPP loss in the unpumped region, with α_u being the associated LRSPP mode power attenuation coefficient; and $C_f = -10\log_{10}(C_{\rm eff})$ is the coupling loss per facet, with $C_{\rm eff}$ being the coupling efficiency of the LRSPP to the fibre's mode. $C_{\rm eff}$ was obtained by numerically computing the overlap between the LRSPP mode and the fundamental mode of the fibre; the former was computed through finite element calculations and the latter was modelled as Gaussian with e^{-1} mode field diameter of 6.2 μm, which was measured on the input fibre using a beam profiler. The calculations yield a value of $C_{\rm eff} = 0.93$ ($C_f = 0.315$ dB), which is comparable to the value of 0.92 (0.36 dB) measured via cutback on similar waveguides at a slightly longer wavelength, ($\lambda = 882$ nm; Ref. 25). The value of α_u was obtained from the insertion loss measurements taken *in situ* during the experiment and using C_f as given above.

In analogy to the gain of a photonic amplifier, the expression for G_a including mode gain saturation is[33]

$$G_a(l_a) = 10\log_{10}(e)\frac{\gamma_{\rm SEM} l_a}{1 + S(l_a)}, \tag{3}$$

where $\gamma_{\rm SEM}$ is the small-signal LRSPP mode power gain coefficient (the subscript SEM emphasises that the coefficient is obtained through measurements of probe stimulated emission); and $S(l_a) = P_{\rm LRSPP}(l_a)/P_{\rm sat}$ is the gain saturation factor, with $P_{\rm LRSPP}(l_a)$ being the LRSPP power at $z = l_a$ and $P_{\rm sat}$ being the saturation power. S increases with l_a due to LRSPP amplification causing a reduction of G_a.

Fig. 7a shows G_a corresponding to the fibre-to-fibre gain measurements shown in Fig. 6a as obtained through

Eq. (2). One can identify a linear amplification region for $l_a < 0.6$ mm. On the other hand, for $l_a > 0.7$ mm the amplification is not linear; rather, it decreases with increasing l_a. This is believed to be caused by mode gain saturation. In the linear regime (i.e.; $S \ll 1$), G_a is given by

$$G_a(l_a) \approx 10\log_{10}(e)\gamma_{\mathrm{SEM}} l_a. \tag{4}$$

Thus, γ_{SEM} can be obtained as the slope of a linear model fitted to the linear region of G_a divided by $10\log_{10}(e)$. For the measurements in Fig. 7a, a value of $\gamma_{\mathrm{SEM}} = 16.10$ cm^{-1} was obtained from the linear fit indicated by the dashed line. A large LRSPP mode power gain was achieved despite the fact that fibre-to-fibre gain was not achieved (Fig. 6). This is because the latter also includes losses caused by the unpumped region and fibre coupling. The linear fit predicts a value of -0.15 dB for $l_a = 0$. This slight deviation from the expected value of zero is comparable to the experimental error of ± 0.12 dB.

An alternative approach to obtain the LRSPP mode power gain coefficient is fitting the ASE-LRSPP measurements to the expression describing the power in dBm captured by the fibre

$$P_o = 10\log_{10}\left\{C_{\mathrm{eff}} P_N \left(e^{\gamma_{\mathrm{ASE}} l_a} - 1\right)\right\}, \tag{5}$$

where γ_{ASE} denotes the small-signal LRSPP mode power gain coefficient (the subscript ASE emphasises that the coefficient is obtained through ASE-LRSPP measurements) and P_N is the effective input noise power expressed in milliwatts. Fig. 7b shows the ASE-LRSPP measurements in dBm corresponding to those in Fig. 6a. The fit to Eq. (5) is shown as a dashed line. It was calculated using a non-linear least-squares (NLS) formulation and the Levenberg-Marquardt coefficient minimisation algorithm with γ_{ASE} and P_N as fitting parameters. Using this method, we obtained $\gamma_{\mathrm{ASE}} = 13.67$ cm^{-1}, which is in fair agreement with the value obtained through the stimulated emission measurements.

The inset in Fig. 7b shows absolute measurements of P_o obtained with the probe signal turned off and the PS pumped at full length ($l_a = l$) while scanning the monochromator in the range $870 \leq \lambda \leq 890$ nm. These measurements correspond to the ASE-LRSPP spectrum, which peaks at $\lambda = 876$ nm having a FWHM spectral linewidth of 8 nm. The measured linewidth is considerably narrower than the value of 35 nm measured for $l_a = 0.4$ mm (not shown) using the same pump energy density. This confirmed the presence of ASE-LRSPP, as spectral linewidth narrowing with increasing amplifier lengths and fixed pump energy is characteristic of ASE[34].

C. Noise

An important quantity that characterises the noise of an optical amplifier is the effective input noise power per unit bandwidth, $P_N B_\nu^{-1}$, where $B_\nu = 0.468$ THz is the optical bandwidth of the detected signal and is obtained from B_λ (the monochromator's bandwidth) centred at λ_e. For a high gain amplifier, this quantity represents the power spectral density at the input of the amplifier that generates an output signal with a signal to noise ratio equal to 1. From the NLS fit to the data in Fig. 7b we obtained $P_N = 4.568 \times 10^{-4}$ mW, which results in $P_N B_\nu^{-1} = 9.762 \times 10^{-19}$ W/Hz.

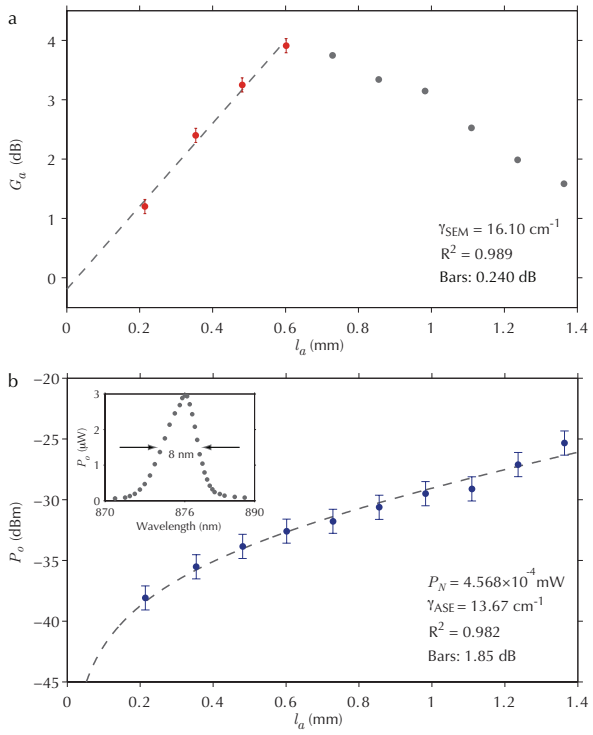

FIG. 7. The LRSPP mode power gain coefficient as calculated from (a) LRSPP probe stimulated emission measurements, and from (b) the ASE-LRSPP measurements. The goodness of each fit as given by the Pearson product-moment correlation coefficient, R^2, is indicated. For both cases, amplitude of the error bars corresponds to two times the mean squared error of the fit. Inset: Absolute power measurement of the ASE-LRSPP spectrum obtained with $l_a = l$; its peak is located at $\lambda = 876$ nm and exhibits a FWHM spectral linewidth of 8 nm.

V. ALIGNMENT SENSITIVITY

Fig. 8 summarises the results of eight experiments conducted consecutively under similar conditions and on the same sample over the course of three days (1,2,3: day one; 4,5: day two; 6,7,8: day three). The input and output fibres and the pump beam were realigned for each experiment following the procedures described in Sections III C and III D, respectively. The ASE-LRSPP and probe stimulated emission measurements associated with experiments 1, 2, 7, and 8 are given in the Appendix. The top panel in Fig. 8 shows the mode power gain coefficients obtained via LRSPP probe stimulated emission,

γ_{SEM} (solid circles), and via ASE-LRSPP, γ_{ASE} (open circles), following the experimental protocol described above. The central panel shows the difference between these two measurements, $\Delta\gamma = \gamma_{\mathrm{SEM}} - \gamma_{\mathrm{ASE}}$. Finally, the bottom panel shows the PS insertion loss measured *in situ* during each experiment; the dashed line corresponds to the insertion loss measured prior to the gain experiments and is taken as the reference.

The results on the top panel of Fig. 8 show that experiments 3,4, and 5 yielded measured values of γ_{SEM} that varied significantly from the average value obtained in the other cases, which is around ~ 19 cm^{-1}. This is attributed to misalignments in the pump beam. Indeed, since the metal stripe is only 1 μm-wide, the combination of a slight lateral misalignment and intensity inhomogeneities along the pump-stripe width (see Fig. 5) can lead to large variations in the excited state molecular density overlapping with the LRSPP mode. Hence, a slightly different pump alignment can affect substantially the repeatability of the measurements. However, this issue can be resolved by improving the pump beam quality or, if the pump power is not a limitation, by increasing the width of the pump stripe.

The results shown on the central and bottom panels of Fig. 8 indicate that for experiments 3,4,5, and 6, the magnitude of $\Delta\gamma$ is significant and related to the increment in the measured insertion loss relative to the reference. This suggests that the discrepancy between γ_{ASE} and γ_{SEM} is caused by a fibre misalignment. Indeed, it is not surprising that a slight misalignment of the output fibre result in a significantly different measurement of P_o, as Figs. 6a and b show that the background ASE coupled into the output fibre can be ten times larger than the LRSPP counterpart. Thus, a slight misalignment in the output fibre suffices to capture enough background ASE light to bury the ASE-LRSPP signal, affecting the measured value of γ_{ASE}. On the other hand, the effect of fibre misalignments on γ_{SEM} is not expected to be as large due to the high coupling efficiency between the LRSPP and the fibre's fundamental mode, which explains the large $\Delta\gamma$ magnitude.

It is difficult to relate the magnitude of $\Delta\gamma$ to the magnitude of the change in insertion loss because an upward misalignment could lead to larger bulk ASE coupled into the fibre than for a lateral misalignment. Nonetheless, it is apparent that a fibre misalignment associated with an increase in insertion loss of ~ 0.5 dB could affect significantly the γ_{ASE} measurements. Thus, the technique based on ASE-LRSPP measurements must be used with care, always ensuring a good mechanical stability of the setup. We expect this problem to be less pronounced for structures with a thinner gain layer such that less bulk ASE is generated. This can be achieved by using microfabrication and etching techniques to develop PSs with thinner microfluidic channels or by incorporating solid-state gain media such as spin-coated dye- or quantum-dot-dopped polymers. For both cases, a gain thickness in the order of few microns is expected to be quite feasible.

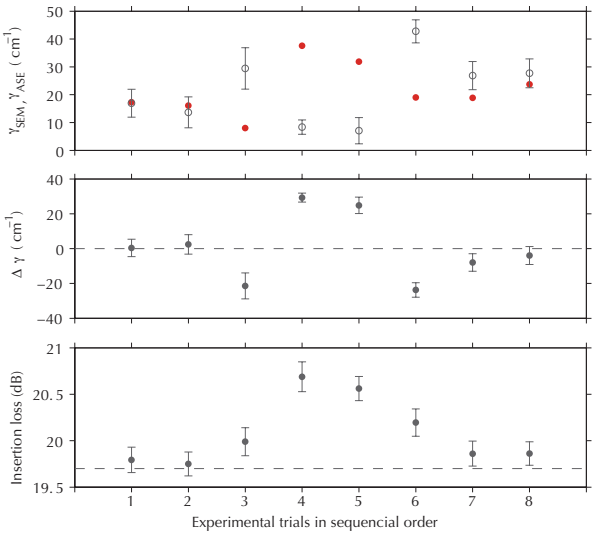

FIG. 8. Top panel: Mode power gain coefficient obtained via stimulated emission (γ_{SEM}, red solid circles) and via ASE-LRSPP (γ_{ASE}, grey open circles) for a number of experiments. The error bar for γ_{SEM} is about the size of the symbol. Centre panel: $\Delta\gamma = \gamma_{\mathrm{SEM}} - \gamma_{\mathrm{ASE}}$. Bottom panel: Insertion loss measured *in situ* for each experiment. For all cases, the amplitude of the error bars correspond to two times the mean squared error of the fit.

VI. SUMMARY AND CONCLUDING REMARKS

We have described an experimental setup and techniques to characterise the gain and noise of a LRSPP amplifier consisting of a symmetric metallic stripe waveguide incorporating optically pumped dye molecules in solution as the gain medium and with end-fire probe-signal coupling via optical fibres.

The experimental setup is designed to acquire optical measurements of absolute power over a narrow optical bandwidth at the amplifier's output, enabling the characterisation of the amplifier's gain and noise from a single experimental run. The amplifier's gain can be determined independently through measurements of stimulated emission using a monochromatic probe signal or from measurements of ASE-LRSPP over a narrow bandwidth using no probe signal, both measurements obtained during the same experimental run. We have described in detail the setup configuration, the calibration and alignment techniques, the mechanical and thermal stability of the setup-amplifier system, and the measurement procedures. We also discussed the methods to evaluate important gain and noise parameters from the experimental data such as, fibre-to-fibre gain, mode power gain coefficient, and effective input noise power. Finally we investigated the sensitivity of the gain measurements to pump and fibre misalignments. It is noted that small misalignments can impact considerably the gain measurements obtained through ASE-LRSPP measurements.

The setup and measurement procedures described here can be used to characterise other types of active photonic

or plasmonic structures having input and output ports that are accessible through end-fire coupling.

APPENDIX: ADDITIONAL MEASUREMENTS

Figs. 9 a, b, c, and d show, respectively, the detailed measurements of experimental trials 1, 2, 7, and 8, which gave good agreement between γ_{SEM} and γ_{ASE}. The bottom panels show measurements of ASE-LRSPP (crosses), of amplified LRSPP probe signal (open circles), and LRSPP probe stimulated emission (full circles); the NLS fits are shown as the dashed lines. The top panels show the amplifier gain in decibels, G_a, as a function of l_a as obtained from the LRSPP probe stimulated emission measurements and the fit to the linear amplifier region that estimates the coefficient γ_{SEM}.

[1] H. Raether, *Surface Plasmons on Smooth and Rough Surfaces and on Gratings.*, Springer, Berlin, 1988.
[2] K. Welford, Opt. Quant. Electron. **23**, 1 (1991).
[3] S. Maier and H. Atwater, J Appl Phys **98**, 011101 (2005).
[4] W. L. Barnes, A. Dereux, and T. Ebbesen, Nature **424**, 824 (2003).
[5] A. Degiron, P. Berini, and D. Smith, Opt. Photonics News, **19**, 28 (2008).
[6] J. N. Anker, W. P. Hall, O. Lyandres, N. C. Shah, J. Zhao, and R. P. V. Duyne, Nat Mater **7**, 442 (2008).
[7] P. Berini, Adv. Opt. Photon. **1**, 484 (2009).
[8] A. Boltasseva, T. Nikolajsen, K. Leosson, K. Kjaer, M. S. Larsen, and S. I. Bozhevolnyi, J. Lightwave Technol. **23**, 413 (2005).
[9] S. I. Bozhevolnyi, A. Boltasseva, T. Sondergaard, T. Nikolajsen, and K. Leosson, Optics Communications **250**, 328 (2005).
[10] R. Charbonneau, C. Scales, I. Breukelaar, S. Fafard, N. Lahoud, G. Mattiussi, and P. Berini, J Lightwave Technol **24**, 477 (2006).
[11] S. Jette-Charbonneau and P. Berini, Applied Physics Letters **91**, 181114 (2007).
[12] D. J. Bergman and M. I. Stockman, Phys. Rev. Lett. **90**, 027402 (2003).
[13] M. Nezhad, K. Tetz, and Y. Fainman, Optics Express **12**, 4072 (2004).
[14] I. Avrutsky, Physical Review B **70**, 155416 (2004).
[15] S. Maier, Optics Communications **258**, 295 (2006).
[16] M. Z. Alam, J. Meier, J. S. Aitchison, and M. Mojahedi, Optics Express **15**, 176 (2007).
[17] I. De Leon and P. Berini, Phys. Rev. B. **78**, 161401 (2008).
[18] I. De Leon and P. Berini, Optics Express **17**, 20191 (2009).
[19] J. Seidel, S. Grafstrom, and L. Eng, Phys. Rev. Lett. **94**, 177401 (2005).
[20] M. A. Noginov, G. Zhu, M. Mayy, B. A. Ritzo, N. Noginova, and V. A. Podolskiy, Phys. Rev. Lett. **101**, 226806 (2008).
[21] J. Grandidier, G. Colas des Francs, S. Massenot, A. Bouhelier, L. Markey, J.-C. Weeber, C. Finot, and A. Dereux, Nano Lett. **9**, 2935 (2009).
[22] R. F. Oulton, V. J. Sorger, T. Zentgraf, R.-M. Ma, C. Gladden, L. Dai, G. Bartal, and X. Zhang, Nature **461**, 629 (2009).
[23] M. T. Hill, Y.-S. Oei, B. Smalbrugge, Y. Zhu, T. D. Vries, P. J. V. Veldhoven, F. W. M. Van Otten, T. J. Eijkemans, J. P. Turkiewicz, H. D. Waardt, E. J. Geluk, S.-H. Kwon, Y.-H. Lee, R. Notzel, and M. K. Smit, Nature Photon. **1**, 589 (2007).
[24] M. A. Noginov, G. Zhu, A. M. Belgrave, R. Bakker, V. M. Shalaev, E. E. Narimanov, S. Stout, E. Herz, T. Suteewong, and U. Wiesner, Nature **460**, 1110 (2009).
[25] I. De Leon and P. Berini, Nature Photon. **4**, 382 (2010).
[26] M. C. Gather, K. Meerholz, N. Danz, and K. Leosson, Nature Photon. **4**, 457 (2010).
[27] P. M. Bolger, W. Dickson, A. V. Krasavin, L. Liebscher, S. G. Hickey, D. V. Skryabin, and A. V. Zayats, Opt. Lett. **35**, 1197 (2010).
[28] I. P. Radko, M. G. Nielsen, O. Albrektsen, and S. I. Bozhevolnyi, Opt. Express. **18**, 18633 (2010).
[29] J. Grandidier, G. Colas Des Francs, S. Massenot, A. Bouhelier, L. Markey, J. C. Weeber, and A. Dereux, J. Microscopy **239**, 167 (2010).
[30] K. Shaklee, R. Nahory, and R. Leheny, J Lumin **7**, 284 (1973).
[31] P. Berini, R. Charbonneau, N. Lahoud, and G. Mattiussi, J. Appl. Phys. **98**, 043109 (2005).
[32] I. De Leon and P. Berini, Phys. Rev. B. (to be published).
[33] B. E. A. Saleh and M. C. Teich, *Fundamentals of photonics, 1st. Edition.*, John Wiley & Sons, New York,, 1991.
[34] M. D. McGehee, R. Gupta, S. Veenstra, E. K. Miller, M. A. Diaz-Garcia, and A. J. Heeger, Physical Review B **58**, 7035 (1998).

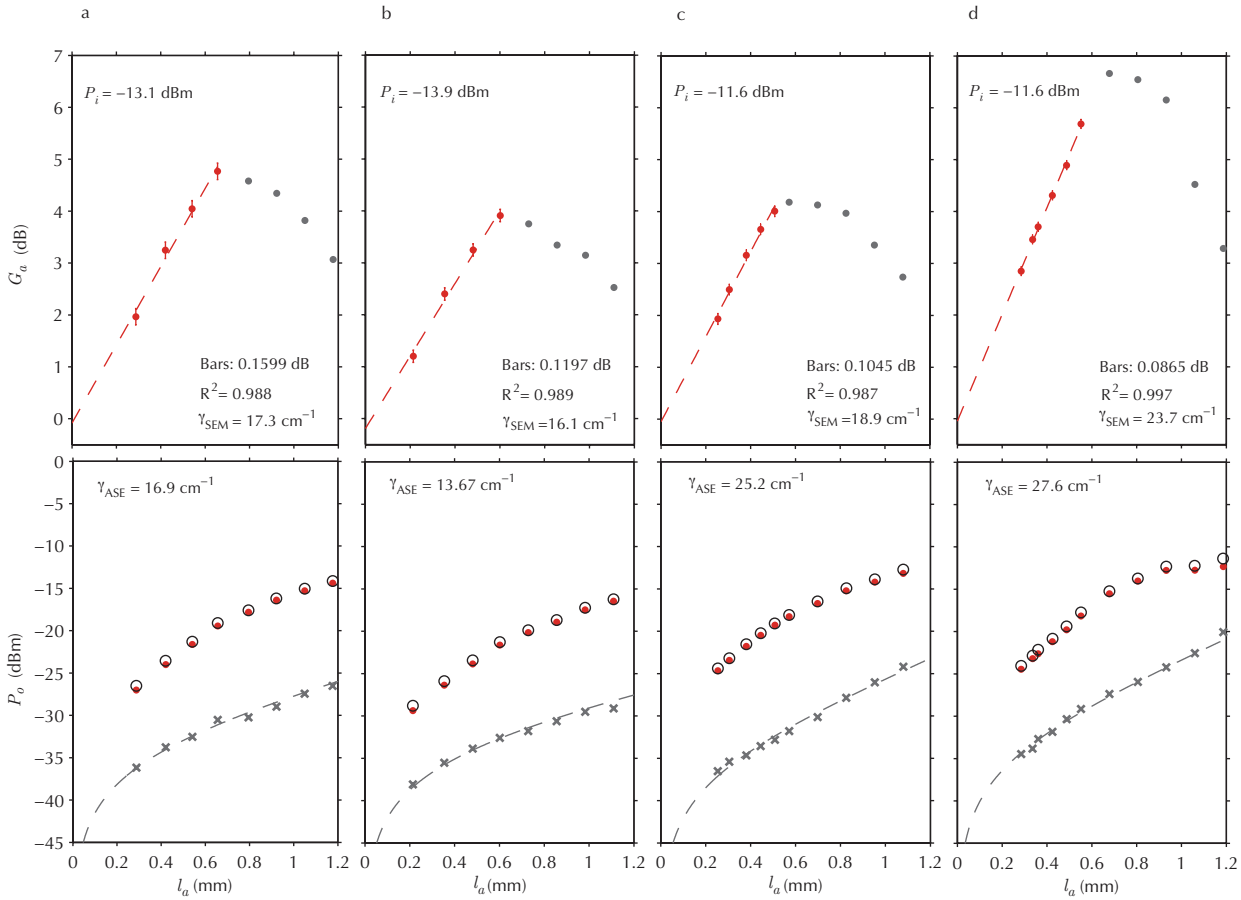

FIG. 9. Gain and noise measurements of a LRSPP amplifier. Top panels: Amplifier gain, G_a, as a function of its length, l_a, obtained from LRSPP probe stimulated emission measurements. The dashed lines are fits to the linear gain regions. Bottom panels: Power at the output fibre, P_o, for stimulated emission and ASE-LRSPP measurements; probe-on measurements (circles), probe-off measurements (crosses), probe-on minus probe-off (dots). The dashed curves are NLS fits to Eq. (5). The measurements shown in a, b, c, and d, correspond to measurements 1, 2, 7, and 8 in Fig. 8, respectively.

6.4 Setup variation for measurements in Chapter 4

The experimental setup described in this chapter was used to obtain the measurements in Chapter 5. On the other hand, the experimental setup employed for the measurements in Chapter 4 is slightly different. The section *Methods* in Chapter 4 includes a description of the experimental setup. The following list summarises the differences between the two setups.

- The setup used for experiments in Chapter 4 did not include the monochromator (MC) nor the cylindrical lens (L2).
- The setup used for experiments in Chapter 4 used a silicon photoreceiver (Newport, Mod. 818-BB-21A) instead of the APD module.
- In the setup used for experiments in Chapter 4, the AOM was located before the lens L1.
- The setup used for experiments in Chapter 4 did not include a syringe pump since the experiments were conducted with the dye under static conditions.

CHAPTER 7

Conclusions

Optical amplification offers a viable venue to reduce or even eliminate the propagation loss of SPPs without compromising their key attributes. This thesis explored the phenomena of amplification, spontaneous emission, and amplified spontaneous emission within the context of a SPP amplifier. The objective of this thesis was to contribute a deeper understanding of such phenomena through theoretical and experimental work on planar metallic structures incorporating a dipolar gain medium in the form of fluorescent organic molecules. The investigation presented here pays particular attention to the LRSPP mode supported by symmetric metallic slab- and stripe-waveguides. Nonetheless, in general, the theoretical and experimental conclusions are not restricted to LRSPPs.

7.1 Summary and contributions

For several years, researchers have studied the amplification of SPPs using theoretical models originally developed for the analysis of photonic amplifiers and lasers. Although the amplification mechanism for photons and SPPs is the same (i.e., stimulated emission), the conditions under which this process occurs are different in a SPP amplifier. The presence of the metal modifies the density of modes in its vicinity leading to a modification of the gain medium near the metal surface, where the SPP field is localised. Chapter 2 presented *an original theoretical model for SPP amplification in one-dimensional planar metallic structures incorporating an optically pumped dipolar gain medium*. The model accounted for the inhomogeneous gain distribution created close to the metal surface, and for the overlap between the gain and SPP-mode distributions. The inhomogeneous gain close to the metal surface is caused by an inhomogeneous pump irradiance distribution and by a position-dependent dipole lifetime; the former is the result of pump-light reflections throughout the multilayer structure, and the latter is caused by dipole relaxation into multiple energy decay channels present in the vicinity of the metal, such as dipole coupling to LRSPPs, SRSPPs, EH pairs in the metal, and radiative modes of the structure. The theory was applied to study the amplification of LRSPPs on a physically realisable structure consisting of a 20 nm-thick silver film bounded by Cytop (a lossless dielectric) on one side and by an index-matched gain medium on the other in the form of R6G dye molecules in solution. The theory predicted that complete compensation of the LR-

SPP propagation loss is possible at the wavelength $\lambda = 560$ nm using a moderate dye molecular density and a reasonable pump irradiance of 210 kW/cm^2 at $\lambda = 532$ nm. The proposed theory was compared against two simplified models: one that accounts for the pump position dependence but assumes a uniform dipole lifetime and one that assumes a uniform gain. The LRSPP mode power gain obtained with the proposed model was approximately an order of magnitude smaller than the values predicted by the simplified models. The discrepancy was ascribed to smaller gain-mode overlap present when the lifetime quenching near the metal surface is taken into account.

The theoretical model described in Chapter 2 was used in Chapter 3 to study the amplification of LRSPPs and single-interface SPPs on similar planar plasmonic structures using moderately (5 mM) and heavily (40 mM) concentrated R6G dye molecules in solution as the gain medium. The analysis considered the concentration-dependent photophysical properties of the dye. The model was employed to estimate the SPP mode power gain as a function of the pump irradiance. Numerical calculations showed that lossless propagation of single-interface SPPs supported by the structure could be achieved only with a high dye concentration using an intense pump irradiance of 3.45 MW/cm^2, whereas for LRSPPs it was achieved with both dye concentrations using pump levels of few hundreds of kW/cm^2 at $\lambda = 532$ nm. For the cases under analysis, neglecting the effects of pump and/or dipole lifetime position-dependence led to pump-irradiance requirements that are smaller by up to 800% when the mode power gain is close to saturation. On the other hand, it was shown that for dipoles with low quantum efficiency the lifetime distribution is well approximated as a constant; thus, the effects of the metal on the dipole's lifetime can be neglected in such a case.

Previous experimental studies have presented evidence of complete loss compensation in SPPs through optical amplification using indirect vehicles such as a theoretical interpretation of SPP stimulated emission or through the observation of laser-like behaviour of light coupled out of active plasmonic structures. Chapter 4 presented *a direct demonstration of gain in the LRSPP mode supported by a index-symmetric thin gold stripe waveguide at a near-infrared wavelength.* The gain medium consisted of a ~ 100 μm-thick index-matched layer of IR140 dye molecules in solution, which was pumped at normal incidence using linearly polarised pulsed light at $\lambda = 808$ nm. The LRSPP mode of the stripe was probed using CW light at $\lambda = 882$ nm via end-fire coupling using a polarisation maintaining fibre, and it was out-coupled of the waveguide in a similar fashion. A fibre-to-fibre gain of 1.10 was measured directly as the ratio of the stimulated-emission output power to the input power. This indicated not only complete compensation of the losses of the structure (that is, intrinsic mode propagation loss, coupling loss due to both facets and loss due to dye ground-state absorption in the unpumped sections), but also a power gain of 10%. The measured

small-signal LRSPP mode power gain was 8.55 dB/mm. In addition, Chapter 4 reported a 6.3 dB reduction of the spontaneous emission generated in the vicinity of the waveguide relative to that generated in the bulk gain. A qualitative explanation of this phenomenon was given in terms of the low probability of spontaneous emission into LRSPPs, and the large power dissipation involved in other energy decay processes with larger probabilities, such as dipole coupling to SRSPPs and EH pairs.

Spontaneous emission is a phenomenon of fundamental importance in optics, particularly in optical amplification and lasing since it is a form of noise that limits the performance of optical systems. It is well known that spontaneous emission of optical emitters located near metallic surfaces is significantly different to that of emitters located far from the metal. However, only few studies [51, 47] have addressed to some extent the implications of spontaneous emission near metallic surfaces within the context of SPP amplification. Chapter 5 presented and discussed *an experimental and theoretical analysis of spontaneous emission noise in a LRSPP amplifier* similar to that studied in Chapter 4. Usually, the large density of SPP modes at the metal surface enhances the spontaneous emission of optical emitters near the metal. This is not the case for the LRSPP (as explained in Chapter 4). The results in this chapter are believed to be *the first quantitative measurement of low spontaneous emission in a plasmonic structure with gain.* The experiment consisted in obtaining absolute power measurements of ASE-LRSPP at the output of the amplifier over a narrow optical bandwidth, from which the LRSPP mode power gain and effective noise input power were obtained. The latter is the power at the amplifier's input needed to produce an output signal with unitary signal to noise ratio, and it was measured at the peak ASE-LRSPP wavelength. The measured effective noise input power was only 3.3 times larger than the theoretical limit for linear optical amplifiers and it was comparable to noise values measured in other nearly optimum optical amplifiers. In addition, *an original semi-classical theoretical model to describe amplified spontaneous emission into the SPP modes of planar structures was presented.* The theory linked the amplifier noise to the spontaneous emission rate into the amplified mode. The theoretical model was applied to the experimental situation and its validity was confirmed via comparisons with the experimental results.

Chapter 6 described *the experimental techniques and setup employed for experimental measurements of gain and noise in the LRSPP amplifier.* The setup is capable of acquiring absolute power measurements at the amplifier's output over a narrow optical bandwidth. The experimental techniques allowed the measurement of fibre-to-fibre gain, ASE-LRSPP noise, LRSPP mode power gain coefficient. The latter was determined from two different methods using data generated in a single experimental run. In the first method, a (substantially) monochromatic probe signal was used to

excite the LRSPP in the amplifier and the mode power gain coefficient was obtained through measurements of probe stimulated emission. In the second method, measurements of ASE-LRSPP were used to determine the mode power gain coefficient by fitting experimental data to the theoretical expression of ASE. In addition, this chapter discussed in detail the setup configuration, the calibration and alignment techniques, the mechanical and thermal stability of the setup-amplifier system, and the measurement procedures. It also presented a series of experimental results, conducted under similar conditions, from which the repeatability of the experimental setup was assessed. The factors affecting the repeatability of the measurements were discussed.

7.2 Suggestions for future work

The theory proposed in Chapter 2 is restricted to one-dimensional planar structures. The experimental validation of this theory was not possible because such a one-dimensional device was not available. Experimental validation of the theory could be approached by adapting the theoretical model to handle two-dimensional structures similar to those studied in Chapter 4 and 5.

The study of SPP amplification in the non-linear regime is out of the scope of this thesis. Yet, from the experimental results given in Chapters 4-6, it is clear that a non-linear amplification region appears for large amplifier lengths. This phenomenon deserve further investigation both theoretical and experimental.

An important investigation would be taking the LRSPP amplifier one step further by incorporating a resonant cavity using wavelength selective gratings such that LRSPP lasing is achieved. Also, thermal wavelength tuning and noise characteristics of such a laser would be an important research path.

APPENDIX A

Setup instrumentation settings

This appendix provides information regarding the measurement instrumentation settings employed in the experiments. Please refer to the block diagram in Fig. 2 (and related text) in Chapter 6 for a detailed description of the experimental setup. Table A.1 shows the instrumentation used during the SPP amplification measurements. Each instrument is composed by a sensor (or actuator) device connected to a meter (or interface) device capable of communicating with a Windows-XP personal computer (PC). The sensor/actuator and meter/interface pairs are denoted by the identifier (ID) symbol defined in Fig. 2 of Chapter 6, and the respective instrument model numbers are provided along with the communication protocol and address (Comm:Addr) employed.

Table A.1 | Instruments and model numbers. [a] No model number was indicated by the manufacturer (Mechatronics). [b] The CS130 monochromator is equipped with a GPIB interface and is connected directly to the PC through the GPIB bus.

	Instrumentation		
ID	Sensor/Actuator	Meter/Interface	Comm:Addr
PS1 & PS2	Newport 918D-SL	Newport 2930C	GPIB:2
SW1 & SW2	Ledex LH1146-330 (Rot. Selonoid)	Twin-relay board[a]	Parallel:LPT1
APD	Hammamatsu C5658	Tektronix TDS 540A	GPIB:8
MC	Oriel Cornerstone 130 (CS130)	- [b]	GPIB:4

The instrument settings were selected to obtain reliable sets of measurements from typical SPP amplification experiments, such as those described in Chapter 6. For instance, the oscilloscope monitoring the APD readings is configured to acquire time-resolved readings of the 8 ns pulse amplifier's output reducing the pulse-to-pulse signal variations by averaging the signal over many pulses; the number of averaging pulses is defined by the switching times of SW1/SW2; the power meter that monitors the PS1/PS2 readings is configured to acquire sufficient readings of the CW passive power during the time-averaging intervals; finally, the settings of MC are optimised to reject undesired ASE noise while maintaining the power of the amplifier's output signal reaching the APD above its noise floor. The relevant settings for each instrument are given in Table A.2.

Table A.2 | Default instrument settings.

Newport 2930C	
Parameter	Settings
CH A	Connected to PS2
CH B	Connected to PS1
Mode	DC count
Filter	Analog
Filter Interval	1 ms
Ext. Trigger	OFF

Tektronix TDS540A	
Parameter	Settings
CH 1	Connected to trigger signal (from Nd:YAG pump laser)
CH 2	Connected to APD signal
CH 3	Connected to Silicon Photo-receiver (optional)
Coupling (CH1, CH2 & CH3)	DC (50 Ω)
Bandwidth (CH 2)	100 MHz
Bandwidth (CH 1 & CH3)	full (500 MHz)
Volt Scale (CH 2 & CH3)	500 mV/div
Time Scale (CH 2 & CH3)	10 ns/div
Ext. Trigger	ON
Trigger Type	Rise edge
Delayed Trigger	192 μs
Reading Mode	Average
Averaging	100

Oriel CS130	
Parameter	Settings
Optical Bandwidth	$\sim$ 1 nm
Central Wavelength	882 nm or 876 nm
Wavelength Scan Increment	0.08 nm
Grating Model	74027

Ledex LH1146-330	
Parameter	Settings
SW1 Behaviour	Normally Closed (Blanks when OFF)
SW2 Behaviour	Normally Closed
SW1 Open Time	7 sec.
SW2 Open Time	7 sec.

APPENDIX B

Setup automation software

This appendix outlines the operation and design of the automation software developed to perform the automatic measurement procedure described in Section III.E of Chapter 6. The software was developed using LabView 2009 running on a Windows-XP based PC. The PC counts with a GPIB PCI card (National Instruments PCI-GPIB) and a parallel port, both required by the automation software to control and monitor the instrumentation.

B.1 Graphical user interface

A snapshot of the automation software's graphical user interface (GUI) is shown in Fig. B.1. The GUI allows the user to start and stop the experiment sequence, monitor the measurements during the experiments, change some instrument settings, and select the setup calibration file. The red circled letters in Fig. B.1 label important controls and indicators, which are described next.

The calibration parameters (Cal. Params) box, labeled A, allows the user to select the calibration file that accounts for the losses in the optical paths involving PS1 and PS2 (see Fig. 2 of Chapter 6) at a specific wavelength. The calibration factors and wavelength obtained from this file are displayed in the 'Offset A', 'Offset B' and 'wavelength' controls. The 'Offset A' factor corresponds to $\Delta_{o\mathrm{A}}$, the optical loss of the oA branch, and the 'Offset B' factor corresponds to $\Delta_{i\mathrm{M}}$, the relation between the input and monitor power levels (see Sect.III.B in Chapter 6 for details on the setup calibration). The offsets and wavelength values can be modified manually through the GUI for calibration purposes. In such a case, clicking on the 'Update' button will update the software with the new values; similarly, clicking on the 'Save' button will save the new values in the calibration file. The 'Spike Tol.' control sets the acceptable tolerance (in dB) for PS1/PS2 spurious readings. The 'Tick Time' control indicates the time between readings; the default value is 100 ms.

The sequencer parameters (SEQ. Params) box, labeled B, allows the user to pause, restart, and stop the experiment sequence by clicking on the respective buttons. It also displays the elapsed time and the current status of the pump and probe signals (enable/disable). Finally, the drop-down controls allow the user to manually switch the pump and probe signal status by changing the control from 'Bypass' (software controlled) to 'Enabled' or 'Disabled'.

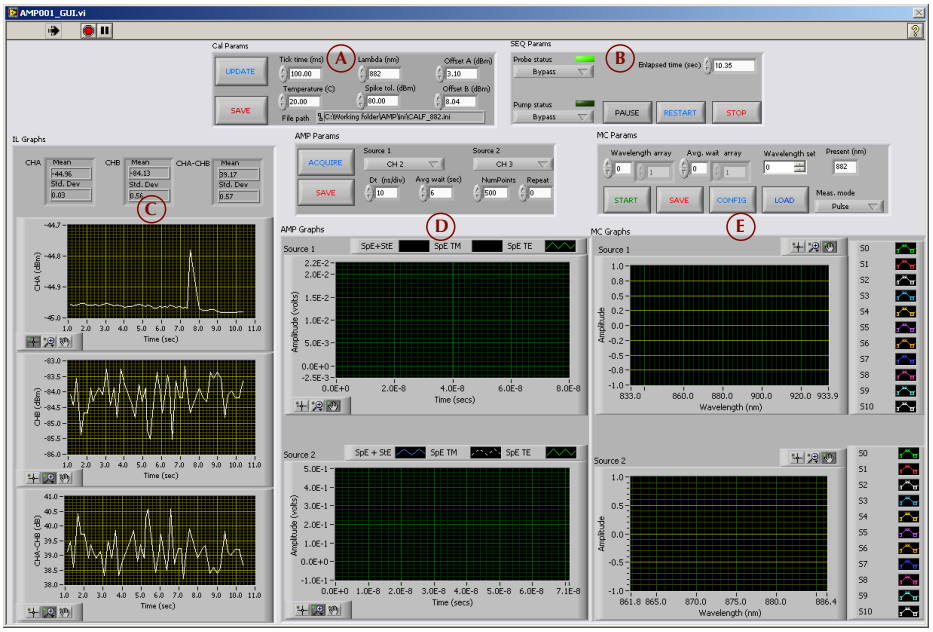

Figure B.1 | Automation software's GUI. The labels (red circled letters) are superimposed on the GUI image to indicate key controls and indicators.

The set of indicators in the Insertion-Loss Graph (IL Graph) box, labeled C, display information related to the CW power measurements performed by PS1 and PS2 during the experiment taking into account the calibration losses specified in the Cal. Params box. The graphs labeled 'CHA' and 'CHB' indicate the time evolution of the power at points o and i in Fig. 2 of Chapter 6, respectively. Similarly, the graph labeled 'CHA-CHB' plots the insertion loss of the device under as a function of time. The statical mean and standard deviation of these three curves are shown by the indicators located in the top section of the box.

The set of controls and indicators in the amplification parameters (AMP. Params) and amplification graph (AMP. Graph) boxes, labeled D, allow the user to perform and monitor time-resolved power measurements for the SPP amplification experiments using the APD. Through the AMP Params box the user can modify two settings of the TDS 540A oscilloscope– i.e., delayed trigger ('Dt') and number of points per plot ('NumPoints') – and the pulse-averaging duration ('Avg. Wait'). The software can monitor up to two sources (photo-detectors), which allows using the APD (assigned to channel 2 by default) and other fast photo-receiver (eg., 818-BB-21A; assigned to channel 3 by default) to monitor simultaneously the SPP amplifier's output and pump signals, respectively. By clicking on the 'Acquire' button, the software will perform as many measurements as indicated in the 'Repeat' control. The raw measured signals associated with 'Source 1' and 'Source 2' will be displayed (in Volts), respectively, on

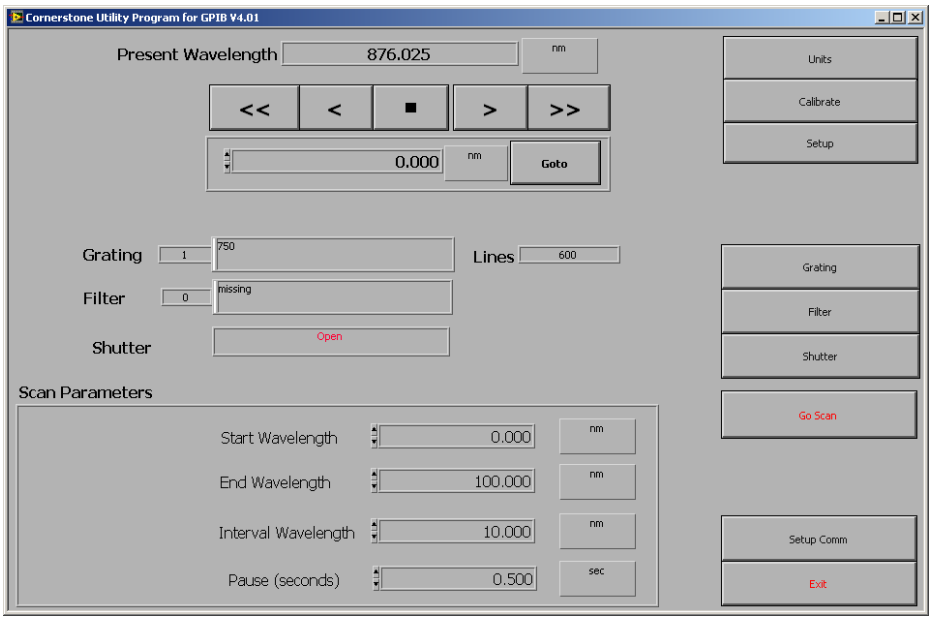

Figure B.2 | Monochromator control utility GUI.

the top and bottom graphs located in the AMP. Graph box. The measured signals can be saved in CSV (comma separated value) format by clicking on the 'Save' button in the AMP. Params box. *Note: In order to perform the experimental sequence described in Chapter 6, the pump and probe status in the SEQ. Params box must be set to 'Bypass'.*

The set of controls and indicators in the monochromator parameters (MC. Params) and monochromator graph (MC. Graph) boxes, labeled E, allow the user to perform wavelength sweep measurements of SPP amplification. The 'Wavelength set' control allows the selection of a number of user-defined *wavelength sweep configurations* stored in the 'mcscan.csv' configuration file (see Table B.1 in next section). By clicking on the 'Load' button the corresponding wavelength and pulse-averaging duration values are loaded into the 'Wavelength array' and 'Avg. Wait array', respectively. By clicking on the 'Start' button, a wavelength sweep is performed by automatically running the 'Acquire' command in the AMP Param. box for each of the values in the wavelength and pulse-averaging duration arrays. The wavelength at any point during the wavelength sweep measurements is indicated in the 'Present' indicator. The set of measurements corresponding to 'Source 1' and 'Source 2' are displayed as a function of the wavelength in the top and bottom graphs, respectively, in the MC. Graph box. These measurements can be saved in CSV (comma separated value) format by clicking on the 'Save' button. Finally, clicking on the 'Config' button will execute the Monochromator Control Utility, from which the monochromator can be controlled.

Please refer to the CS130 monochromator user manual for more information about this utility.

B.2 Automation software structure

The LabView virtual instruments (VIs) comprising the automation software are stored in a number of libraries that organise the files according to their VI hierarchy. The software stores data (eg., measurement results) in and retrieve data (eg., calibration parameters) from files located in specific directories. Table B.1 describes the different files and directories used by the automation software. The root directory (.) where the software resides is 'C:/working folder/AMP'.

Table B.1 | Files and directories used by the setup automation software.

Directory path	File name	Hierarchy	Description
.	AMP001.llb	1,2,3	Main GUI and sequencer related VIs
.	REL001.llb	4	Twin-relay card control driver
.	CS74000.llb	4	Oriel CS130 monochromator driver
.	NP2930C.llb	4	Newport 2930C power meter driver
.	TDS540A.llb	4	Tektronix TDS 540A oscilloscope driver
.	INST001.llb	5	Instrument VISA session handling VIs
./ini/	CS130.ini	-	Init. file for Oriel Cornerstone-130
./ini/	calf_882.ini	-	Init. file for setup path-loss factors at $\lambda = 882$ nm
./ini/	mcscan.csv	-	Init. file for wavelength sweep measurements
./meas/amp/	-	-	Holds saved amplification measurements
./meas/il/	-	-	Holds saved passive insertion loss measurements
./meas/mc/	-	-	Holds saved wavelength-sweep measurements

Fig. B.3 shows the first four hierarchy levels (including the zeroth level corresponding to the LabView application) of the software structure. All the VIs in the figure are contained in the library AMP001.llb. For the purposes of this section, the discussion is limited to VIs with hierarchy 1 to 3 highlighted in Fig. B.3. It suffices to mention that hierarchy-4 and hierarchy-5 VIs are called by hierarchy-3 VIs in order to send and retrieve information to/from the instrumentation.

The GUI VI (AMP001_GUI.vi) shown in Fig. B.1 is the only hierarchy-1 VI. As the automation code is executed, the GUI becomes operational and hierarchy-2 VIs, including AMP001_Setup.vi, AMP001_SEQ.vi, and AMP001_Cleanup.vi, are executed (see Fig. B.3a). Actions on the enabled GUI controls perform calls to hierarchy-3 VIs illustrated in Fig. B.3b and B.3c, with the exception of 'Restart' button in the SEQ. Params box, which re-execute the hierarchy-2 VIs.

Hierarchy-3 VIs are associated with the substructure of AMP001_Setup.vi and AMP001_SEQ.vi. AMP001_Cleanup.vi is self-contained and has no substructure;

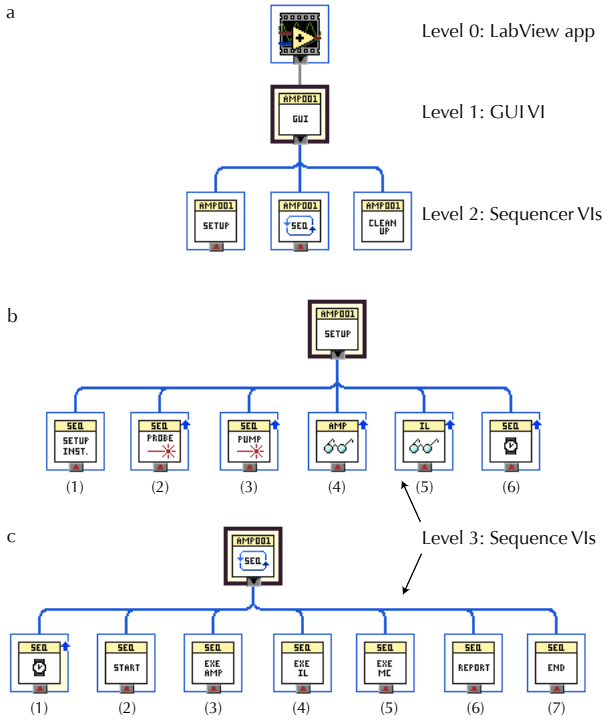

Figure B.3 | Automation code structure: (a) First three levels of the code's hierarchical structure;(b) substructure of the code's 'setup' algorithm; (c) substructure of the experiment sequence algorithm.

however, it is prepared to call hierarchy-3 VIs if future modifications so require. The hierarchy-3 VIs associated with AMP001_Setup.vi are shown in Fig. B.3b; they perform the following tasks according to their labels: (1) applying default settings to NP2930C, CS130, and TDS540A; (2) applying default settings to probe and (3) pump switches; (4) initialising AMP Graph and (5) IL Graph boxes; and (6) initialising elapsed time. Refer to Table A.2 for information regarding the default instrument settings. Similarly, the hierarchy-3 VIs associated with AMP001_SEQ.vi are shown in Fig. B.3c; they perform the following tasks according to their labels: (1) update elapsed time; (2) setup instruments (if needed) and read commands from GUI; (3) execute amplification measurements if so commanded; (4) execute passive insertion loss measurements; (5) execute wavelength-sweep measurements if so commanded; (6) prepare and save measurement reports; and (7) read GUI commands and finalise/abort sequence if needed.

Bibliography

[1] Ashcroft, N. W & Mermin, N. D. *Solid State Physics.* (Brooks Cole, 1976).

[2] Raether, H. *Surface Plasmons on Smooth and Rough Surfaces and on Gratings.* (Springer, 1988).

[3] Palik, E. D. *Handbook of Optical Constants of Solids.* (Academic Press, New York, 1985).

[4] Kovacs, G. J. Optical excitation of surface plasma waves in an indium film bounded by dielectric layers. *Thin Sold. Films.* **60,** 33-44 (1979).

[5] Fukui, M. *et al.* Lifetimes of Surface Plasmons in thin Silver Films. *Phys. Stat. Sol. B* **91,** K61-K64 (1979).

[6] Burke, J. J., Stegeman, G. I. & Tamir, T. Surface-polariton-like waves guided by thin, lossy metal films. *Phys. Rev. B* **33,** 5186-5201 (1986).

[7] Sarid, D. Long-Range Surface-Plasma Waves on Very Thin Metal Films. *Phys. Rev. Lett.* **47,** 1927-1930 (1981).

[8] Yang, F., Sambles, J. R., & Bradberry, G. W. Long-range surface modes supported by thin films. *Phys. Rev. B* **44,** 5855-5872 (1991).

[9] Berini, P. Long-range surface plasmon polaritons. *Adv. Opt. Photon.* **1,** 484-588 (2009).

[10] Barnes, W. L. Fluorescence near interfaces: the role of photonic mode density. **J. Mod. Optics. 45,** 661-699 (1998).

[11] Barnes., W. L. Surface plasmon-polariton length scales: a route to sub-wavelength optics. *J. Opt. A: Pure Appl. Opt.* **8,** S87.

[12] Barnes, W. L , Dereux, A., & Ebbesen, T. W. Surface plasmon subwavelength optics. *Nature* **424** 824-830 (2003).

[13] Simon, H. J., Mitchell, D. E., & Watson, J. G. Surface plasmons in silver films - a novel undergraduate experiment. *Am. J. Phys.* **43,** 630-636 (1975).

[14] Ford, G. W. & Weber, W. H. Optical electric-field enhancement at a metal surface arising from surface-plasmon excitation. *Opt. Lett.* **6,** 122-124 (1981).

[15] Stiles, P. L., Dieringer, D. J., Shah N. C. & Van Duyne R. P. Surface-Enhanced Raman Spectroscopy. *Annu. Rev. Anal. Chem.* **1,** 601-626 (2008)

[16] Neumann, T., Johansson, M. L., Kambhampati, D. & Knoll, W. Surface-plasmon fluorescence spectroscopy. *Adv. Funct. Mater.* **12,** 575-586 (2002).

[17] Simon, H. J., Mitchell, D. E., & Watson, J. G. Optical Second-Harmonic Generation with Surface Plasmons in Silver Films. *Phys. Rev. Lett.* **33,** 1531-1534 (1974).

[18] E. Ozbay, Plasmonics: Merging photonics and electronics at nanoscale dimensions. *Sience* **311,** 189-193 (2006).

[19] Barnes, W. L., Dereux, A. & Ebbesen, T. W. Surface plasmon subwavelength optics. *Nature* **424,** 824-830 (2003).

[20] Kawata, S., Inouye, Y. & Verma, P. Plasmonics for near-field nano-imaging and superlensing. *Nature Photon.* **3,** 388-394 (2009).

[21] Berini, P. Bulk and surface sensitivities of surface plasmon waveguides. *New J. Phys.* **10,** 105010 (2008).

[22] Anker, J. N. *et al.* Biosensing with plasmonic nanosensors. *Nature Mater.* **6,** 442 (2008).

[23] Nezhad, M. P., Tetz, K. & Fainman, Y. Gain assisted propagation of surface plasmon polaritons on planar metallic waveguides. *Opt. Express.* **12,** 4072-4079 (2004).

[24] Siegman, A. E. *Lasers.* (University Science Books, 1986).

[25] Plotz, G., Simnon, H., & Tucciarone, J. Enhanced total reflection with surface plasmons. *J. Opt. Soc. Am.* **69,** 419-422 (1979)

[26] Sudarkin, A. N. & Demkovich, P. A. Excitation of surface electromagnetic waves on the boundary of a metal with an amplifying medium. *Sov. Phys. Tech. Phys.* **34,** 764-766 (1988).

[27] Seidel, J., Grafstrom, S. & Eng, L. Stimulated emission of surface plasmons at the interface between a silver film and an optically pumped dye solution. *Phys. Rev. Lett.* **94,** 177401 (2005).

[28] Bergman, D. J. & Stockman, M. I. Surface plasmon amplification by stimulated emission of radiation: quantum generation of coherent surface plasmons in nanosystems. *Phys. Rev. Lett.* **90,** 027402 (2003).

[29] Ramakrishna, S. A. & Pendry, J. B. Removal of absorption and increase in resolution in a near-field lens via optical gain. *Phys. Rev. B* **67,** 201101 (2003).

[30] Pendry, J. B. Negative refraction makes a perfect lens. *Phys. Rev. Lett.* **85,** 3966-3969 (2000).

[31] Avrutsky, I. Surface plasmons at nanoscale relief gratings between a metal and a dielectric medium with optical gain. *Phys. Rev. B* **70,** 155416 (2004).

[32] Okamoto, T., H'Dhili, F. & Kawata, S. Towards plasmonic band gap laser. *App. Phys. Lett.* **85,** 3968 (2004).

[33] Okamoto, T., Simonen, J. & Kawata, S. Plasmonic band gaps of structured metallic thin films evaluated for a surface plasmon laser using the coupled-wave approach. *Phys. Rev. B* **77,** 115425 (2008)

[34] Okamoto, T., Simonen, J. & Kawata, S. Plasmonic crystal for efficient energy transfer from fluorescent molecules to long-range surface plasmons. *Opt. Express* **17,** 8294-8301 (2009)

[35] Winter, G., Wedge, S. & Barnes, W. L. Can lasing at visible wavelength be achieved using the low-loss long-range surface plasmon-polariton mode? *New J. Phys.* **8,** 125 (2006).

[36] Maier, S. A. Gain-assisted propagation of electromagnetic energy in subwavelength surface plasmon polariton gap waveguides. *Opt. Commun.* **258,** 295-299 (2006).

[37] Alam, M. Z., Meier, J., Aitchison, J. S. & Mojahedi, M. Gain assisted surface plasmon polariton in quantum well structures. *Opt. Express* **15,** 176-182 (2007).

[38] Sirtori, C., Gmachl, C., Capasso, F., Faist, J., Sivco, D. L., Hutchinson, A. L. & Cho, A. Y. Long-wavelength ($\lambda \approx 11.5\mu$m) semiconductor lasers with waveguides based on surface plasmons. *Opt. Phys. Lett.* **23,** 1366-1368 (1998).

[39] Tredicucci, A., Gmachl, C., Capasso, F., Hutchinson, A. L., Sivco, D. L. & Cho, A. Y. Single-mode surface-plasmon laser. *App. Phys. Lett.* **76,** 2164-2166 (2000).

[40] Noginov, M. A, Podolskiy, V. A, Zhu, G., Mayy, M., Bahoura, M., Adegoke, J. A., Ritzo, B. A. & Reynolds, K.3 Compensation of loss in propagating surface plasmons polariton by gain in adjacent dielectric medium. *Opt. Express* **16,** 1385-1392 (2008).

[41] Noginov, M. A., Zhu, G. Mayy, M., Ritzo, B. A., Noginova, N. & Podolskiy, V. A. Stimulated Emission of Surface Plasmon Polaritons. *Phys. Rev. Lett.* **101,** 226806 (2008).

[42] Hill, M. T., Oei, Y.-S., Smalbrugge, B., Zhu, Y., De Vries, T., Van Veldhoven, P. J., Van Otten, F. W. M., Eijkemans, T. J., Turkiewicz, J. P., De Waardt, H., Geluk, E. J., Kwon, S.-H., Lee, Y.-H., Notzel, R. & Smit, M. K. Lasing in metallic-coated nanocavities. *Nature Photon.* **1,** 589-594 (2007).

[43] Hill, M. T., Marell, M., Leong, E. S. P., Smalbrugge, B., Zhu, Y., Sun, M., Van Veldhoven, P. J., Geluk, E. J., Karouta, F., Oei, Y.-S., Notzel, R., Ning, C.-Z. & Smit, M.K. Lasing in metal-insulator-metal sub-wavelength plasmonic waveguides. *Opt. Express* **17,** 11107-11112 (2009).

[44] Ambati, M., Nam, S. H., Ulin-Avila, E., Genov, D. A., Bartal, G. & Zhang, X. Observation of Stimulated Emission of Surface Plasmon Polaritons. *Nano Lett.* **8,** 3998-4001 (2008).

[45] Grandidier, J., Colas des Francs, G., Massenot, S., Bouhelier, A., Markey, L., Weeber, J.-C., Finot, C. & Dereux, A. Gain-Assisted Propagation in a Plasmonic Waveguide at Telecom Wavelength. *Nano Lett.* **9,** 2935-2939 (2009).

[46] Grandidier, J., Massenot, S., Colas des Francs, G., Bouhelier, A., Weeber, J. C., Markey, L., Dereux, A., Renger, J., Gonzalez, M. U. & Quidant, R. Dielectric-loaded surface plasmon polariton waveguides: Figures of merit and mode characterization by image and Fourier plane leakage microscopy, *Phys. Rev. B* **78,** 245419 (2008).

[47] Oulton, R. F., Sorger, V. J., Zentgraf, T., Ma, R.-M., Gladden, C., Dai, L., Bartal, G. & Zhang, X. Plasmon lasers at deep subwavelength scale. *Nature* **461,** 629-632 (2009).

[48] Oulton, R. F., Sorger, V. J., Genov, D. A., Pile, D. F. & Zhang, X. A hybrid plasmonic waveguide for subwavelength confinement and long-range propagation. *Nature Photon.* **2,** 496-500 (2008).

[49] Bjork, G. & Yamamoto, Y. Analysis of semiconductor microcavity lasers using rate equations. *IEEE J. Quantum Elect.* **27,** 2386-2396 (1991).

[50] Noginov, M. A., Zhu, G., Belgrave, A. M., Bakker, R., Shalaev, V. M., Narimanov, E. E., Stout, S., Herz, E., Suteewong, T. & Wiesner, U. Demonstration of a spaser-based nanolaser. *Nature* **460,** 1110-1113 (2009).

[51] Bolger, P. M., Dickson, W., Krasavin, A. V., Liebscher, L., Hickey, S. G., Skryabin, D. V. & Zayats, A. V. Amplified spontaneous emission of surface plasmon polaritons and limitations on the increase of their propagation length. *Opt. Lett.* **35,** 1197-1199 (2010).

[52] Berini, P. Plasmon-polariton waves guided by thin lossy metal films of finite width: Bound modes of symmetric structures. *Phys. Rev. B* **61,** 10484-10503 (2000).

[53] Berini, P., Charbonneau, R., Lahoud, N. & Mattiussi, G. Characterization of long-range surface-plasmon-polariton waveguides. *J. Appl. Phys.* **98,** 043109 (2005).

[54] Chance, R. R., Prock, A. & Silbey, R. Molecular Fluorescence and Energy Transfer Near Interfaces. *Adv. Chem. Phys.* **37,** 1-65 (1978).

[55] Ford, G. W. & Weber, W. H. Electromagnetic interactions of molecules with metal surfaces. *Phys. Rep.* **113,** 195-287 (1984).

[56] Yeh, P. *Optical waves in layered media* (Wiley, New York, 1988).

[57] Chen, C., Berini, P., Feng, D., Tanev, S., & Tzolov, V. Efficient and accurate numerical analysis of multilayer planar optical waveguides in lossy anisotropic media. *Opt. Express* **7,** 260-272 (2000).